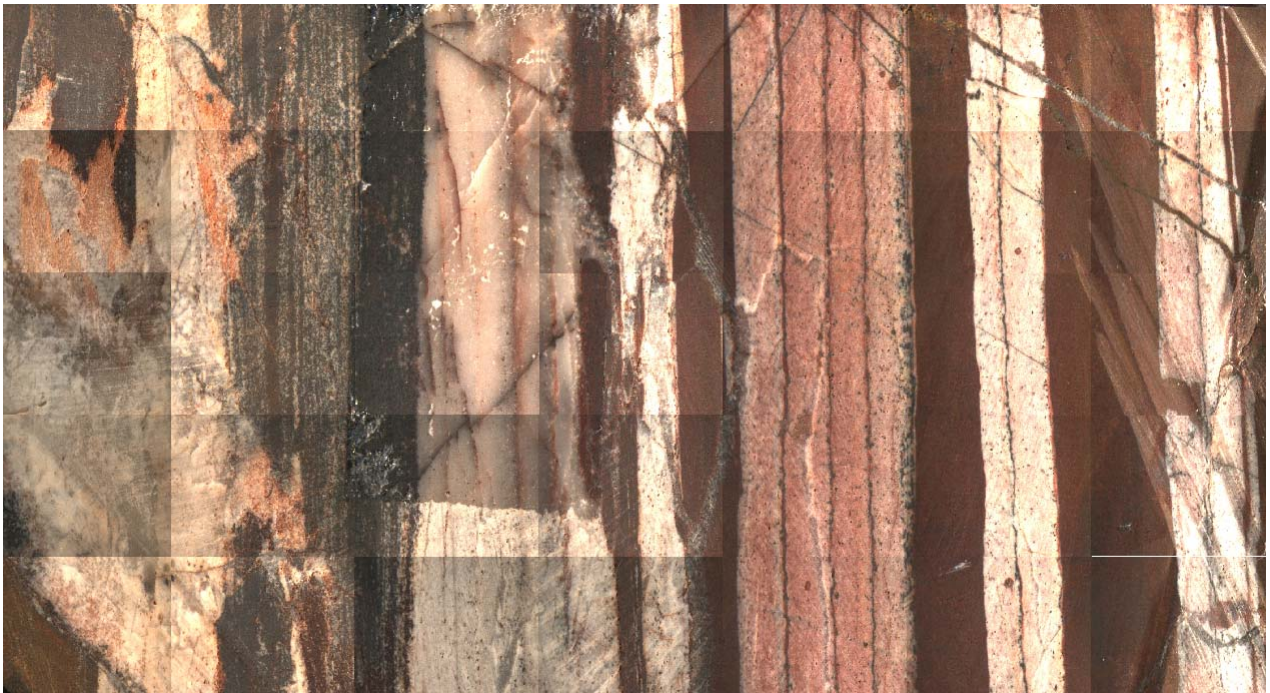


X-ray fluorescence microanalysis

*Instrumental capabilities and application to
Archaean cherts*



MSc Thesis

Utrecht University, The Netherlands, August 2010

Sophie Jansen

Under supervision of Dhr. Dr. M.J. Van Bergen

Table of Contents

Executive Summary	Page 4
General Introduction	Page 6
Chapter outlines	Page 7
Chapter 1: Background and Principles of XRF Spectroscopy	Page 10
1.1 Introduction	Page 10
1.2 Principles of XRF	Page 11
1.3 Source	Page 14
1.4 Detector	Page 16
1.5 Micro-XRF	Page 17
Chapter 2: Experimental determination of optimal measurement conditions for geological samples	Page 22
2.1 Introduction	Page 22
2.2 Methods	Page 24
2.3 Optimal Amplifier test	Page 25
2.3.1 Results	Page 25
2.3.2 Discussion and Conclusions	Page 25
2.4 30- μ m Polycapillary Voltage Tests	Page 26
2.4.1 Results	Page 26
2.4. 2 Discussion and Conclusions	Page 26
2.5 Aperture Voltage Tests	Page 27
2.5.1 Results	Page 27
2.5.2 Discussion and Conclusions	Page 27
2.6 30- μ m Polycapillary Current Tests	Page 27
2.6.1 Results	Page 27
2.6.2 Discussion and Conclusions	Page 29
2.7 Aperture Current Tests	Page 29
2.7.1 Results	Page 29
2.7.2 Discussion and Conclusions	Page 29
Sheet 2.1	Page 30
Sheet 2.2	Page 31
Sheet 2.3	Page 32
Sheet 2.4	Page 33
Sheet 2.5	Page 34
Sheet 2.6	Page 35
Chapter 3: Evaluation Test for Quantitative Analyses	Page 37
3.1 Introduction	Page 37
3.2 Methods	Page 37
3.3 Results and Discussion	Page 40
3.3.1 Precision	Page 40

3.3.2 Accuracy	Page 41
3.4 Conclusions	Page 43
Chapter 4: Archaean Chert and Banded Iron Formation Samples from Pilbara, Australia	Page 46
4.1 Introduction	Page 46
4.2 Methods	Page 47
4.2.1 Sample 1(C-chert): Red, Pink, White and Black layers	Page 47
4.2.1.1 Qualitative	Page 47
4.2.1.2 Quantitative	Page 47
4.2.2 Sample (S-chert): White and various Grey layers	Page 48
4.2.2.1 Qualitative	Page 48
4.3 Results	Page 50
4.3.1 Sample 1(C-chert): Red, Pink, White and Black layers	Page 50
4.3.1.1 Laminations	Page 50
4.3.1.2 Veins	Page 52
4.3.2 Sample (S-chert): White and various Grey layers	Page 52
4.4 Discussion	Page 63
4.4.1 Sample 1	Page 63
4.4.1.1 Quality of element analysis	Page 63
4.4.1.2 Red and Black layers	Page 64
4.4.1.3 Pink and Orange layers	Page 64
4.4.1.4 White layers	Page 65
4.4.1.5 Minerals	Page 65
4.4.1.6 Veins	Page 66
4.4.2 Sample 2	Page 66
4.4.2.1 Quality of element analysis	Page 66
4.4.2.2 Laminations	Page 66
4.4.3 Background on Achaean environments of chert deposition	Page 67
Box 4.1	Page 69
4.4.4 Implications from the analytical results	Page 70
4.5 Conclusions	Page 71
General Conclusions and Recommendations	Page 75
Acknowledgements	Page 78
Literature	Page 78
Appendix 1 Standard deviations of the measured or practical data	Page 82
Appendix 2 Theoretical and Practical Wt% of the standards	Page 88
Appendix 3 The complete Quantitative data of Sample 1	Page 97
Appendix 4: The Micro XRF Work routine User's Manual	Page 100

Executive Summary

This thesis describes the results of an analytical study into μ -XRF spectroscopy and capabilities of the technique, aimed at applications in geological research. Background, principles and a brief history of XRF spectrometry are explained, a theoretical account is given of the interaction between X-rays and target material, and the components needed for XRF application on micro-scale are described.

Tests were performed to explore parameter settings of the instrument that would yield optimum results for various analytical purposes. The results indicate that (1) an amplifier time of 6.4 μ s produces optimum peak resolution for qualitative analysis, (2) voltages of 20-30 keV and currents up to 600 μ A are most suitable for qualitative analysis, (3) reproducible data can be obtained for quantitative analysis, (4) software provided by the manufacturer and a standardless approach are inadequate for obtaining quantitative results with an accuracy that many geological research questions demand. Tests on international geological reference materials with known compositions showed deviations from accepted values between 0.5 and 22% for major and minor elements.

Using the optimized parameter settings, μ -XRF analyses were performed on two different types of color-banded Archaean chert. One was supposedly deposited as a chemical precipitate in a marine-hydrothermal environment. Individual, up to several cm thick layers showed clear compositional contrasts. Red and black layers were iron-rich, while white, pink or orange layers contained abundant silicon. Quantitative analyses, carried out with a 2-mm spot size, yielded ca. 60 wt% SiO_2 and 30 wt% Fe_2O_3 for the dark group of layers, and ca. 88 wt% SiO_2 and virtually no iron for the pale group. The measurements showed MnO concentrations up to \sim 0.15 wt% in the red layers and the existence of a clear stratigraphic trend in Fe/Mn ratios of individual layers. Findings support the hypothesis that hydrothermal activity played a major role in the supply of Si, Fe and Mn. Hence, it is inferred that color-banding reflects changes in the vigor of hydrothermal activity.

A second analyzed sample is a color-banded "silicified precursor chert", which represents a volcanoclastic sediment that became silicified by interaction with silica-saturated seawater. Qualitative μ -XRF results pointed to the presence of quartz, Fe-bearing sericite and some rutile. In this case, color differences were attributable to subtle mineralogical variations, possibly reflecting original changes in sediment supply.

This thesis includes a recommended work routine as manual for μ -XRF analysis, meant to serve future users.

General Introduction

This thesis describes the results of a study into advantages and limitations of micro X-ray fluorescence spectrometry, as applicable to a recently acquired instrument at the Department of Earth Sciences. This relatively new analytical technique is capable of providing qualitative and quantitative data on geological materials at small scales, relatively fast and without damaging the samples.

Various instrumental techniques are presently available for determining major, minor and trace-element concentrations in bulk rocks and other solid geological samples. Among the most widely used are XRF (X-Ray Fluorescence), ICP-OES (Inductively Coupled Plasma Optical Emission Spectrometry) and ICP-MS (Inductively Coupled Plasma Mass Spectrometry). In-situ techniques such as EPMA (Electron Microprobe Analysis) and LA-ICP-MS (Laser-Ablation ICP-MS) measure samples at very small scales, usually between one and several tens of microns. As many rocks and sediments are inhomogeneous at mm to cm scales, an analytical method is needed that can determine compositions at intermediate spatial scales with the same level of confidence as the traditional techniques. The μ -XRF is a good candidate to meet this requirement, since it is capable of analyzing surface areas of a few millimetres and down to 10 μ m (HORIBA, Ltd., 2010). Also, it is a relatively fast and non-destructive method. In particular compared to the techniques for bulk analysis, it is less time consuming as little sample preparation is required, and as it avoids the need of dissolving a sample (e.g. after micro-drilling) so that large numbers of samples can be handled.

The instrument used for this research is a bench-top Energy Dispersive X-Ray Fluorescence instrument with micro spot (a μ -XRF), recently purchased from EDAX (AMETEK Inc.). The μ -XRF is fitted with a Rh tube (the X-ray source) and a Silicon Drift Detector (SDD) with a Be window. This filters the signals produced by lighter elements, so that only elements with characteristic lines above 1 keV appear in the spectra. In practice this means that the instrument measures elements from Sodium (Na) ($Z = 11$) to Berkelium (L) ($Z=97$). Three available spot-controlling devices are a 30 μ m poly-capillary and 1 or 2 mm apertures. Measurements can be done under low vacuum or in air. Various options available for quantitative analysis, for example FP No Standards and measurements against preset (manually created) databases. In this research only the FP No Standards option has been examined.

μ -XRF spectrometry promises to be particularly interesting for analyzing Archaean ($\sim 3,5$ Ga) cherts and Banded Iron Formations (BIFs), which are often laminated and compositionally variable down to cm or mm-scale. Investigating Archaean cherts and BIFs is of practical interest, given that these rocks might host the earliest and oldest

(biological) fossils known (Schopf et al., 2002). Thus these ancient rocks may hold the key to the origin of life. These rocks are believed to record ancient conditions because they are fairly resistant to weathering (Kato & Nakamura, 2003). They document changes in atmospheric oxygen levels (Cloud, 1972; Chown et al., 2000), and provide information about their depositional environment (shallow versus deep marine; Chown et al., 2000), the origin of silica, and the presence of Archaean plate-tectonics (Kato & Nakamura, 2003). Finally, these rocks put constraints on minerals that may have been involved when life on earth started to develop (Papineau, 2010).

Samples tested in this research are Australian Archaean cherts that were previously analyzed by ICP-MS (Sander van den Boorn, 2008). These samples differ from each other in appearance and are supposed to have different origins. One specimen, a red, white and black laminated chert is thought to have been chemically precipitated from a silica-saturated solution, either seawater or hydrothermal water (C-chert). The other sample, a chert with layers of various grey tones, was classified as a 'sedimentary precursor chert' (S-chert), which formed when a parent rock or sediment was silicified. Their chemical compositions and internal (laminar) variations provide information about the sources of silica and other elements, and reflect signatures of precursor material. Besides the determination of chemical compositions, the data quality and detection limits have been examined. The extent of compositional variabilities, expected from the visible colour layering, was tested.

A principal aim of this study was to examine whether collected μ -XRF data are of sufficiently high quality to be used for geological purposes. Concerning the Archaean samples, special attention was paid to the significance of lamina-scale variations in hydrothermal or seawater origins. Furthermore, an attempt was made to interpret the findings in terms of depositional environment of the cherts.

To ensure that the obtained knowledge on μ -XRF operating procedures will become available for other researchers, a User's Manual was created. It explains various functions available for sample analysis and data display.

Chapter outlines

Chapter 1 explains the general principles of X-ray fluorescence – i.e. the physical foundation of this technique at atomic level – and introduces the components present in an X-ray fluorescence spectrometer for micro-analysis. This chapter also describes the developments that promoted the appearance of the μ -XRF technique for analysis with mm and μ m spot sizes.

Chapter 2 tackles the initial problem of determining an optimum parameter set for qualitative analysis. Various tests are described for choosing the optimal spot size, amplifier time, voltage and current.

Sheet 2.1 contains voltage experiment data executed with the 30- μm beam.

In *Sheet 2.2* the results of voltage experiments with the 1-mm beam can be found.

Sheet 2.3 presents the 2-mm beam voltage experiment results.

Sheet 2.4 displays results for the 30- μm beam current experiment.

Sheet 2.5 contains current experiment results executed with the 1-mm beam

In *Sheet 2.6* the 2-mm beam current experiment data are shown.

Chapter 3 describes various tests executed for determining the precision and accuracy of data obtained by the $\mu\text{-XRF}$. This was done on three geological standards, using the 2 mm spot, various voltages and currents, and two amplifier time conditions.

In *Chapter 4* the qualitative and quantitative data of the Archaean samples are described and discussed. Discussed topics include the compositional differences between the samples and between lamina, the environments in which the Archaean samples may have formed, possible reasons for a discovered stratigraphic change in Fe/Mn- ratio, and criteria for acceptable qualitative and quantitative data.

Appendix 1 contains standard deviations for the measured data per chosen condition set, per geological standard. Graphs of these standard deviations are also included.

Appendix 2 displays the measured weight percentages (and their accuracy) of the three geological standards, again sorted per used parameter set.

In *Appendix 3* the measured quantitative data of the ten most important elements for the first specimen is given. The data was collected for different ten layers.

Appendix 4 contains the 'Micro XRF Work routine User's Manual' in which the basics of operating the micro-XRF are explained.

Chapter 1: Background and Principles of XRF Spectrometry

1.1 Introduction

X-rays were first discovered in the late 19th century by Wilhelm Conrad Röntgen when he was experimenting with cathode rays and a Hittorf–Crooks tube, which is an ion tube covered with a piece of opaque black cardboard and with electrons hitting its walls (Röntgen, 1896; Arai, 2006; Langhoff and Simionovici, 2006). He discovered that a piece of paper, with barium platino-cyanide applied on one side, lit up with fluorescence when held in the proximity of this tube. Because it was clear to Röntgen that the radiation - which he named x-radiation for briefness - could penetrate the cardboard, it led him to ask the question of how far this radiation could penetrate other bodies and materials. As a result he made the first x-ray image of a human hand (*Figure 1.1*). This picture was one of the first indicators of the changes to come in the medical world now it was possible to 'see' inside human bodies.

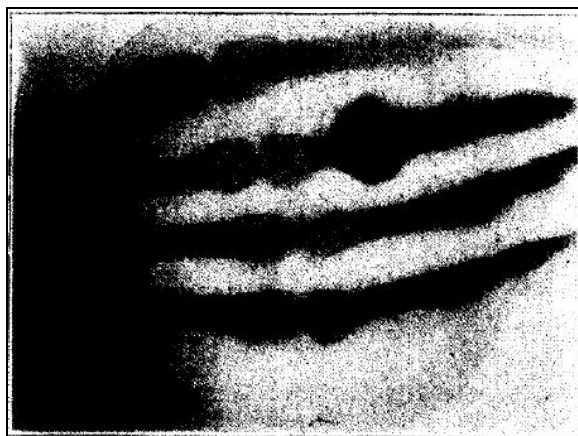


Figure 1.1 The first (published) x-ray image of a human hand (Source: Röntgen, 1896)

X-rays, however, are not just of interest to the medical world, but nowadays they are widely used in countless other fields like geology, archeology and industries. In geology x-rays are used for determining the composition of rocks and other samples by means of X-Ray Fluorescence (XRF), a technique that is based on the ionization of atoms in samples that are hit by a beam of primary x-rays (Janssens, 2005). The excited atoms in the sample create x-rays that are characteristic for each specific type of atom. When these characteristic x-rays are emitted, they provide information about the type of atoms and the amounts at which they are present in the sample material.

There are two types of XRF depending on how the X-rays are characterized: Wavelength Dispersive XRF (WDXRF) and Energy Dispersive XRF (EDXRF). WDXRF spectrometry uses a single crystal to produce a narrow wavelength band for sequel analysis of individual elements. With EDXRF spectrometry, an energy selective detector is used to separate narrow energy bands from the radiation emitted by the sample (Janssens, 2005), so that multiple elements can be analyzed simultaneously. Both techniques are used for analysis

of bulk samples. Extensive developments since the first EDXRF instrument became commercially available in the beginning of the 1970s have made it increasingly possible to analyze small parts of samples for more detailed investigations with this technique.

Besides the fact that XRF analyses provide element identification and concentrations, XRF has been popular because it does not require much sample preparation. Because of the non-destructive character of this technique, XRF analysis is also very suitable for investigating valuable objects such as archeological materials.

1.2 Principles of XRF

The principle of EDXRF is that incident x-rays produced by a source are concentrated and guided to the sample. Some of these x-rays will pass through the sample, but some will be reflected off its surface. When incident photons enter the sample and collide with the electrons present in the atoms, physical reactions occur that cause these atoms to emit x-rays that are characteristic for them. These secondary x-rays, or characteristic x-rays, hit a detector and will be transformed into element identification lines and concentration levels (*Figure 1.2a*). With WDXRF, the incident x-rays or particles hit the sample and characteristic x-rays are produced as with EDXRF. These characteristic x-rays then fall on a crystal that scatters and diffracts them according to their wavelengths. By changing the incidence angle and specimen-crystal-detector geometry, the diffracted rays are usually sequentially detected and translated into a spectrum (*Figure 1.2b*).

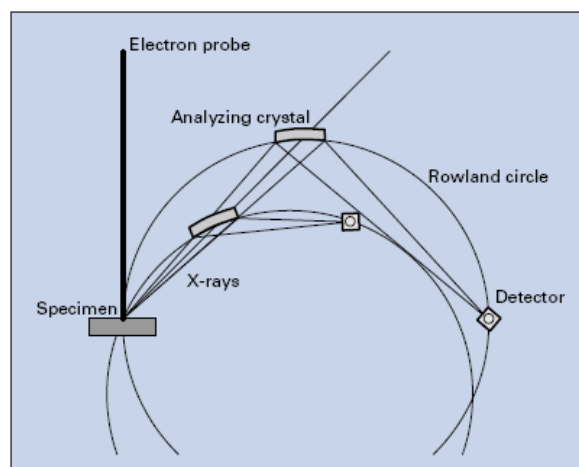
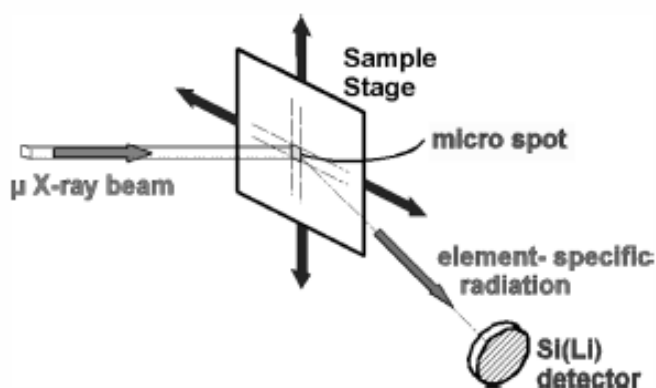


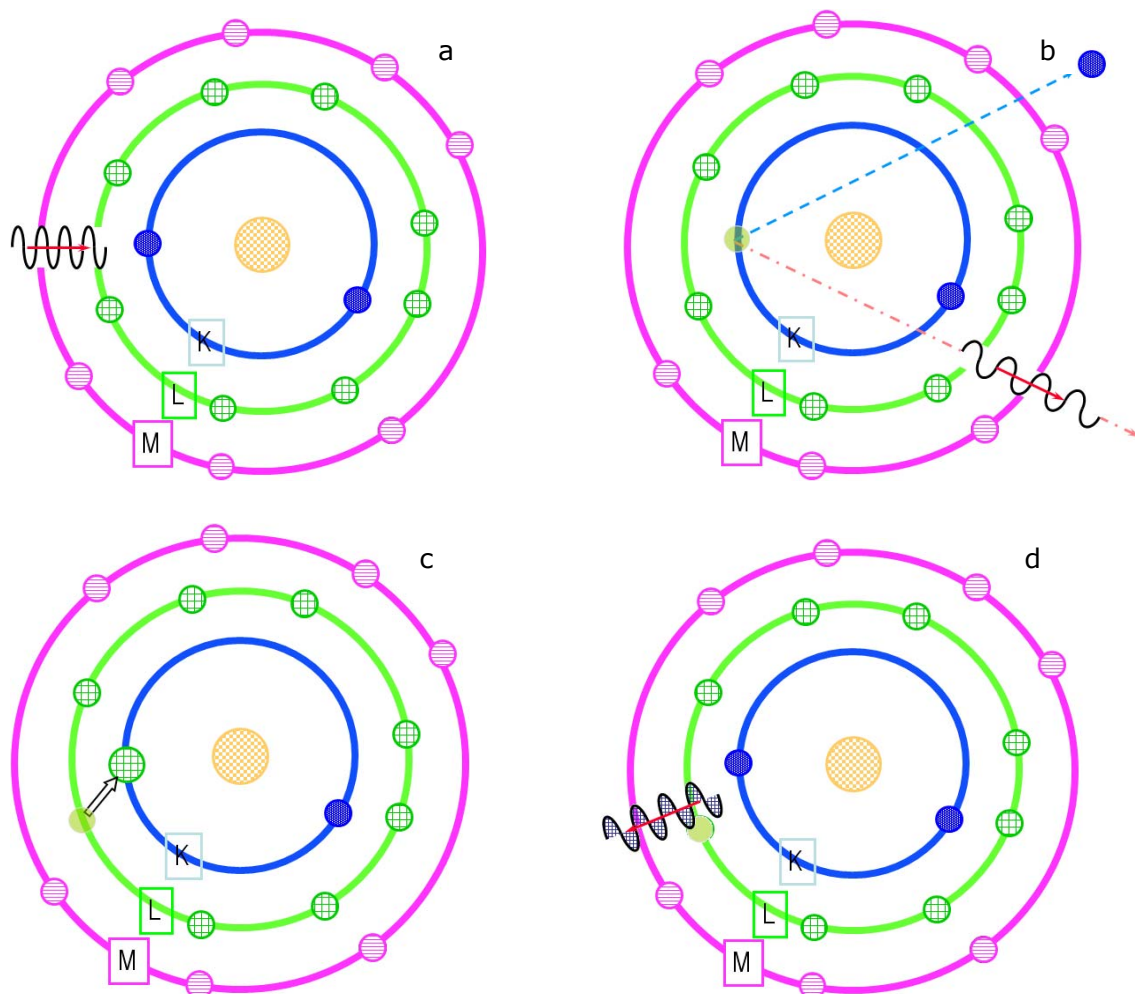
Figure 1.2 a) Principle of (μ-) EDXRF (Source: Janssens, 2005)

b) Principle of WDXRF. (Source: Jeol, Ltd., 2009)

Fluorescence is possible because the energies of x-ray photons produced by the source are in the same order of magnitude as the inner shell electrons of atoms (Janssens, 2005). Because of these comparable energies, the photons can, on collision, excite inner shell electrons and cause them to leave their shell. For this to happen, the energy of the incident photon must be larger than the binding energy of the electron. When the hit electron leaves its shell, a vacancy is created that leaves the shell unstable. To re-establish stability, an electron from another shell will fill the vacancy, which is

accompanied with the emission of X-ray energy. When electrons are transferred from an L to a K shell, the produced x-rays are called K α lines. Transfer from M to K shells produces K β lines, and from M to L, L α lines. The emitted x-rays are characteristic x-rays (Figure 1.3a-d). However, when a characteristic x-ray interacts with another shell electron within the same atom, this electron may also be excited and leave the atom. This type of electrons are Auger electrons (Figure 1.3e-f).

With EDXRF, the generated characteristic x-rays fall directly upon the detector. With WDXRF, however, these x-rays first hit a crystal that scatters and diffracts them. Depending on the lattice of the crystal and on the different wavelengths characteristic for specific atoms, the diffracted rays are dispersed in various directions. To enable capturing of all different characteristic waves there are several configurations for the crystal and the detector: (1) the crystal and detector can move according to a Rowland Circle (Joel, Ltd., 2009) (Figure 1.2b); (2) the crystal is able to change position and the detector is fixed (Horiba, Ltd., 2010) (3) in a simultaneous system, there are several crystals and detectors present (Horiba, Ltd., 2010).



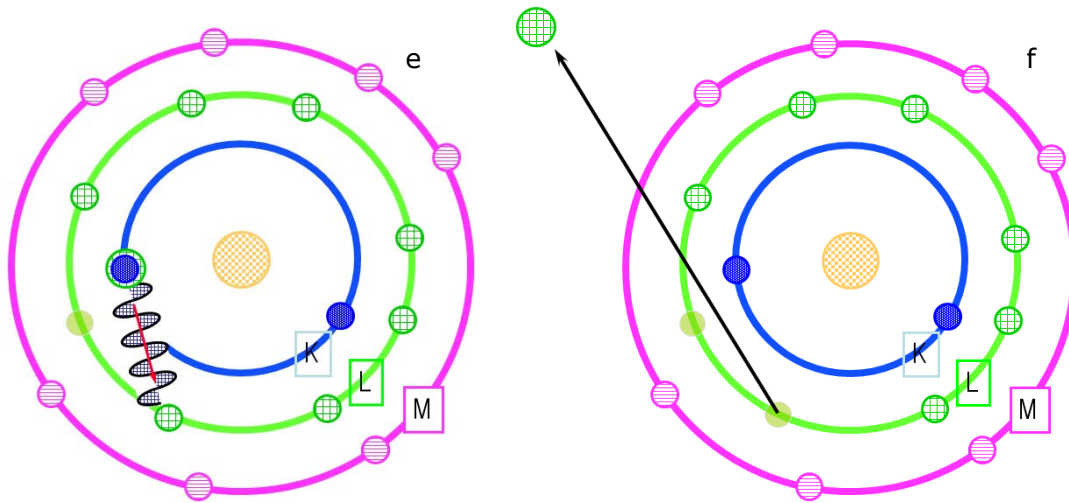


Figure 1.3 a) A source x-ray or an incident photon enters the atom with an energy that is higher than the binding energy of the inner shell electron on its path with which it will collide. b) The collision of x-ray and inner shell electron caused the electron to be ejected, in this case from the K-shell, and a vacancy is created. The high-energy x-ray is now emitted as a reduced or low energy particle. c) The vacancy in the K-shell is filled with an electron from the L-shell creating a vacancy in the L-shell. d) The electron from the L-shell has too much potential energy for the K-shell vacancy and will emit this energy as a so called K α x-ray photon, the characteristic x-ray for the L->K shell electron substitution. e) The emitted K α x-ray photon collides with another electron within the same atom. f) The K α x-ray photon collision with an L-shell electron causes this L-shell electron to be ejected, this electron is called an Auger electron. (Source: Edax, 2009)

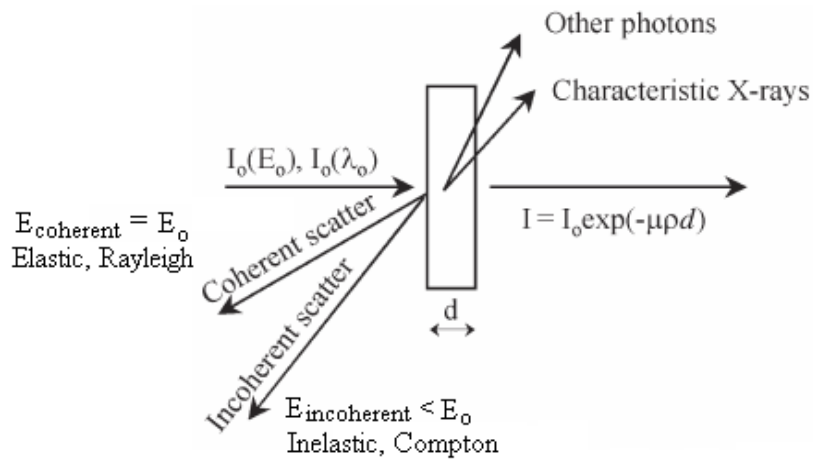


Figure 1.4 Schematic display of the effects when x-rays interact with a sample. μ is the mass attenuation coefficient. (Sources: Janssens, 2005; Edax, 2009)

Each atom in a sample has a certain number of electrons to which XRF can be applied. Since samples are made up of huge amounts of atoms and a large part of these atoms participate in shell electron transfers, all possible de-excitation routes (e.g. K α , L β) are taken (Janssens, 2005) and provide characteristic radiation. Since the correlation between wavelengths of the produced characteristic x-rays and atomic numbers of atoms is well known, it has been possible to create software that is able to translate emitted characteristic x-rays into an analysis with identified elements and their concentrations in the sample (Janssens, 2005).

When incident photons come into contact with a sample, characteristic x-ray and Auger electrons are not the only effects that occur. The photon ray could also scatter, this means that the photon changes direction after hitting the sample (*Figure 1.4*). If this scattering does not have energy loss as a result, the scattering is known as coherent, elastic or Rayleigh scattering. If energy is lost, the process is known as incoherent, inelastic or Compton scattering.

1.3 Source

The incident photons or x-rays that are used in EDXRF can be generated in a special tube (indirect) (*Figure 1.5*) or by particle-induced x-ray emission where radioactive materials emit α , β , or γ radiation (direct) (Janssens, 2005; Beeson and Mayer, 2008). In the tube a current runs through a filament. Electrons are emitted and attracted towards an anode. When these electrons hit the target material (Rh or other elements like Mo, Cu and Ti), they can undergo coherent or incoherent scattering, or be backscattered within the tube. These electrons are the producers of the continuum spectrum or Bremstrahlung (*Figure 1.6*). The electrons that are not scattered interact with the atoms of the target material and produce the characteristic x-rays for that material. These x-rays are detected in the spectral analyses of samples (Langhoff and Simionovici, 2006) (*Figure 1.6*).

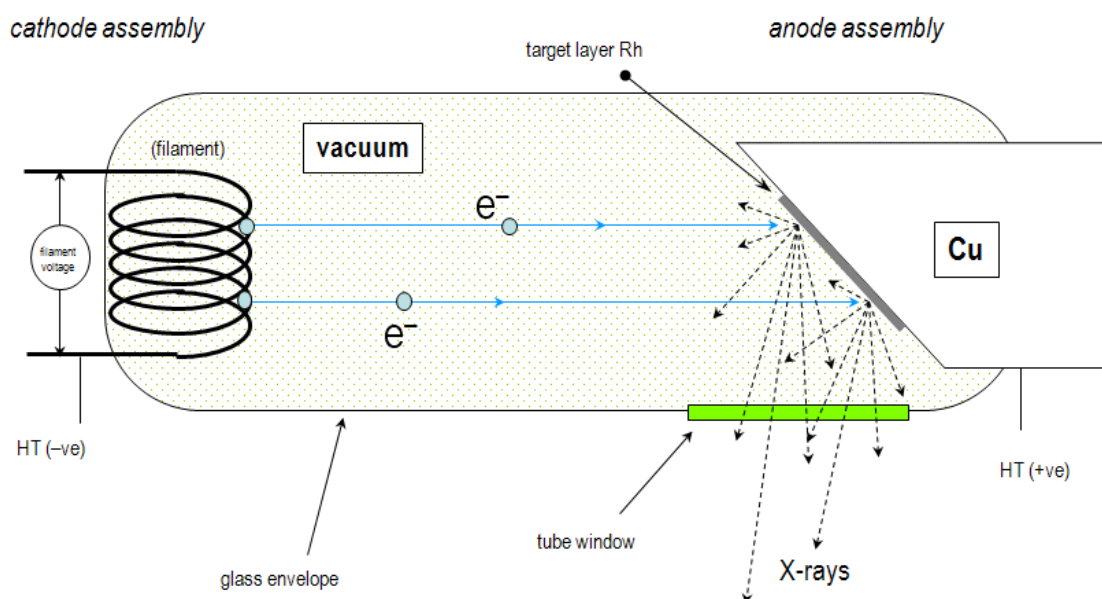


Figure 1.5 Schematics of a Rh tube that provides the incident photons or x-rays in a XRF spectrometer. (Source: Edax, 2009)

Only 1% of the produced energy falls upon the tube window as x-rays (*bottom right in Figure 1.5*) and are led through an aperture, mono-capillary or poly-capillary to the sample chamber and the sample, whereas the other 99% creates heat (Edax, 2009). For some analyses the continuum and scatter are a hindrance. In this case a primary beam filter could be used to modify the continuum spectrum and optimize it for the desired elements.

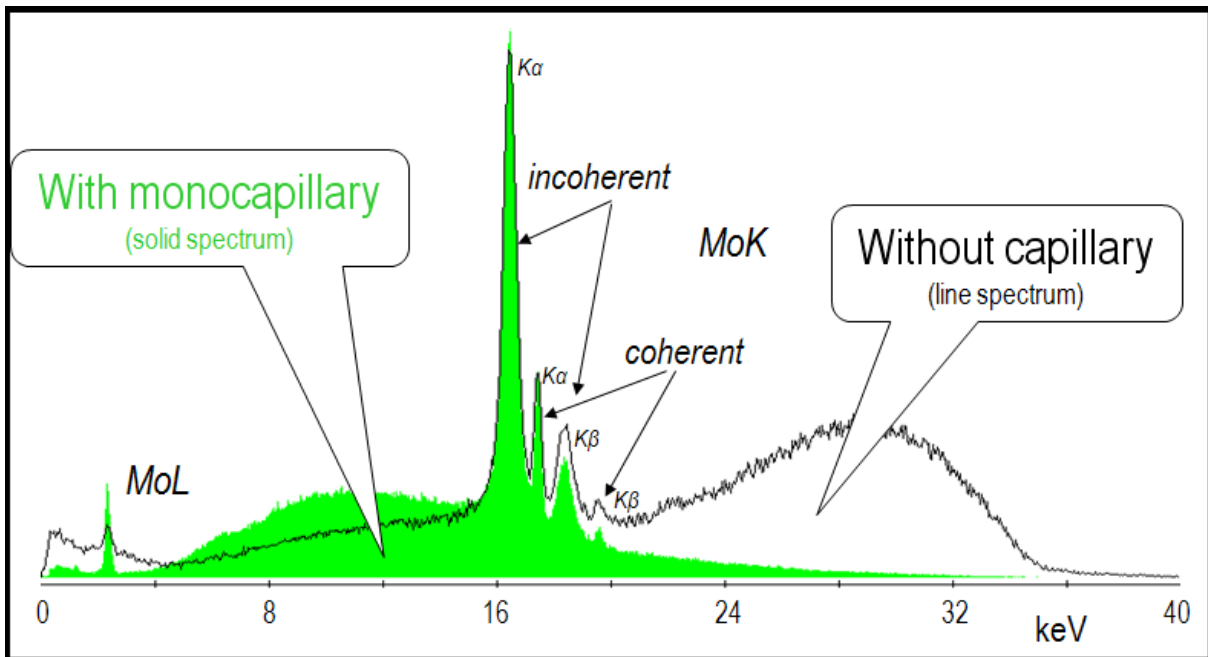
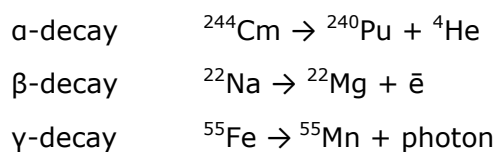


Figure 1.6 The continuous spectrum or Bremstrahlung created with a Mo anode tube for a Plexiglas sample. A monicapillary and an aperture were used. Besides the continuum, the target characteristic lines (MoL), coherent scattering ($K\alpha$ and $K\beta$) and incoherent scattering ($K\alpha$ and $K\beta$) lines are also visible. (Source: Edax, 2009)

Radioactive materials are very compact compared to tube sources. This means that portable XRF spectrometers can benefit greatly from this type of x-ray generation. Examples of direct excitation sources are ^{244}Cm , which emits α particles upon decay to form ^{240}Pu . ^{244}Cm is suitable for identification of light elements. Other examples are ^{22}Na which produces through β -decay ^{22}Mg , and ^{55}Fe which decays to ^{55}Mn through γ -decay where a proton merges with an electron to form a neutron (see reactions below) (Janssens, 2005).



The x-rays produced from direct γ excitation will produce characteristic x-rays in the same way as described earlier for indirect excitation. β -decay elements also produce characteristic x-ray as with indirect excitation, with the difference that the incident beam is not made up of photons but of electrons, which means that vacancies are created by electron-electron collisions. With α excitation, the positively charged $^4\text{He}^{2+}$ particles collide with inner shell electrons and create vacancies which are responsible for generation of characteristic x-rays (Beeson and Mayer, 2008). The energy of any incident particle should be larger than the binding energy of the electron to produce the vacancy.

1.4 Detector

The x-rays (energy) produced by the samples in EDXRF spectrometry can be captured by various types of detectors. Here, two of them will be described, the Silicon –Lithium (SiLi) detector (*Figure 1.7*) and the newer Silicon Drift Detector (SDD) (*Figure 1.8*). They are often fitted with a Beryllium window that stops all the photons with energies of 1 kV or less. These detectors transform the caught x-rays into measurable and countable voltage pulses that collectively create a spectrum (Janssens, 2005). With SiLi detectors the (characteristic) x-rays enter the detector through a Si dead layer. This layer is mostly made up of Si but doped with some Li. The Si atoms that surround the Li atoms are more weakly bonded than the Si atoms that are completely surrounded by other Si atoms. When the high energy x-rays enter the detector and hit the Si dead layer, valance electrons are freed. Because of the electric potential difference within the detector the freed electrons are pulled towards the anode. This current then enters the field effect transistor (FET) that changes the charge into pulses. These pulses go through a pulse processor that transforms the pulses further so that a single pulse provides a signal that is proportional to the energy of the entered x-ray or photon. This analog signal is digitized by an analog-to-digital converter (ADC), and the resulting digital pulses are stored in a multi-channel analyzer (MCA). In this MCA, all the pulses with the same magnitude (thus x-ray energy) are stored in the same channel. When read, the MCA creates a graph that displays these pulse distributions in the form of a spectrum.

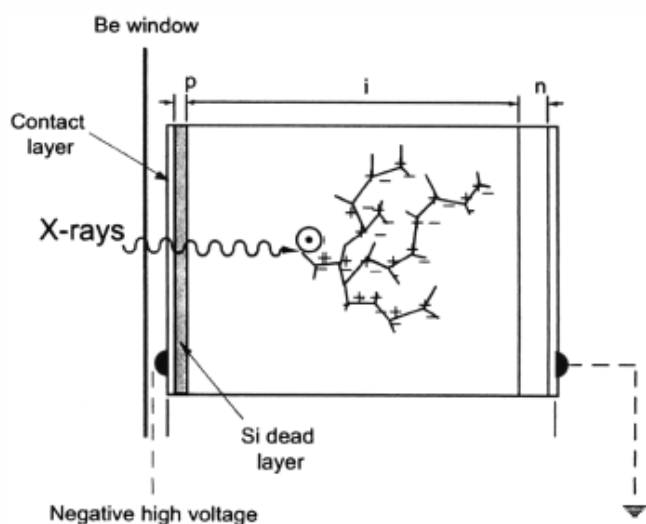


Figure 1.7 Schematics of a SiLi detector. P is positive, n is negative (Source: Janssens, 2005)

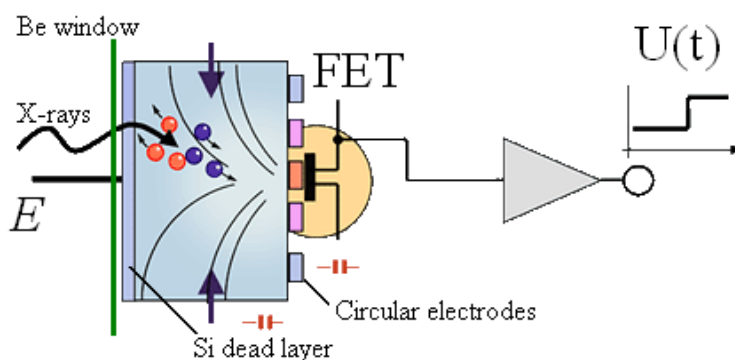


Figure 1.8 Cross-section through the center of a SDD (Source: Bruker AXS)

The energy that enters an SDD as x-rays or photons hits the Si within the detector and, together with the attached circular electrodes, frees valance electrons from the Si lattice. These electrons are freed more quickly then in a SiLi detector. The number of freed electrons is proportional to the energy that enters the detector. The electrons are

attracted to the anode and then follow the same route as the electrons in a SiLi detector, i.e. through the FET, ADC and MCA to generate a spectrum.

When examining produced spectra, one should keep in mind that not all lines necessarily represent elements. As discussed before, other peaks may appear such Rayleigh and Compton peaks, diffraction peaks due to the reflectiveness of the sample surface, or escape and sum peaks that are artifacts from the detector. An escape peak of an element that is usually abundant in the sample has an energy of 1.74 kV less than that of the element itself (1.74 kV is the energy of Si). A sum peak is formed when the energies of two elements hit the detector at precisely the same moment. The detector does distinguish these two elements as separate but takes them as one, with an energy made up of the two elemental energies combined.

1.5 Micro-XRF

Micro-Energy Dispersive X-ray Fluorescence is based on extracting chemical information from a small spot, the area of the primary beam, but the technique uses essentially the same components and options as standard XRF. XRF spectroscopy at micro-spot scale was developed owing to progresses made in X-ray optics (Janssens, 2005; Malzer & Kanngießer, 2005). The innovations concerned the capillary optics (mono- and polycapillary) that enabled creating increasingly smaller spot sizes (Kumakhov & Komarov, 1990), down to 10 μm (HORIBA, Ltd., 2010) for bench-top apparatuses. *Figure 1.9* gives an impression of the difference in surface area between apertures for spot sizes in the order of mm, mono-capillaries for spot sizes on the order of 100s of μm , and poly-capillaries for spot sizes of 10s of μm (Edax, 2009).

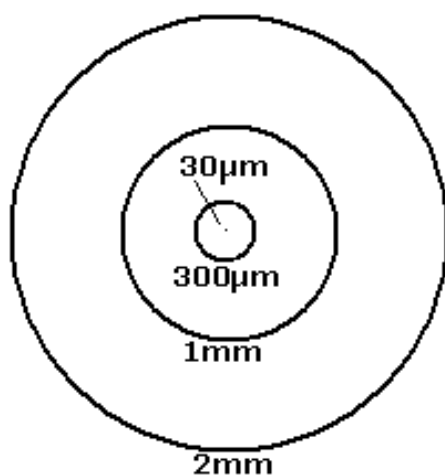


Figure 1.9 1 and 2 mm apertures and 300 and 30 μm capillaries drawn to scale. The 2-mm aperture has a surface that is 4 times larger than the 1-mm aperture, 44 times larger than the 300- μm capillary and 4445 times larger than the 30- μm capillary.

Poly-capillary lenses are composed of large numbers of 3-5 μm channels (*Figure 1.10*). These channels are made of glass, and curve towards a single point where the x-ray

beam is focused. Because of this type of focusing, poly-capillary lenses create high-intensity, micro spot x-ray beams (Janssens, 2005) perfect for analyzing micro structures in samples.

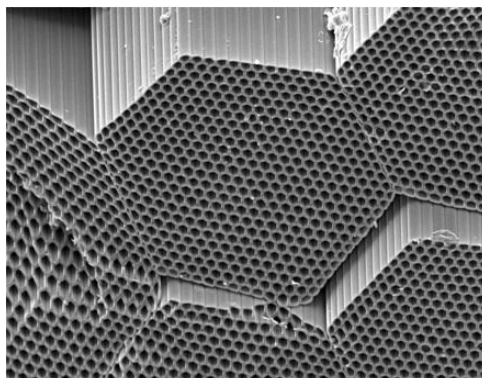


Figure 1.10 Enlargement of the channels in a poly-capillary, the channels have diameters of 3-5 μm (Source: Edax, 2009)

The small spot sizes imply that $\mu\text{-XRF}$ spectrometry can be used for analyses at small spatial resolution, for example to determine the composition of individual fine layers or small mineral clusters within a larger geological sample, or of element clusters in a synthetic material (Molloy & Sieber, 2008), or to assess whether a sample is homogeneous or heterogeneous at small scale (Miller, 2005; Tsuji et al., 2008). Minimal sample preparation and the non-destructive character form another important difference with standard XRF, for which samples are usually ground to a fine, homogeneous powder needed to prepare pellets of glass beads. Samples can also remain intact because the $\mu\text{-XRF}$ has a relatively large sample chamber (Behrends & Kleingeld, 2009), so that cutting of larger samples is often not needed. Another advantage is that, apart from single spot analysis, $\mu\text{-XRF}$ software is capable of providing compositional line scans and 2-D element maps (Miller, 2005).

An advantage of $\mu\text{-XRF}$ is that it can perform under air conditions and does not need vacuum, unlike other micro-scale analytical techniques such as a Scanning Electron Microscope (Miller, 2005; Behrends & Kleingeld, 2009). However, for measuring low-Z elements in geological and biological samples vacuum conditions are still needed to prevent attenuation of emitted x-rays by interaction with air particles. Another disadvantage of $\mu\text{-XRF}$ might be that only an energy-dispersive variant is currently available (Behrends & Kleingeld, 2009). A wavelength-dispersive detection system would increase the spectral resolution and data quality, but a drawback of WD- $\mu\text{-XRF}$ would be the relatively high cost (HORIBA, Ltd., 2010).

Theoretical detection limits of $\mu\text{-XRF}$ spectrometry lie between 0.2 and 4% according to Ginibre et al. (2007) (*Figure 1.11*), and appear to be good compared to other XRF techniques (EDS, WDS). Others have suggested that practical detection limits are

between 0.007 and 0.062 ‰ for elements with atomic numbers between 19 and 30, i.e. from K to Zn (Papadopoulou et al., 2006). However, it needs to be verified if these detection limits can actually be reached in practice for various setups. A final limitation is that data reduction software not always meet the requirements for accurate and reliable analysis of geological samples with the same quality as standard XRF.

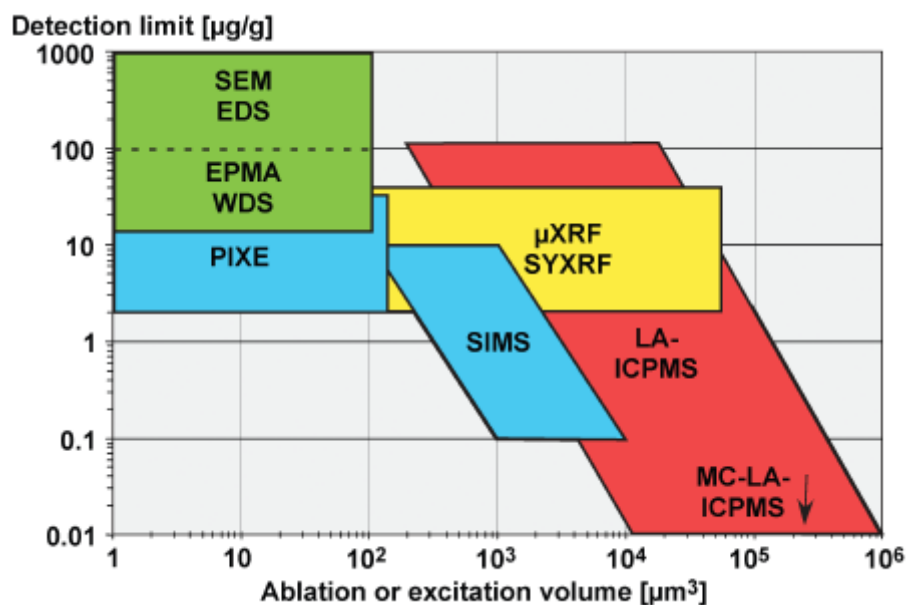


Figure 1.11 Detection limits for various micro-analytical techniques (Source: Ginibre et al., 2007)

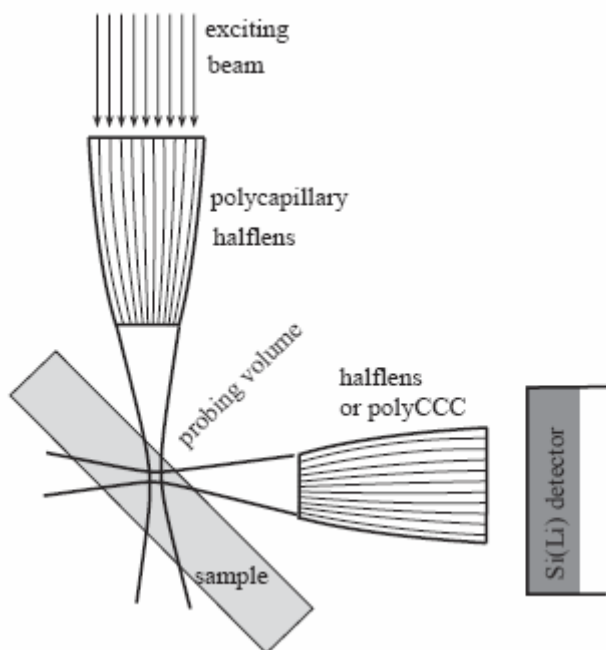


Figure 1.12 Schematics of confocal setup for 3D µ-XRF spectrometry (Source: Malzer & Kanngießer, 2005)

Besides 2D measurements, µ-XRF technology has recently expanded into 3D analyses (Malzer & Kanngießer, 2005; Tsuji et al., 2008). The 3D analyses are performed by a confocal setup (the use of two lenses) where the first is located within the excitation channel and the second in the detection channel (Figure 1.12), a polycapillary half- or

fullens and a polycapillary half lens or conical collimator respectively (Xiao-Yan et al, 2007; Malzer & Kanngießer, 2005). The two overlapping beams cover a micro-volume that can be analyzed because the lens in front of the detector works as a shield, so that only X-rays created in the volume reach the detector (Malzer & Kanngießer, 2005). Applications for this type of μ -XRF analysis are plentiful in geology, biology and archeology, such as analysis of solid inclusions in diamonds and of fluid inclusions in quartz (Vincze et al., 2004), seawater constituents incorporated in exoskeletons of marine animals (Janssens et al., 2004), and paint layers (Kanngießer, 2005).

Chapter 2: Experimental determination of optimal measurement conditions for geological samples

2.1 Introduction

In order to produce reliable results with a μ -XRF instrument, fitted with an SDD (Silicon Drift Detector), it is necessary to determine the optimal conditions for measurements. Parameters to be discussed here are *Beam size* (30- μ m, 1-mm and 2-mm), *Amplifier time* (ranging from 0,5 – 12,8 μ s), *Voltage* (for geological purposes ranging from 10/20 – 50 keV), *Current* (for geological purposes ranging from 100 – 1000 μ A), and *Live time*.

The *beam size* affects the strength of the signal that is received. The 30- μ m polycapillary results in a stronger signal than the 1- or 2-mm apertures. And the 2-mm aperture results in an approximately 4 times stronger signal than the 1-mm aperture.

The *amplifier time* is the time during which the detector is open for receiving signal. Changing the amplifier time affects the resolution, i.e. the peak width defined as the full width – half max of the Manganese peak.

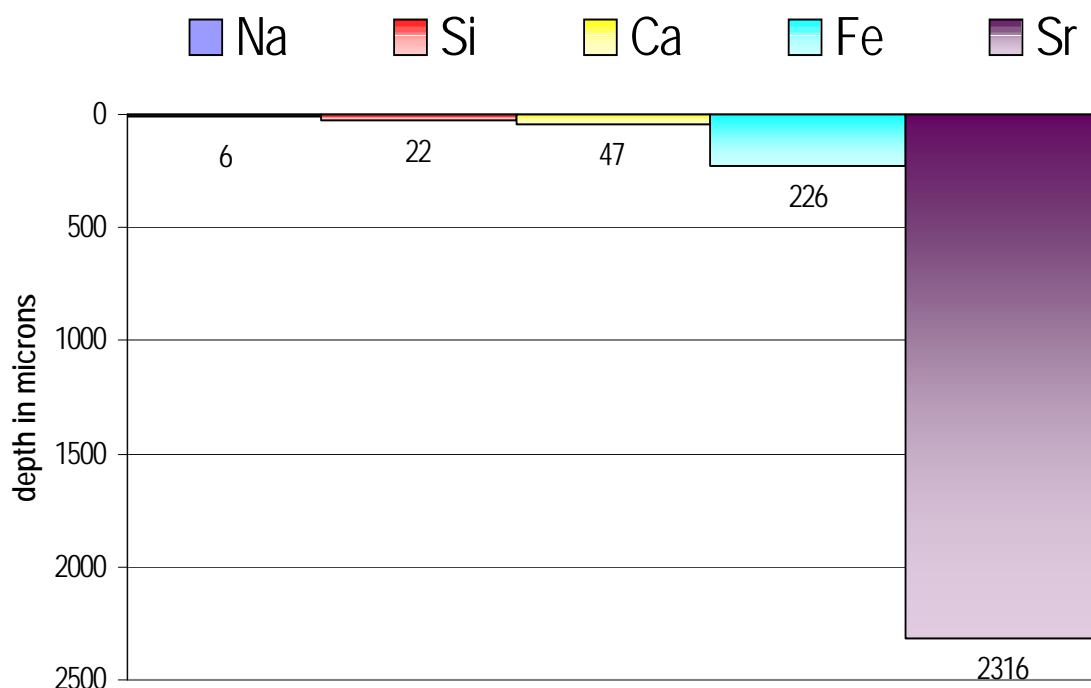


Figure 2.1 Critical depths of Na, Si, Ca, Fe, and Sr in a silica glass standard (Source: Edax, EDXRF training lecture Properties and Production of X-rays)

The *voltage*, or tube voltage, affects the pull on the free electrons. If the voltage increases, the speed of electrons also increases so that they reach their target sooner. Consequently, the emitted X-rays will have increased energies (higher keV) (*source*:

Edax, EDXRF training lecture Properties and Production of X-rays). With higher voltages, for example 50 keV instead of to 20 keV, the beam reaches a deeper part of the sample and will excite heavier elements. This effect may negatively influence the results (*Figure 2.1*). For example, Fe has a much larger critical depth than Si, and if high voltages are applied, deeper parts of the sample are reached, so that Fe is measured in a larger sample volume than Si. Thus the Fe yield will be too high compared to that of Si. This problem can be minimized by using lower voltages. Another effect of voltage is that it should be tuned, depending on the weight of the element, to measure in the optimal excitation region of the continuum spectrum (*Figure 2.2a-d*) (source: Edax, EDXRF training lecture Properties and Production of X-rays).

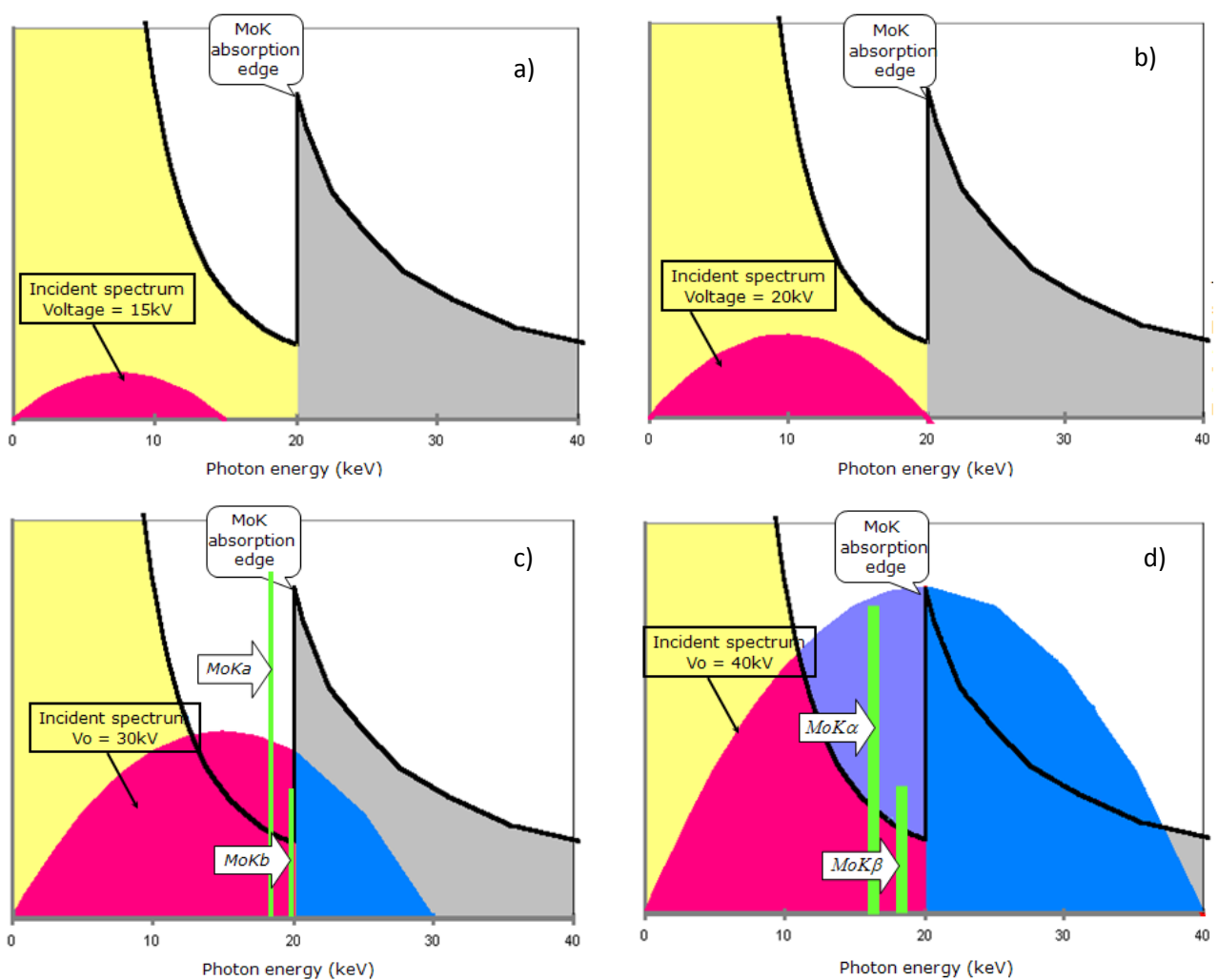


Figure 2.2 a) The effect of tube voltage and associated continuum spectrum on the appearance of MoK lines in a Molybdenum-bearing sample. (Tube voltage = 15kV) No MoK peak is yet visible. *b)* There is no spectral energy (pink) larger than the MoK absorption edge energy. (Tube voltage = 20kV) No MoK peak is yet visible. *c)* Part of the incident continuum has an energy larger than the MoK absorption edge (blue). (Tube voltage = 30 kV) The MoK peak appears, but not in the optimal excitation region of the continuum spectrum. *d)* Approximately half of the incident continuum has an energy larger than the MoK absorption edge (blue). (Tube voltage = 40kV) The MoK peak is now in the optimal excitation region of the continuum. (Source: Edax, EDXRF training lecture Properties and Production of X-rays)

The *current*, or filament current, determines the amount of electrons available for exciting the Rh target layer. With more electrons available for exciting the Rh, a more intensive X-ray beam is created.

The *live time*, is the time during which a single spot is effectively measured. Increasing the live time increases the accuracy of the measurement.

Several effects should be taken into account when determining the optimal measuring conditions, depending on the parameter to be examined. *Dead time* is important since it controls the total run time of tests. Dead time (Dtm%) is the interval the detector needs to process a certain amount of incoming pulses so that it is not available for receiving new pulses. A high dead time results in a longer measurement time. A maximum acceptable Dtm% limit is approximately 40%. Varying the amplifier time affects the *resolution* (Res). This effect should be taken into account, since narrower peaks result in better peak separation and thus in improved element identification.

2.2 Methods

The procedure for determining optimal measuring conditions varies for each parameter. The selection of the appropriate *beam size* or *live time* depends on the nature of the experiment. For a quick screening to determine which elements a specimen contains and which should be mapped, the 2-mm aperture is a good choice because a beam of this size guarantees a high return. Usually several different locations should be measured to ensure that all the elements present are identified. An appropriate live time to obtain sufficiently accurate data for this purpose would be 30 seconds. For detailed mapping, the 30- μm polycapillary beam can be used due to an even higher return and accuracy. This beam is ~ 4450 times smaller than the 2-mm beam and will thus enable measuring very small grains and identify variations at much smaller scales. In this case, much shorter live times ($< 1\text{s}$) can be selected to create a reasonable accurate map within an acceptable length of time. In the present tests a live time of 10 seconds was chosen and the experiments were done with the three available beam sizes, so that optimal conditions were determined for each beam size.

The *optimal amplifier* time was determined by finding the highest resolution or smallest peak widths in an experiment on a randomly selected geological material in this case a pyroxene. Voltage (keV) and current (μA) conditions were taken that are generally suitable for geological samples. The lower and upper boundaries were approximately 20 keV, 100 μA and 50 keV, 1000 μA , respectively. Because 20 keV will be frequently used in practice, an experiment was performed at 20 keV and 1000 μA . These three parameter sets were tested for all available amplifier times (0.5 – 12.8 μs), and for the 30- μm and 2-mm beam sizes, as they give higher returns than the 1-mm size. From

these experiments the optimal amplifier time was determined by optimizing the resolution, while taking the Dtm% into account.

To determine the *optimal voltage* for geological samples, tests were executed on 3 metal standards: Cu, Al and Cu-Al alloy. The combination of Al and Cu was chosen because these elements represent the lower and upper voltage limits (1.49 keV and 8.03 keV) respectively, for the common group of elements measured in geological materials with the μ -XRF. Each of the standards were analyzed with all three beam sizes (30- μ m, 1-mm, 2-mm), at voltages ranging from 10 to 50 keV at 5keV intervals, and a current of 100 μ A. For each run the standard, beam size, live time, amplifier time, current, voltage, Dtm%, and maximum intensity (maximum amount of counts) were recorded. The amplifier time of 6.4 μ s was taken, based on the outcome of the optimal amplifier time experiment mentioned above. The optimal voltage for each beam size and standard was eventually determined by considering the maximum intensities and Dtm%.

Tests for *optimal current* conditions for the analysis of geological samples were carried out following similar procedures as described above for the optimal voltage. In this case, however, the current was allowed to vary, from 100 – 1000 μ A with 100 μ A steps, and a voltage of 20 keV was used. The amplifier and live times remained the same, also previously determined. The analyses were again done on the three standards with three beam sizes, and maximum intensities and Dtm% were recorded. The optimal currents, depending on sample and beam size, were determined by taking the associated Dtm% into account, ensuring that it did not exceed 40%.

The combined results of the tests provide a set of preferred parameter settings suitable for the analysis of geological materials.

☞ 2.3 Optimal Amplifier Time Test ☞

2.3.1 Results

The results of tests on the optimal amplifier time can be found in *Table 2.1*. They show that with increased amplifier times the Dtm% increases, both for the 30- μ m and the 2-mm spot. The Dtm% also increases with higher voltages and currents.

The resolution only changes with the selection of the amplifier time, independent of other variables.

2.3.2 Discussion and Conclusions

When taking into account the resolution and Dtm% results, we conclude that 6.4 μ s is the optimal amplifier time. The Dtm% values are too high at 50 keV and 1000 μ A, but these conditions are not likely parameters that will be used when examining geological

samples. Also, the Dtm% for 20 keV and 1000 μA are too high for the 30- μm but reducing the current will resolve this problem.

Amplifier time	Voltage (keV)	Current (μA)	Resolution	Dtm% 30- μm	Dtm% 2-mm
0.5	20	100	163.1	1	0
0.5	20	1000	163.1	10	2
0.5	50	1000	163.1	16	7
0.8	20	100	153.7	2	1
0.8	20	1000	153.7	14	4
0.8	50	1000	153.7	22	11
1.6	20	100	143.3	3	1
1.6	20	1000	143.3	25	8
1.6	50	1000	143.3	38	20
3.2	20	100	137.6	6	2
3.2	20	1000	137.6	41	14
3.2	50	1000	137.6	59	35
6.4	20	100	135.4	14	6
6.4	20	1000	135.4	65	28
6.4	50	1000	135.4	83	59
12.8	20	100	137.8	23	9
12.8	20	1000	137.8	87	45
12.8	50	1000	137.8	96	81

Table 2.1 Results of the optimal amplifier time experiments

2.4 30- μm Polycapillary Voltage Tests

2.4.1 Results

The results of this experiment are shown in *Sheet 2.1*. The results marked **bold** are those with the highest counts. The associated voltages are 35 keV and 45-50 keV for Al and Cu respectively. Dead times do not exceed 35% and range up to 33% for the highest counts results.

2.4.2 Discussion and Conclusions

From the 30- μm polycapillary voltage tests it appears that Dtm% values are lower than the maximum allowed limit of approximately 40%, irrespective of the testing material used. In the tests on Cu at voltages of 40 – 50 keV and a relatively low current of 100 μA the Dtm% approached the limit. Hence, there is much room for increasing the current at these higher voltages. The Al experiment shows a maximum intensity at 35 keV, as does the Al in the Cu-Al alloy. The Cu experiment shows a maximum intensity at 45 keV. These data indicate that the maximum voltage to be used for measuring light elements should be approximately 35 keV, considering the maximum intensities and acceptable Dtm%. For heavy elements the maximum voltage should be approximately 40 keV, since this will still produce high intensities at relatively low Dtm%, leaving some space for

increasing the current if desired. However, considering the discussion on voltage in the introduction (cf. *Figure 2.1*), it would be more appropriate to use voltages that are 5 keV lower than referred to above. This implies that the maximum voltage to be used should be around 30keV for lighter elements and 35 keV for heavy elements.

☞ 2.5 Aperture Voltage Tests ☞

2.5.1 Results

Again, the results with the highest counts are marked bold (*Sheet 2.2* and *2.3*). Both spots show low Dtm%, up to 14%, with the exception of the 2-mm Cu-test, which shows a maximum Dtm% of 35%. The voltages that accompany the maximum counts range from 35 keV for AL to 50 keV for Cu.

2.5.2 Discussion and Conclusions

In the aperture voltage tests Dtm% values remained sufficiently, which implies that there is room to increase the current. Trends for the light elements are similar to those of the polycapillary test, showing maximum intensities of 35 – 40 keV. For the heavy elements (e.g., Cu) there is no maximum intensity but a continuous positive correlation between intensity and voltage. The preferred maximum voltage to be used for analyses of light elements is 35 keV. A maximum voltage of 40 keV is preferred for heavy elements when using an aperture, based on the value determined for the 30- μ m polycapillary. However, as with the 30- μ m polycapillary, it would be more appropriate to subtract 5 keV implying that a maximum of 30 keV should be taken for light elements, and 35 keV for heavy elements.

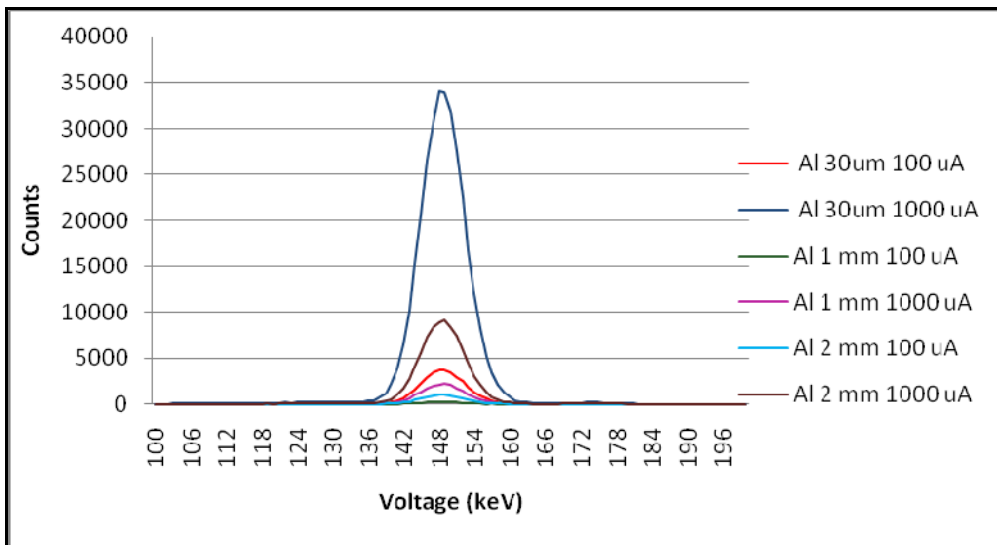
After gaining further experience, it appeared that a voltage of 20 keV is adequate for the analysis of geological materials, both with the polycapillary and with the apertures.

☞ 2.6 30- μ m Polycapillary Current Tests ☞

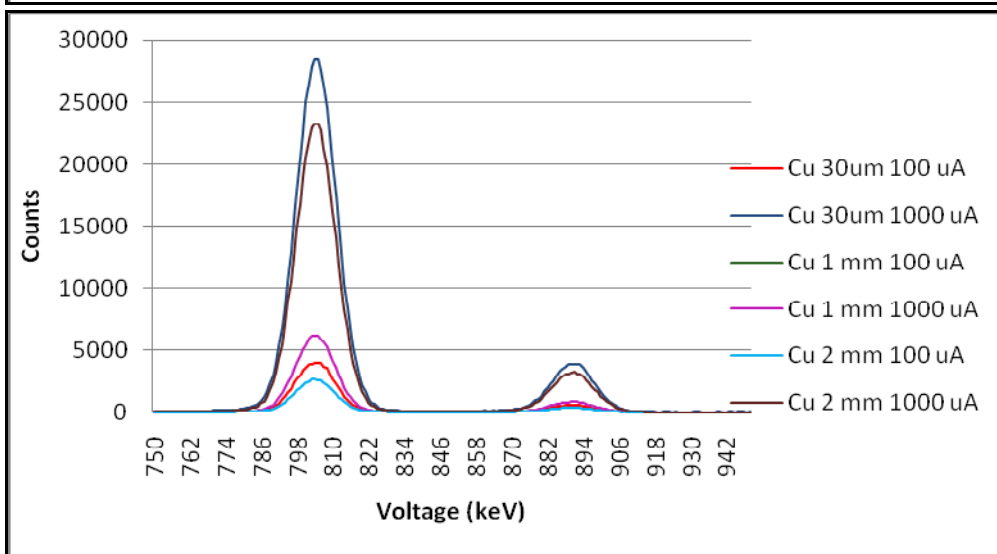
2.6.1 Results

The results of this experiment are shown in *Sheet 2.4*. For these test results the conditions with Dtm% of equal or lower than 40% are in bold numbers. For Al high currents can still be used, the tests give a maximum Dtm% of 40% at 900 μ A. The test for Cu shows a smaller usable current range of 100 to 400 μ A. The Cu-Al alloy displays almost the exact Dtm% as the pure Al test. The current has a positive relation with the amount of counts that were measured.

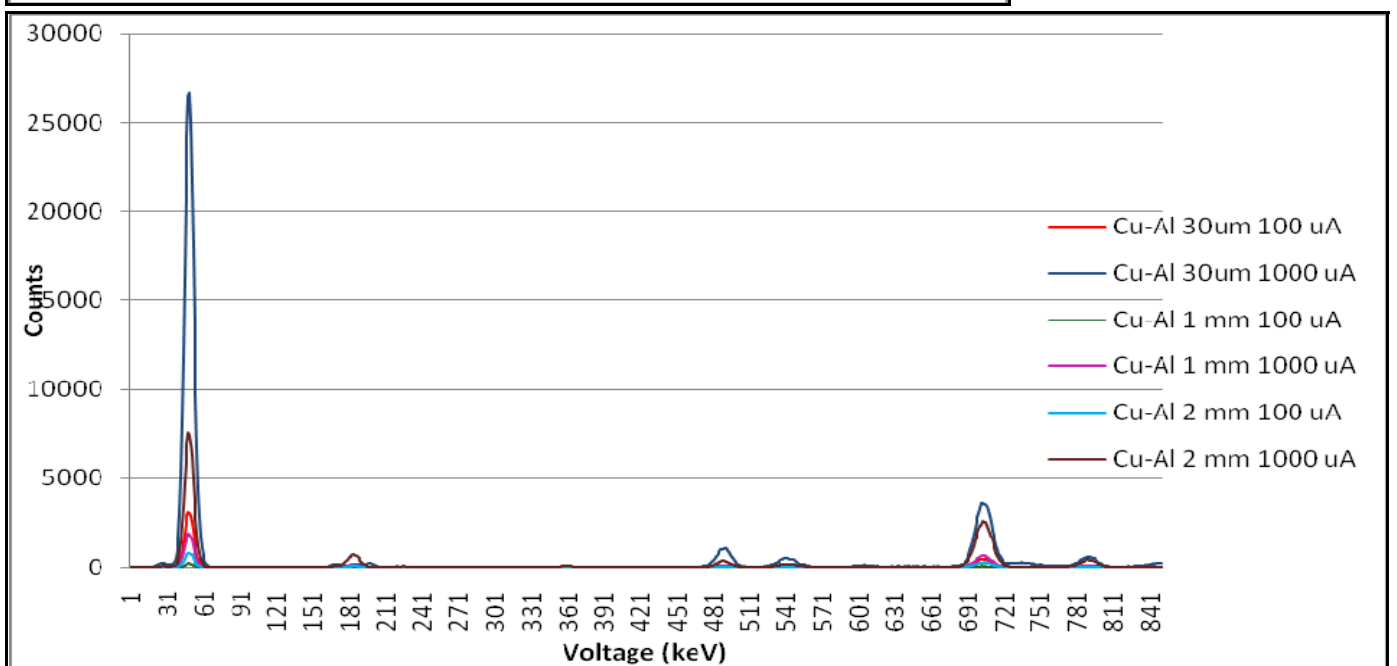
A multicolor overlay of spectra from the current experiment for the three standards, the three beam sizes and currents of 100 and 1000 μ A is shown in *Figure 2.3a-c*.



a) Zoomed-in portion of the full-scale Spectra of Copper:
 Beam sizes: 30- μ m, 1-mm and 2-mm.
 Voltage: 20 keV. Currents: 100 μ A and 1000 μ A. Amplifier time: 6.4 μ s.
 Live time: 10 sec.



b) Zoomed-in portion of the full-scale Spectra of Aluminum:
 Beam sizes: 30- μ m, 1-mm and 2-mm.
 Voltage: 20 keV. Currents: 100 μ A and 1000 μ A. Amplifier time: 6.4 μ s.
 Live time: 10 sec.



c) Zoomed-in portion of the full-scale Spectra of Copper/Aluminum:
 Beam sizes: 30- μ m, 1-mm and 2-mm.
 Voltage: 20 keV. Currents: 100 μ A and 1000 μ A. Amplifier time: 6.4 μ s.
 Live time: 10 sec.

Figure 2.3 a-c Current experiment, multicolor overlay spectra, the x-axis shows the voltage in keV and the y-axis shows the intensity.

2.6.2 Discussion and Conclusions

The 30- μm polycapillary current data obtained from the Al and Cu-Al alloy standards show linear relationships between intensity and current. For the Cu standard the trend deviates from linearity at currents of 800 μA and up. This effect is also seen in the associated Dtm%. Considering the Dtm% values and the linear relations, we conclude that currents up to 900 μA can be used for light elements and currents up to 400 μA for heavy elements at 20 keV.

2.7 Aperture Current Tests

2.7.1 Results

Sheet 2.5 and 2.6 show the results of this experiment. Almost all the Dtm% are below 40% (in **bold**) with the exception of the results for the 2-mm spot on Cu at high currents ($>700 \mu\text{A}$). The lowest recorded Dtm% was 4% for the 1-mm Cu-test for both 100 and 200 μA . Counts increase steadily with the current.

2.7.2 Discussion and Conclusions

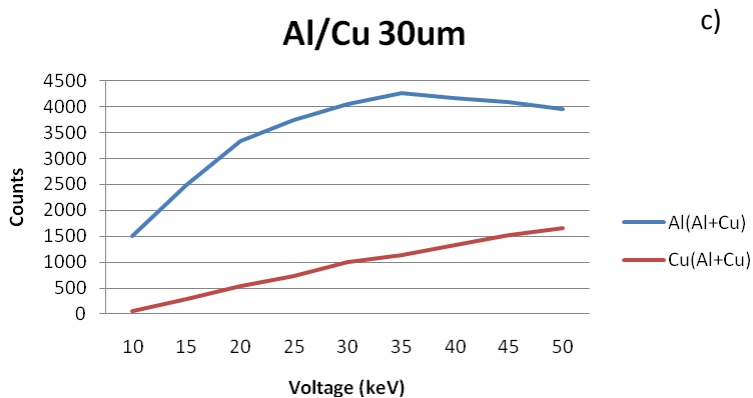
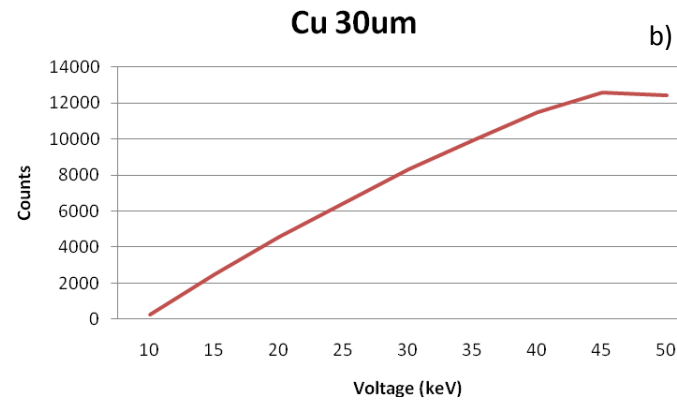
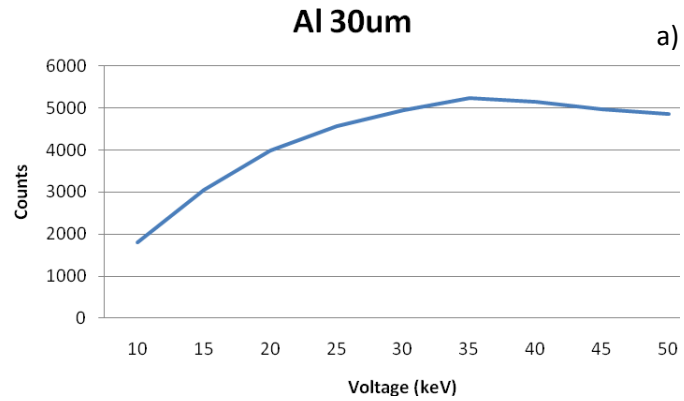
Current-experiment data for the 1- and 2-mm apertures also show positive linear relations between intensity and current with a slight deviation at $\sim 750 \mu\text{A}$ for the Cu standards. Except for the test of the 2-mm aperture on Cu, Dtm% values are far below the 40% limit over the entire current range taken. The 2-mm aperture test on Cu showed that Dtm% remains acceptable below 600 μA . We conclude that, when using apertures, any current up to the tested 1000 μA can be used for light elements, and up to 600 μA for heavy elements.

Again, from further experience it appeared that lower currents decrease the diffraction peaks, so that working with lower currents, for example 100 μA , is preferable.

The multicolor overlay spectra (*Figure 2.9a-c*) from the current experiments show that the maximum intensity increases at higher currents. Also, the 30- μm polycapillary provides the highest signal, followed by the 2-mm aperture and the 1-mm aperture. It also appears that changing the beam size from 30- μm to 2-mm has a larger effect on the results obtained from the Al standard than from the Cu standard. These spectra illustrate the large differences that low and high currents and various beam sizes produce.

Sheet 2.1: Voltage Experiment with 30- μ m beam

Al			Cu			Al(Al+Cu)		Cu(Al+Cu)		
keV	Counts	Dtm%	keV	Counts	Dtm%	keV	Counts	keV	Counts	Dtm%
10	1792	4	10	265	5	10	1495	10	48	3
15	3040	5	15	2501	11	15	2480	15	287	6
20	3979	7	20	4573	16	20	3331	20	544	8
25	4577	8	25	6465	21	25	3747	25	738	10
30	4950	9	30	8315	25	30	4050	30	999	11
35	5235	10	35	9941	29	35	4271	35	1130	12
40	5137	10	40	11507	31	40	4161	40	1325	12
45	4973	11	45	12580	33	45	4098	45	1531	13
50	4852	11	50	12402	35	50	3963	50	1654	14

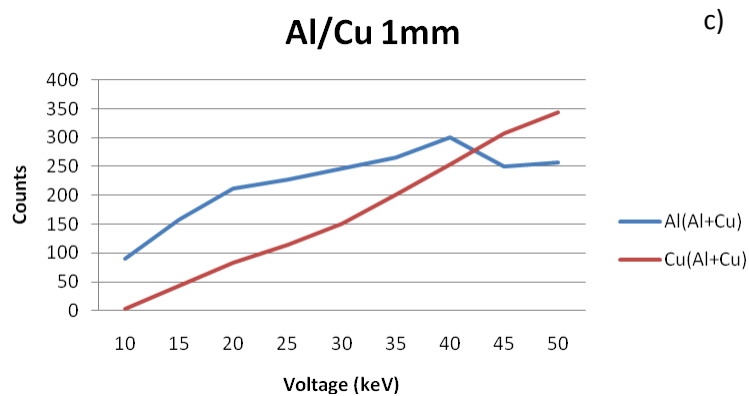
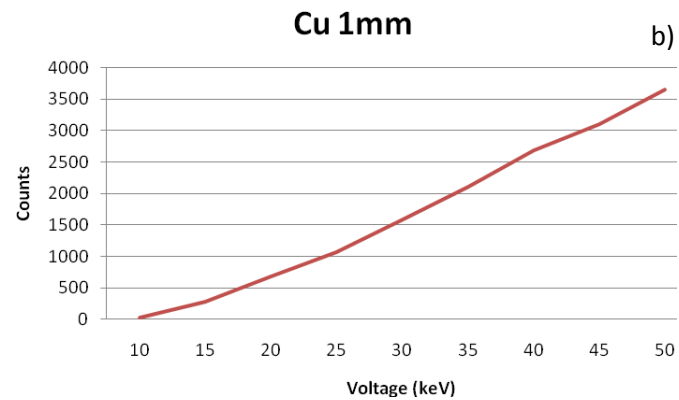
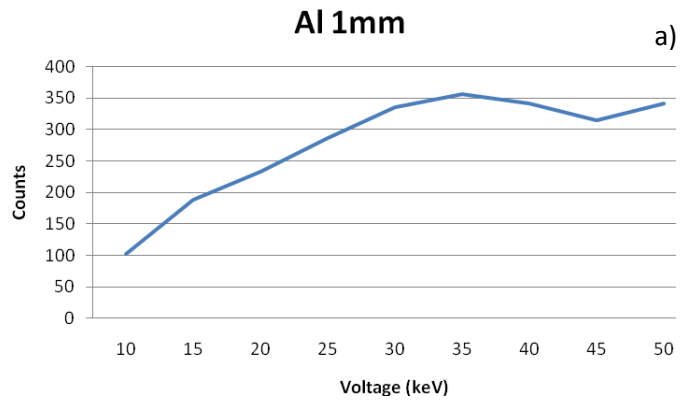


Beam size: 30- μ m
 Amp. Time: 6,4 μ Sec
 Current: 100 μ A
 Live time: 10 Sec

Table Voltage experiment data for the 30- μ m polycapillary
Figure: Voltage experiment data for the 30- μ m polycapillary on the *a)* aluminum sample, *b)* copper sample, *c)* copper/aluminum alloy sample

Sheet 2.2: Voltage Experiment with 1-mm beam

Al			Cu			Al(Al+Cu)		Cu(Al+Cu)		
keV	Counts	Dtm%	keV	Counts	Dtm%	keV	Counts	keV	Counts	Dtm%
10	103	2	10	23	4	10	90	10	4	4
15	188	3	15	281	6	15	157	15	43	5
20	233	3	20	685	7	20	212	20	84	5
25	287	3	25	1066	7	25	227	25	114	4
30	335	5	30	1591	8	30	247	30	151	6
35	357	6	35	2113	10	35	265	35	201	6
40	341	6	40	2685	11	40	300	40	253	7
45	315	7	45	3102	12	45	250	45	307	8
50	342	9	50	3656	14	50	257	50	343	8

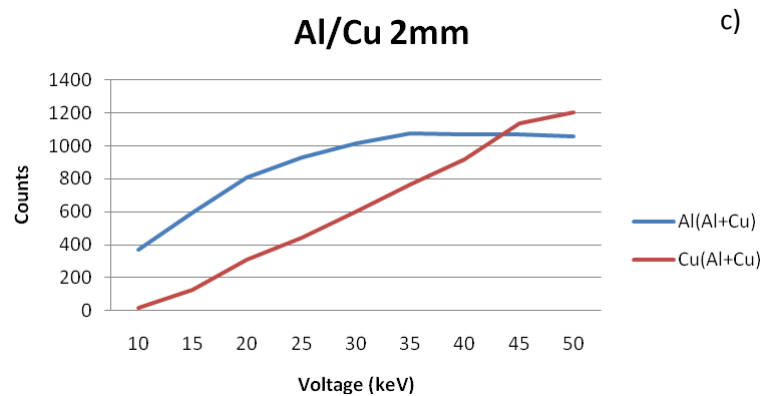
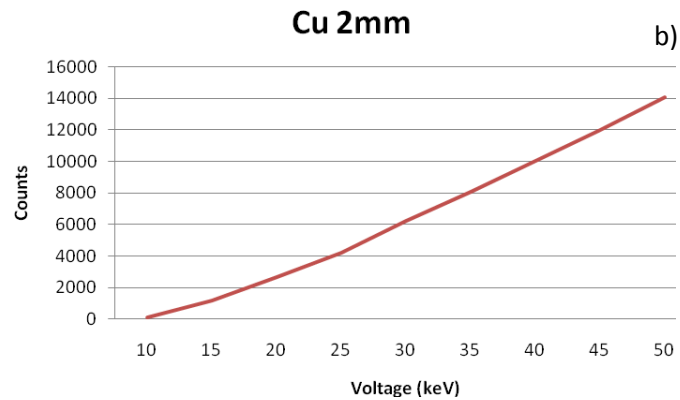
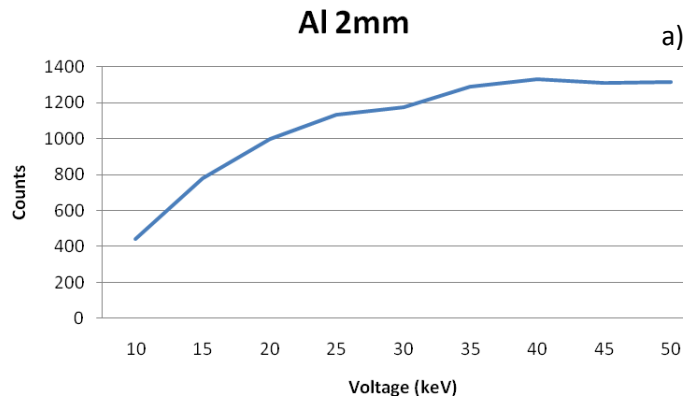


Beam size: 1-mm
 Amp. Time: 6,4 μ Sec
 Current: 100 μ A
 Live time: 10 Sec

Table Voltage experiment data for the 1-mm aperture
 Figure Voltage experiment data for the 1-mm aperture on the a) aluminum sample, b) copper sample, c) copper/aluminum alloy sample

Sheet 2.3: Voltage Experiment with 2-mm beam

Al			Cu			Al(Al+Cu)			Cu(Al+Cu)		
keV	Counts	Dtm%	keV	Counts	Dtm%	keV	Counts	keV	Counts	Dtm%	
10	443	2	10	91	4	10	369	10	15	3	
15	781	2	15	1190	8	15	595	15	128	4	
20	1000	4	20	2640	12	20	806	20	309	6	
25	1135	5	25	4240	15	25	930	25	440	7	
30	1177	5	30	6235	20	30	1012	30	602	7	
35	1287	8	35	8080	24	35	1074	35	768	8	
40	1329	8	40	10056	28	40	1070	40	915	10	
45	1309	10	45	12020	31	45	1068	45	1137	11	
50	1314	10	50	14068	35	50	1055	50	1206	12	

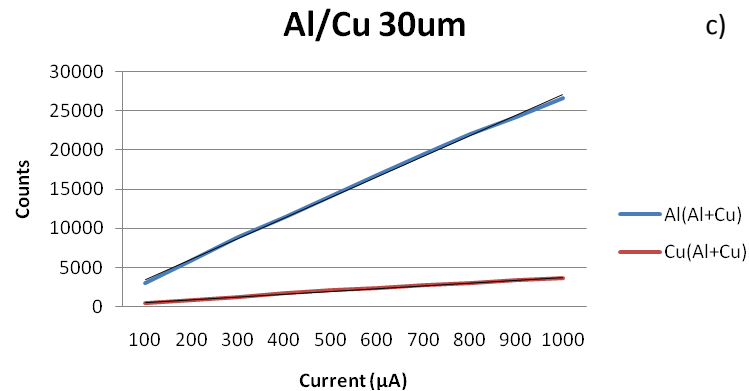
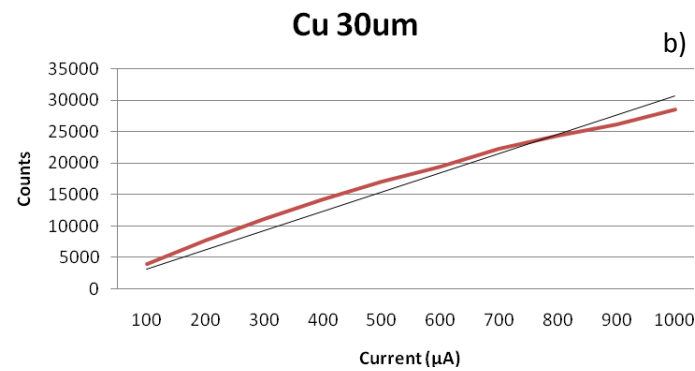
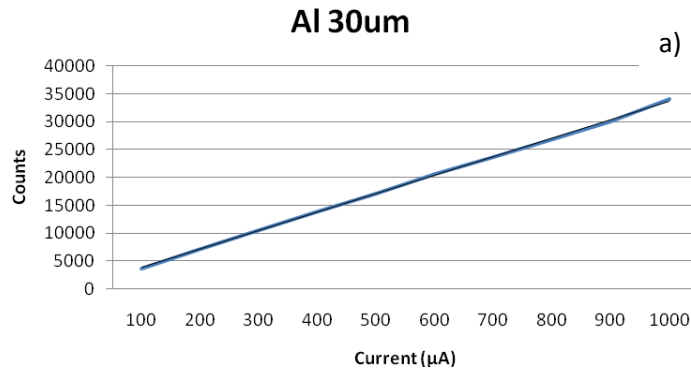


Beam size: 2-mm
 Amp. Time: 6,4 μ Sec
 Current: 100 μ A
 Live time: 10 Sec

Table Voltage experiment data for the 2-mm aperture
 Figure Voltage experiment data for the 2-mm aperture on the a) aluminum sample, b) copper sample, c) copper/aluminum alloy sample

Sheet 2.4: Current Experiment with 30- μm beam

Al			Cu			Al(Al+Cu)		Cu(Al+Cu)		
μA	Counts	Dtm%	μA	Counts	Dtm%	μA	Counts	Amp	Counts	Dtm%
100	3640	8	100	4000	16	100	3060	100	476	8
200	7231	13	200	7651	24	200	5998	200	887	14
300	10603	17	300	11104	32	300	8850	300	1276	19
400	13951	22	400	14243	39	400	11479	400	1712	23
500	17088	26	500	17110	44	500	14131	500	2097	27
600	20641	30	600	19499	48	600	16776	600	2378	31
700	23670	34	700	22293	53	700	19502	700	2770	34
800	26822	37	800	24313	56	800	22043	800	3038	37
900	30002	40	900	26216	59	900	24191	900	3389	40
1000	33997	44	1000	28475	63	1000	26691	1000	3636	43

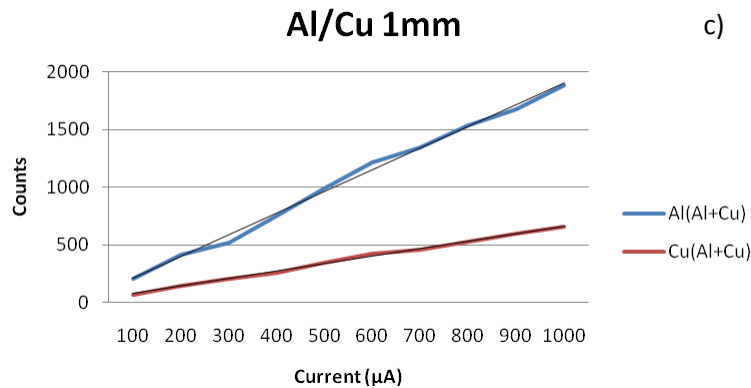
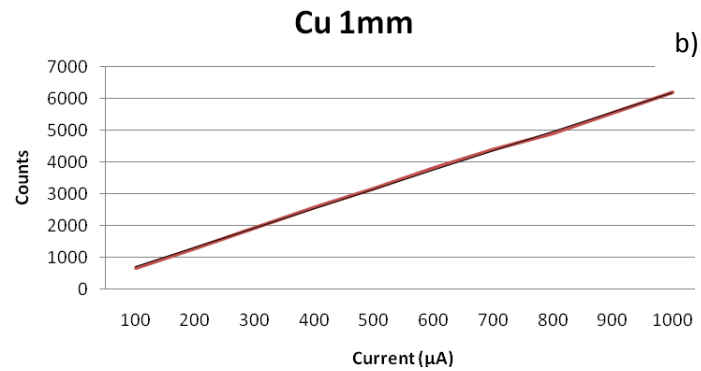
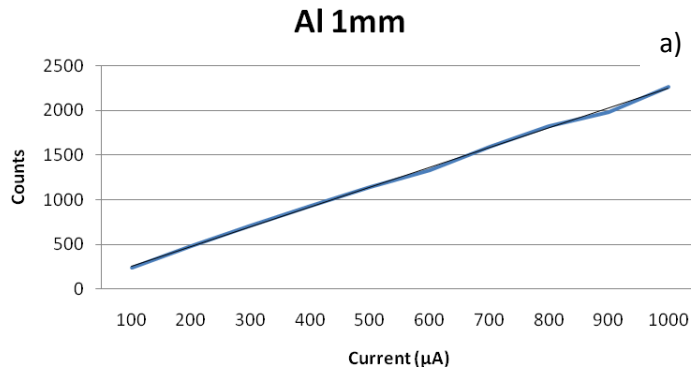


Beam size: 30- μm
 Amp. Time: 6,4 μSec
 Voltage: 20 keV
 Live time: 10 Sec

Table Current experiment data for the 30- μm polycapillary
 Figure Current experiment data for the 30- μm polycapillary on the a) aluminum sample, b) copper sample, c) copper/aluminum alloy sample, with trend line

Sheet 2.5: Current Experiment with 1-mm beam

Al			Cu			Al(Al+Cu)			Cu(Al+Cu)		
μA	Counts	Dtm%	μA	Counts	Dtm%	μA	Counts	Amp	Counts	Dtm%	
100	234	4	100	664	7	100	210	100	72	4	
200	480	4	200	1276	8	200	413	200	148	5	
300	712	5	300	1922	10	300	517	300	204	5	
400	928	5	400	2583	11	400	757	400	261	5	
500	1146	5	500	3162	13	500	989	500	346	6	
600	1330	5	600	3822	14	600	1219	600	427	7	
700	1590	6	700	4398	15	700	1345	700	457	7	
800	1829	6	800	4914	17	800	1539	800	527	8	
900	1979	6	900	5543	18	900	1677	900	600	8	
1000	2269	6	1000	6196	20	1000	1886	1000	656	8	

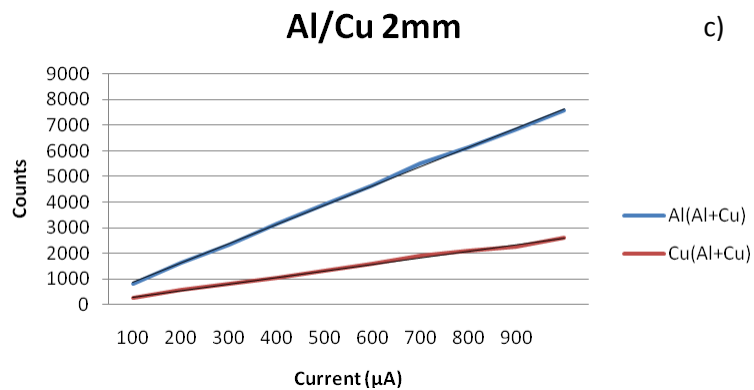
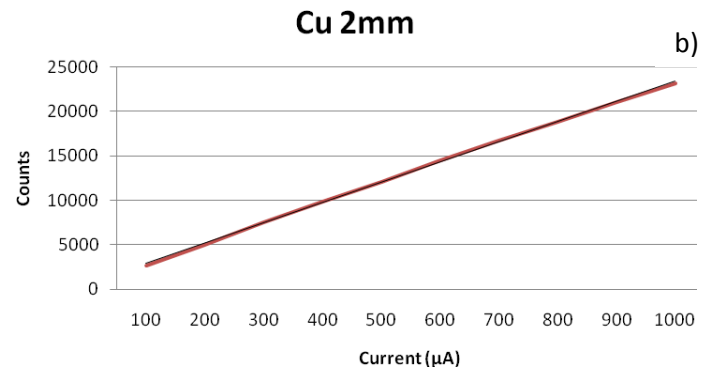
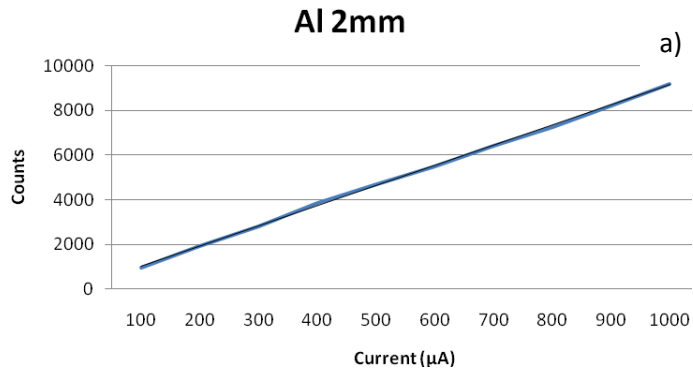


Beam size: 1-mm
 Amp. Time: 6,4 μSec
 Voltage: 20 keV
 Live time: 10 Sec

Table Current experiment data for the 1-mm aperture
 Figure Current experiment data for the 1-mm aperture on the a) aluminum sample, b) copper sample, c) copper/aluminum alloy sample, with trend line

Sheet 2.6: Current Experiment with 2-mm beam

Al			Cu			Al(Al+Cu)			Cu(Al+Cu)		
μA	Counts	Dtm%	μA	Counts	Dtm%	μA	Counts	Amp	Counts	Dtm%	
100	969	5	100	2688	12	100	807	100	285	5	
200	1919	6	200	4995	17	200	1641	200	562	7	
300	2807	6	300	7519	23	300	2346	300	801	10	
400	3849	9	400	9827	28	400	3165	400	1063	12	
500	4706	9	500	12039	33	500	3920	500	1331	14	
600	5492	11	600	14514	37	600	4635	600	1593	16	
700	6417	13	700	16680	41	700	5493	700	1897	17	
800	7263	13	800	18824	45	800	6145	800	2088	18	
900	8230	15	900	21026	49	900	6855	900	2263	21	
1000	9206	17	1000	23203	52	1000	7597	1000	2598	22	



Beam size: 2-mm
 Amp. Time: 6,4 μSec
 Voltage: 20 keV
 Live time: 10 Sec

Table Current experiment data for the 2-mm aperture
 Figure Current experiment data for the 2-mm aperture on the a) aluminum sample, b) copper sample, c) copper/aluminum alloy sample, with trend line

Chapter 3: Evaluation Test for Quantitative Analyses

3.1 Introduction

This chapter describes evaluation tests that were executed to determine the quality of element concentrations obtainable with a standardless routine of the Orbis μ -XRF (FP No Standards).

The main objective was to explore which parameter sets would provide small enough errors for quantitative analysis of geological samples. Special attention was paid to technical capabilities and limitations for measuring systematic compositional variations in samples that are heterogeneous on a small scale, such as finely laminated rocks. Specific questions to be answered included: are the μ -XRF quantitative results reproducible (do the data have small standard deviations), do preferred parameters vary for different standards and how would this influence the errors? Results from the use of low and high currents were compared, and possible improvements from the use of high voltages for standard measurements were tested. Finally it was examined whether applying 30 keV instead of 50 keV for creating a WAX reference spectrum would improve the results, and whether they would be influenced if amplifier times are different from that used for the WAX reference spectrum. All of these findings are documented for different geological standards in test tables that illustrate effects of voltage, current and amplifier time.

3.2 Methods

The parameter sets were tested on three international standards of known composition: basalt (JB-1b), granite (GS-N), and a Fe-rich rock (FER-4). These standards were selected because of their different compositions and geological significance. The FER-4 standard was included because of its particular relevance for the analysis of Banded Iron Formations and associated Fe-rich cherts.

The parameters that were allowed to vary are *Voltage*, *Current*, and *Amplifier Time*. The parameters that were kept constant are the Aperture (2-mm was taken to overcome possible small-scale inhomogeneity of standards), the Live Time (120 seconds which is long enough to produce good spectra), use of the FP No Standards routine, and absence of a filter.

Two main sets of tests were executed. The first set involved data collection with varying parameters (*Table 3.1*), the most important being the voltage that was allowed to cover a range from 20 to 50 keV with 10 keV steps. These spectra were taken against a 50 keV and 500 μ A WAX reference spectrum. In the second test set, the three rock

standards were measured at 20 and 30 keV against a WAX reference spectrum taken at 30 keV and 800 μA (*Table 3.2*). These voltages were chosen because they are probably the most applicable for geological samples, while the higher voltages of 40 and 50 keV were added to explore their potential benefits. Any of the voltages taken had to be coupled to an appropriate current. For these tests, a high and a low current were taken at each voltage: 100 μA for all of the low-current sets, and up to a maximum of 1000 μA for the high-current sets, the exact value depending on the requirement that the Dead time (Dtm%) did not exceed 30%. These specific high-current values are reported in *Table 3.1* and *Table 3.2*. This Dtm% limit of 30% is 10% lower than that adopted for the tests described in *Chapter 2*, but it was preferred here because developing experience had taught that the Dtm% should be around 20% and not exceed 30% for optimal conditions when working with a $\mu\text{-XRF}$ with a Silicon Drift Detector.

The selected amplifier times were 3.2 and 6.4 μs , because the previous tests had indicated that 6.4 μs produces the lowest peak widths, and thus the best resolution, whereas the WAX reference spectrum should be measured at 3.2 μs . By combining voltage and current settings in this way, insights could be obtained into possible effects of collecting spectra at a different amplifier time than that of the reference spectrum.

The collected spectra were processed or quantified by the software provided with the $\mu\text{-XRF}$. To avoid possible software problems it was made sure that, during the quantification routine, the $\mu\text{-XRF}$ was set at the voltage at which the spectra had been taken. The known H_2O and CO_2 concentrations were entered in the KENO option (Known Elements Not Observed) of the program, since these components could not be measured because the Be-window filters out every element with characteristic voltages below 1 keV. Only the H_2O^+ species was entered for water since the samples were heated at 100°C , so that any adsorbed water (H_2O^- , not present in the atomic structure) was removed. The quantification results of the six spectra per condition set were compared. In a few occasions, one of the spectra was discarded because of erroneous measurements.

Summary for the first set of tests:

- WAX reference spectrum collected at 50 keV and 500 μA
- Three rock standards: basalt, granite, and Fe-rock
- Voltages of 20, 30, 40, and 50 keV
- Fixed low current of 100 μA and variable high current depending on the Dtm% (*Table 3.1*)
- Amplifier times of 3.2 and 6.4 μs

Summary for the second set of tests:

- WAX reference spectrum collected at 30 keV and 800 μA
- Three rock standards: basalt, granite, and Fe-rock
- Voltages of 20 and 30 keV
- Fixed low current of 100 μA and variable high current depending on the Dtm%
(Table 3.2)
- Amplifier times of 3.2 and 6.4 μs

All tests were repeated 6 times for each combination of conditions. Processing of the spectra yielded quantitative data on element concentrations of interest.

Basalt	<i>Amp Time</i>	<i>Voltage</i>	<i>Current</i>	<i>Dtm%</i>		<i>Amp Time</i>	<i>Voltage</i>	<i>Current</i>	<i>Dtm%</i>
JB-1b	3.2 μs	20 keV	100 μA	2		6.4 μs	20 keV	100 μA	6
	3.2 μs	20 keV	1000 μA	10		6.4 μs	20 keV	1000 μA	22
	3.2 μs	30 keV	100 μA	2		6.4 μs	30 keV	100 μA	9
	3.2 μs	30 keV	1000 μA	16		6.4 μs	30 keV	600 μA	23
	3.2 μs	40 keV	100 μA	3		6.4 μs	40 keV	100 μA	10
	3.2 μs	40 keV	1000 μA	22		6.4 μs	40 keV	400 μA	23
	3.2 μs	50 keV	100 μA	4		6.4 μs	50 keV	100 μA	12
	3.2 μs	50 keV	1000 μA	28		6.4 μs	50 keV	400 μA	28
Granite	<i>Amp Time</i>	<i>Voltage</i>	<i>Current</i>	<i>Dtm%</i>		<i>Amp Time</i>	<i>Voltage</i>	<i>Current</i>	<i>Dtm%</i>
GS-N	3.2 μs	20 keV	100 μA	1		6.4 μs	20 keV	100 μA	4
	3.2 μs	20 keV	1000 μA	8		6.4 μs	20 keV	1000 μA	18
	3.2 μs	30 keV	100 μA	2		6.4 μs	30 keV	100 μA	8
	3.2 μs	30 keV	1000 μA	13		6.4 μs	30 keV	600 μA	19
	3.2 μs	40 keV	100 μA	3		6.4 μs	40 keV	100 μA	11
	3.2 μs	40 keV	1000 μA	19		6.4 μs	40 keV	400 μA	21
	3.2 μs	50 keV	100 μA	4		6.4 μs	50 keV	100 μA	14
	3.2 μs	50 keV	1000 μA	24		6.4 μs	50 keV	400 μA	25
Fe-rock	<i>Amp Time</i>	<i>Voltage</i>	<i>Current</i>	<i>Dtm%</i>		<i>Amp Time</i>	<i>Voltage</i>	<i>Current</i>	<i>Dtm%</i>
FER-4	3.2 μs	20 keV	100 μA	3		6.4 μs	20 keV	100 μA	8
	3.2 μs	20 keV	1000 μA	19		6.4 μs	20 keV	500 μA	22
	3.2 μs	30 keV	100 μA	4		6.4 μs	30 keV	100 μA	12
	3.2 μs	30 keV	700 μA	23		6.4 μs	30 keV	300 μA	23
	3.2 μs	40 keV	100 μA	6		6.4 μs	40 keV	100 μA	15
	3.2 μs	40 keV	500 μA	23		6.4 μs	40 keV	200 μA	23
	3.2 μs	50 keV	100 μA	7		6.4 μs	50 keV	100 μA	18
	3.2 μs	50 keV	500 μA	28		6.4 μs	50 keV	200 μA	27

Table 3.1 Selected Amplifier times, Voltages, Currents and Dtm% values in parameter tests for measurements on three international standards against the 50 keV and 500 μA WAX reference spectrum.

Basalt	<i>Amp Time</i>	<i>Voltage</i>	<i>Current</i>	<i>Dtm%</i>		<i>Amp Time</i>	<i>Voltage</i>	<i>Current</i>	<i>Dtm%</i>
JB-1b	3.2 μ s	20 keV	100 μ A	2		6.4 μ s	20 keV	100 μ A	6
	3.2 μ s	20 keV	1000 μ A	10		6.4 μ s	20 keV	1000 μ A	22
	3.2 μ s	30 keV	100 μ A	3		6.4 μ s	30 keV	100 μ A	9
	3.2 μ s	30 keV	1000 μ A	17		6.4 μ s	30 keV	800 μ A	28
Granite	<i>Amp Time</i>	<i>Voltage</i>	<i>Current</i>	<i>Dtm%</i>		<i>Amp Time</i>	<i>Voltage</i>	<i>Current</i>	<i>Dtm%</i>
GS-N	3.2 μ s	20 keV	100 μ A	1		6.4 μ s	20 keV	100 μ A	6
	3.2 μ s	20 keV	1000 μ A	8		6.4 μ s	20 keV	1000 μ A	18
	3.2 μ s	30 keV	100 μ A	2		6.4 μ s	30 keV	100 μ A	8
	3.2 μ s	30 keV	1000 μ A	13		6.4 μ s	30 keV	1000 μ A	28
Fe-rock	<i>Amp Time</i>	<i>Voltage</i>	<i>Current</i>	<i>Dtm%</i>		<i>Amp Time</i>	<i>Voltage</i>	<i>Current</i>	<i>Dtm%</i>
FER-4	3.2 μ s	20 keV	100 μ A	2		6.4 μ s	20 keV	100 μ A	8
	3.2 μ s	20 keV	1000 μ A	18		6.4 μ s	20 keV	700 μ A	27
	3.2 μ s	30 keV	100 μ A	4		6.4 μ s	30 keV	100 μ A	11
	3.2 μ s	30 keV	900 μ A	28		6.4 μ s	30 keV	400 μ A	28

Table 3.2 Selected Amplifier times, Voltages, Currents and Dtm% values in parameter tests for measurements on three international standards against the 30 keV and 800 μ A WAX reference spectrum.

3.3 Results and Discussion

3.3.1 Precision

The standard deviation and precision results can be found in *Appendix 1*. Although concentrations for sodium are reported in *Appendices 1 and 2*, this element was excluded from the assessments because its characteristic peak in the spectrum is too close to the Be-filter cut-off of 1 keV, and sits on the tails of Si, Al, and Mg peaks, which makes results unreliable. The software did not always recognize the background of these four elements correctly, specifically if they are present in low amounts, as could be the case for all of the three geological standards used. The resulting large errors and standard deviations are thus not very meaningful.

As expected, the elements with low concentrations of <1 wt% in the rock standards also show relatively large standard deviations (*Table 3.3*). An exception is Ti in the granite standard, which shows a good precision despite its low concentration. Standard deviations for elements present in larger amounts are generally better than ~5%. Because in the FER-4 standard, the concentrations of elements other than Fe and Si do not exceed 2.3 wt%, their standard deviations are not reported.

From the low standard deviations, and thus high precisions found it can be concluded that the μ -XRF instrument yielded well reproducible concentration data for most of the major and minor elements investigated, independent from the moment of data collection. The exact precision of the instrument obviously depends on the concentration of the element of interest.

	Basalt (JB-1b)		Granite (GS-N)		Fe-rock (FER-4)	
	Wt%	Precision	Wt%	Precision	Wt%	Precision
SiO_2	51.11	good	65.8	good	50.07	good
TiO_2	1.26	good	0.68	good	0.07	X
Al_2O_3	14.38	good	14.67	good	1.70	X
MnO	0.147	poor	0.06	poor	0.19	X
MgO	8.14	good	2.3	poor	1.41	X
CaO	9.6	good	2.5	good	2.23	X
K_2O	1.32	good	4.63	good	0.29	X
P_2O_5	0.256	poor	0.28	poor	0.13	X
Fe_2O_3 TOTAL	9.06	good	3.75	good	39.92	good

Table 3.3 Compositions of the three geological standards, and precision assessments obtained for each oxide. Na_2O was excluded (see text). 'Good' represents standard deviations below ~5%, and 'poor' represents standard deviations generally higher than ~5% and with irregular behavior when results for the five different voltages are compared (see graphs in *Appendix 1*). The precisions were determined per element and standard by combining the results from the entire range of parameter sets. The complete data set and graphs are given in *Appendix 1*.

The comparison of results from the sets when 30 keV or 50 keV WAX reference spectra were used is inconclusive for the basalt and granite standards. In some cases, depending on the element or conditions, the 50 keV WAX resulted in a better precision, while in other cases the 30 keV WAX was more precise. Any differences are, however, not more than a few percent. Differences between the standard-deviation results from the two WAX reference spectra were slightly larger for the Fe-rock than for the basalt and granite, but any contrasts are still minor. Hence, the use of the 50 keV WAX reference spectrum would be preferable because it would allow operating at higher voltages without having to change the reference setting.

Even if results from the 30 keV WAX reference spectrum are ignored, no obvious relationships were found between standard deviations, specific elements, voltages, and amplifier times. However, at increasing currents, the standard deviations do appear to reduce, independent from other parameters.

For the basalt and granite data, the standard deviations found at 40 keV deviate from those obtained at the other voltages. For the Fe-rock data, only the standard deviations for data collected at 30 and 50 keV against the 50 keV WAX reference spectrum diverge. These findings mainly apply to the minor elements. For Si and Al in the basalt and granite the differences in standard deviations were only up to 1%.

3.3.2 Accuracy

Appendix 2 documents the accuracy results for the measured geological standards. The accuracy data for the basalt and granite, obtained with the 30 keV and 50 keV WAX

reference spectra, are comparable, but those for the Fe-rock show large deviations. The differences with accepted values lie within a few percent for the basalt and granite, while they are about 10% for Si and Fe in the Fe-rock. The accuracies for the other elements in the Fe-rock are not very meaningful due to the low concentrations. The results for these elements are reported, as are the results for Na in the basalt and granite, but they are excluded from further evaluation. For the Fe-rock, the 50 keV WAX reference spectrum produced better accuracies for Si, while the 30 keV WAX reference spectrum produced better results for Fe.

The lack of good accuracies (i.e., errors <5%) is not limited to elements that are present in low concentrations (<5 wt%) but also applies to elements with moderately high concentrations (5-10 wt%) and occasionally to elements with high abundances (>10 wt%) (Table 3.3). For the basalt, the relatively abundant elements Mg, Ca, and Fe show large errors varying between about 10 and 50 percent. The accuracies for highly abundant elements are generally better than for the minor elements, showing maximum values of ~12.5% for Si and Al in the basalt and granite standards, and ~22% for Si and Fe in the Fe-rock standard (see Table 3.4).

	Accuracy for Si		Accuracy for Al		Accuracy for Fe	
	Maximum	Minimum	Maximum	Minimum	Maximum	Minimum
<i>Basalt</i>	12.5 %	2.4 %	9.2 %	0.2 %	X	X
<i>Conditions</i>	50 keV WAX, 50 keV, 100 μA, 6.4 μs	50 keV WAX, 20 keV, high μA, 3.2 μs	50 keV WAX, 50 keV, 100 μA, 3.2 μs	30 keV WAX, 20 keV, 100 μA, 6.4 μs		
<i>Granite</i>	9.2 %	1.0 %	11.5 %	4.5 %	X	X
<i>Conditions</i>	50 keV WAX, 50 keV, 100 μA, 6.4 μs	50 keV WAX, 20 keV, high μA, 3.2 μs	50 keV WAX, 50 keV, 100 μA, 3.2 μs	30 keV WAX, 20 keV, high μA, 6.4 μs		
<i>Fe-rock</i>	14.0 %	1.5%	X	X	22.0 %	0.5 %
<i>Conditions</i>	50 keV WAX, 50 keV, 100 μA, 6.4 μs	50 keV WAX, 30 keV, high μA, 3.2 μs			50 keV WAX, 20 keV, high μA, 6.4 μs	30 keV WAX, 30 keV, 100 μA, 3.2 μs

Table 3.4 Maximum and minimum accuracy values for elements with concentrations of more than 10 wt%, and the adopted conditions.

Lowering the *voltage* improved the accuracies for Si, Al, and Fe in the basalt and the granite, and thus had a positive effect. It resulted in a better accuracy for Si but a poorer accuracy for Fe in the Fe-rock. The other elements did not show any effects from voltage changes.

Increasing the *current* resulted in better accuracies for the minor element Ti in all cases and for K in the basalt and granite standards. At almost all voltages and amplifier times

the higher current yielded a better accuracy than the lower current. Only at 6.4 μs , no real differences were seen in the basalt test, while in the Fe-rock tests accuracies improved only slightly at the higher current than at the low current.

No significant improvement was observed when the *amplifier time* for sample measurement was equal to that for collecting the WAX reference spectrum compared to when amplifier times were different. An amplifier time of 6.4 μs is preferred over 3.2 μs for geological samples, because it yielded the highest peak resolution (see *Chapter 2*).

3.4 Conclusions

In conclusion, good precisions (standard deviations <5%) were obtained for most of the elements present in the three rock standards. For Mn and P, minor elements with concentrations below 1 wt%, the results were not satisfactory. Thus, according to the executed tests the $\mu\text{-XRF}$ instrument should provide reproducible data for most major and minor elements in geological samples.

The precision of results was virtually independent from the use of 30 keV or 50 keV WAX reference spectra. The 50 keV WAX reference spectrum created better accuracies for elements in the basalt and granite standards, and for Si in the Fe-rock standard, whereas the 30 keV WAX reference spectrum provided better results for Fe in the Fe-rock standard. The use of the 50 keV WAX reference spectrum is generally advisable, also because no change in reference spectra would be necessary when measurements are done at relatively high voltages.

The accuracy results improved with decreasing voltage for Si, Al, Fe, and Ti measured in the basalt and granite standards. The same holds for Si in the Fe-rock standard, but a reverse effect was observed for Fe. In contrast, measurements of K and Ti in basalt and granite, and Fe and Ti in the Fe-rich standard benefited from the use of higher rather than lower voltages. However, because the 40 keV produced outlying standard deviations for many elements in the basalt and granite standards, it is not advised to use such a high voltage.

Higher currents have better effects on the accuracy and precision of the data than higher voltages.

Choosing the same amplifier time as that for the WAX reference spectrum did not result in a significant improvement compared to a deviating amplifier times. An amplifier time of 6.4 μs (see *Chapter 2*) remains is the best option for geological samples.

Many of the analytical problems can probably be attributed to the FP No Standards routine. So far, this seems only capable of accurately quantifying elements with

concentrations >10 wt%. The best and most accurate results with errors below 0.5% were collected with a 2-mm aperture, an amplifier time of 6.4 μ s, and a high current (depending on the allowed Dtm%). For the basalt and granite samples a low voltage of 20-30 keV was necessary to obtain reliable results for Si and Al, as was the case for Si results in the Fe-rich sample, whereas a high voltage of 40-50 keV was required for Fe in the latter.

Chapter 4: Analysis of Archaean chert samples from the Pilbara craton, Australia

4.1 Introduction

The aim of this part of the investigation was to test the capabilities of the μ -XRF technique by analyzing Archaean cherts from Marble Bar (C-chert, sample 1) and Kitty's Gap (S-chert, sample 2) in the Pilbara craton, Australia (*Figure 4.1*). The question was examined for which elements reliable qualitative and quantitative data could be obtained. The two rock samples were selected because they had been extensively analyzed before by MC-ICP-MS (Multi Collector-Inductively Coupled Plasma Mass Spectrometry) as part of a silicon-isotope study (Van den Boorn, 2008). The samples represent different styles of chert formation. The Marble Bar sample is a typical C-chert that formed as chemical precipitate from seawater and/or hydrothermal water that was saturated in silica. The Kitty's Gap sample represents a volcanoclastic sediment that was silicified by percolating seawater. Both cherts underwent only low degrees of metamorphism, their metamorphic grades being greenschist facies or lower (Van Kranendonk et al., 2003; Van der Boorn, 2008).

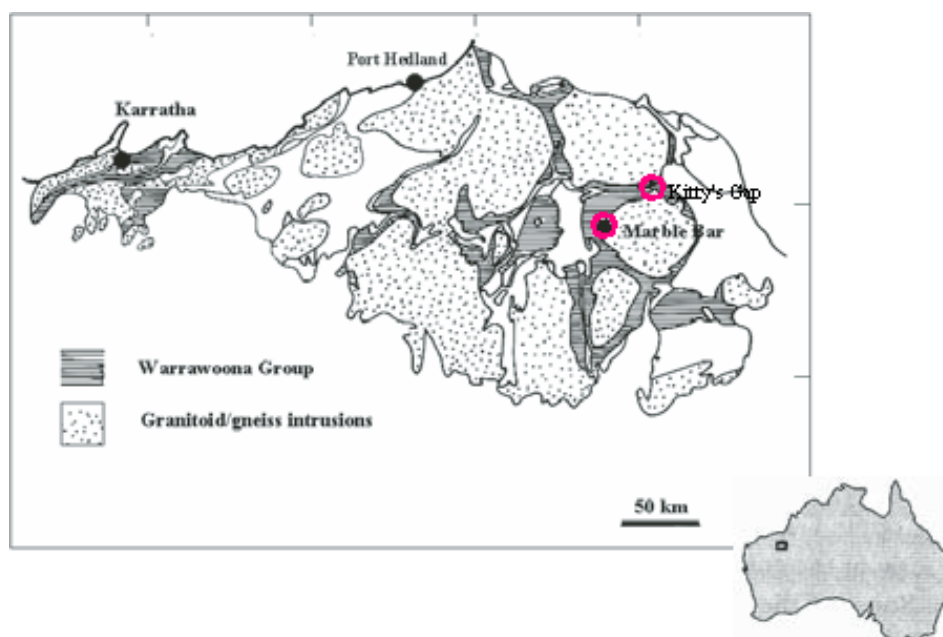


Figure 4.1 Map of the Pilbara region in Australia with approximate locations of Marble Bar and Kitty's Gap (After: Westall et al., 2006)

Each of the chert samples shows fine laminations varying in thickness between one millimeter and several centimeters. Color differences between the laminae are a first indication of variable chemical compositions. Relatively dark and red layers in the C-chert were thought to be Fe-rich, and whitish layers Fe-poor and Si-rich. Laminae in the S-chert show less conspicuous color variations in white and grey. It was anticipated that these variations would reflect different concentrations of sericite. According to earlier

work the compositional differences between laminae indicate changes in depositional conditions or variations in the composition of precursor sediments (e.g. Kato and Nakamura, 2003; Van den Boorn, 2008). For example, laminations in the C-cherts could have been caused by changes in hydrothermal activity (Van den Boorn, 2008).

Since the color variations in the test samples suggest that individual layers have different chemical compositions, it was attempted to determine these compositions in a number of layers. In addition, it was explored if mineralogical information could be obtained.

4.2 Methods

4.2.1 Sample 1 (C-chert): Red, Pink, White and Black layers

4.2.1.1 Qualitative

Spectra were collected for visually different layers in this orthochemical chert to determine which elements were most abundant and would thus be suitable to create linescans and element maps. These elements were Al, Ca, Fe, K, Mg, Mn, S, Si, and Ti. The linescans were labeled L1-L5, linescans through veins V1-V5, and the maps M1 and M2 (*Figure 4.2*). The overlap between individual spots in the linescans was taken to be approximately 20%, depending on the length of the line. For intra-layer linescans the total number of measured spots was 256. Overlap percentages of spots in the maps varied due to the limitation of preset amounts of pixels (256x200 was mostly used) and the size of the defined mapping area. All analyses were performed under vacuum. Parameter settings are given in *Table 4.1*. No filters were used.

	<i>Voltage</i>	<i>Current</i>	<i>Amplifier time</i>	<i>Spot size</i>	<i>Live Time</i>
<i>Linescans L1</i>	20 keV	500 μ A	6.4 μ s	30 μ m	30 s
<i>Linescans</i>	20 keV	500 μ A	6.4 μ s	30 μ m	10 s
<i>Vein Linescans</i>	20 keV	500 μ A	6.4 μ s	30 μ m	10 s
<i>Maps</i>	20 keV	500 μ A	6.4 μ s	30 μ m	1 s

Table 4.1 Parameters for the analyses performed on both Achaean chert samples

4.2.1.2 Quantitative

Quantitative data were collected for various different layers. All except one of the red layers, one black layer, two pink layers, two regular white layers and one apparently microcrystalline white layer were analyzed. In each individual layer spectra were collected in such a way that interference with other layers and veins was avoided as much as possible. The average of six spectra was taken to represent the composition of a specific layer. In addition, linescan measurements across all five red layers were quantified in order to further explore stratigraphic changes in Fe-Mn relationships seen in the qualitative tests. The elements considered were the same as those taken for the

qualitative analyses with the exception that S was replaced by P. The quantification was executed with the Orbis Vision software against a 50-keV WAX reference spectrum, using the standard-less routine (FP No Standards) without KENO values (Known Elements Not Observed). The analyses were carried out at 40 keV and 200 μ A, using a 2-mm aperture, an amplifier time of 6.4 μ s, and no filters. These settings were chosen based on the findings outlined in Chapter 3. The voltage 40 keV was preferred because it yields similar errors for Si and Fe (\sim 10%, see *Table 4.2*), and hence would be most appropriate for Fe-rich chert samples. *Table 4.2* includes errors for Mn because this element shows relationships with Fe that will be discussed later in this chapter.

4.2.2 Sample 2 (S-chert): White and various Grey layers

4.2.2.1 Qualitative

Test spectra taken on this silicified precursor chert (S-chert) identified Si as most abundant element. Hence, the same group of elements was investigated as in sample 1. The linescans are labeled L1-L6, and the maps M1 and M2. Positions and labels can be found in *Figure 4.3*. Spot overlaps were the same as given above for sample 1. This sample was also analyzed under vacuum, with parameter settings reported in *Table 4.1*. No filters were used.

	30keV error	20keV error	50keV error	40keV error	30keV error	20keV error
SiO ₂ %	12.2 %	5.7 %	12.7 %	9.9 %	4.5 %	-2.0 %
Fe ₂ O ₃ t %	4.0 %	10.2 %	9.0 %	11.0 %	15.6 %	22.0 %
MnO %	-14.0 %	-14.0 %	-4.4 %	-5.3 %	-6.1 %	-2.6 %
WAX Ref. Spectrum	30 keV	30 keV	50 keV	50 keV	50 keV	50 keV

Table 4.2 Errors obtained on the Fe-rock standard for 6.4 μ s and high currents. Fe₂O₃ t: All Fe taken as Fe₂O₃.

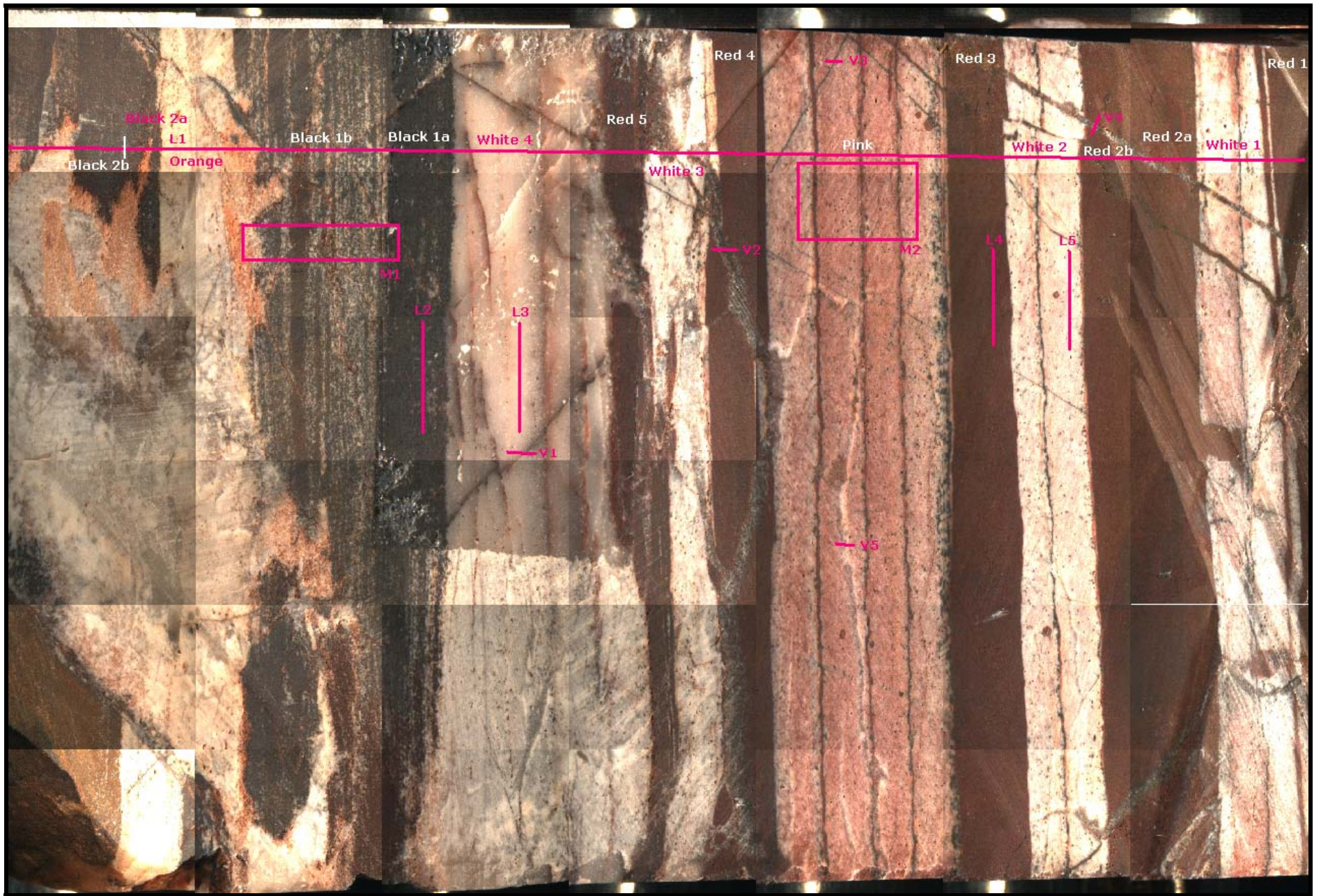


Figure 4.2 General overview of sample 1 (C-chert) with positions and approximate lengths of the linescans, vein linescans and maps made. Approximate size of the image 9.5x5 cm. L = Linescan, V = Vein linescan, M = Map. The layers are labeled by color and number.

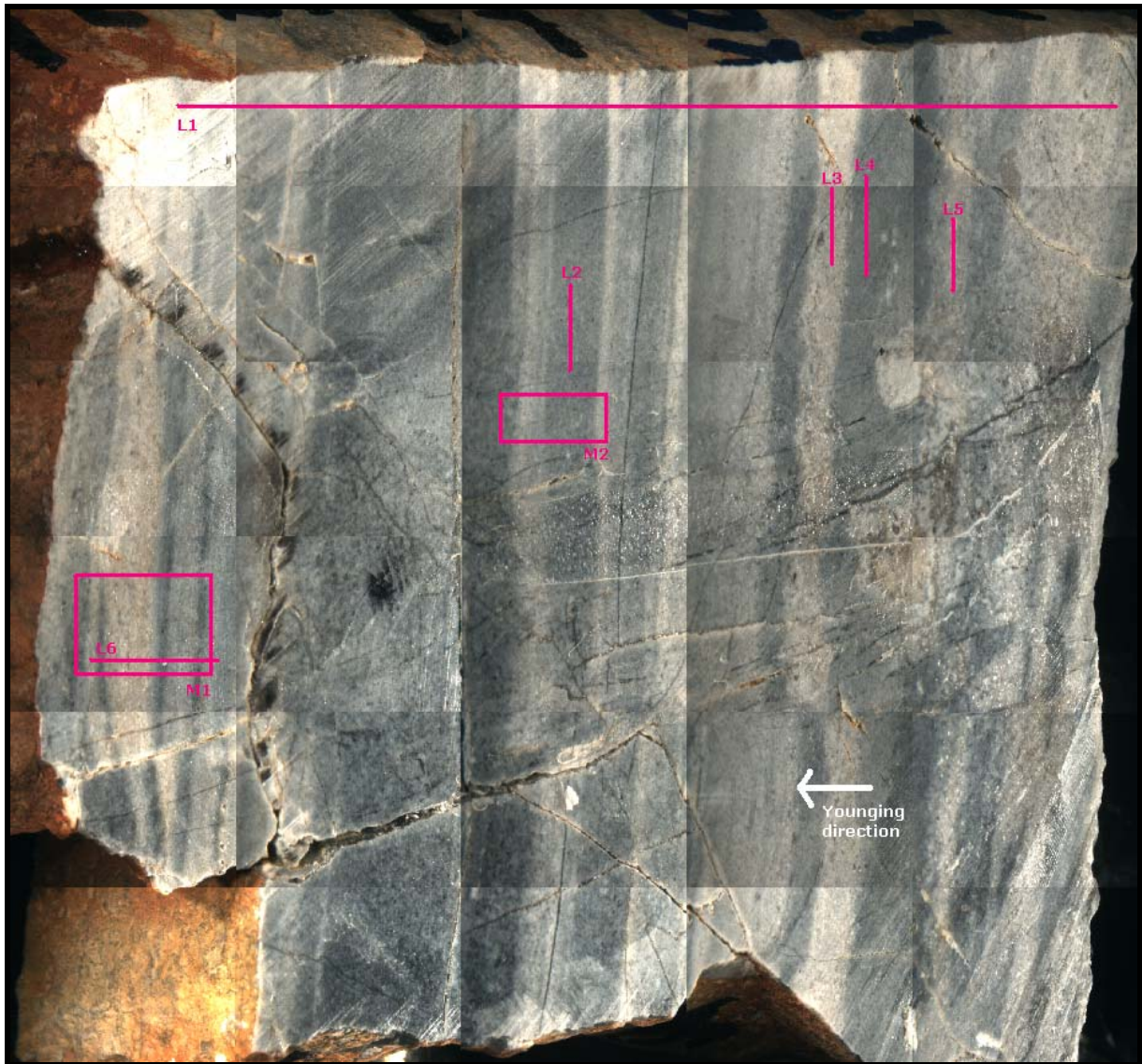


Figure 4.3 General overview of sample 2 (S-chert) with positions and approximate lengths of the linescans and maps made. Approximate size of the sample is 7x5 cm. L = Linescan, M = Map.

4.3 Results

4.3.1 Sample 1 (C-chert): Red, Pink, White and Black layers

4.3.1.1 Laminations

Figure 4.4 shows qualitative linescan trends for selected elements overlain on microphotographs of the color layers. The following observations can be made: (1) Si and Fe are the main constituents, (2) Mn peaks correlate with Fe in the Fe-rich layers, and (3) K and Al peaks are present whereby the latter correlate with dips in Si. Elements not shown did not produce any systematic pattern. The quantitative analyses confirmed that Si and Fe are the most abundant elements in this sample. The concentrations of SiO_2 and $\text{Fe}_2\text{O}_3^{\text{tot}}$ in the dark colored layers are around 60% and 30%, and in the light layers in the high eighties and close to zero, respectively (Table 4.3; see Appendix 3 for the complete data set). Note that the qualitative data showed higher count rates for Fe

than for Si (*Figure 4.4*), while the quantitative data indicated that Si was actually more abundant. No quantitative results could be obtained for areas yielding the high K and Al peaks seen in *Figure 4.4*.

	SiO_2	\pm	Fe_2O_{3total}	\pm	MnO	\pm
Red 2	63.3	6.3	28.8	3.2	0.15	0.01
Red 3	55.1	5.5	36.7	4.0	0.14	0.01
Red 4	60.1	6.0	32.2	3.5	0.07	0.00
Red 5	66.1	6.6	25.0	2.7	0.04	0.00
Black 1a	57.5	5.7	34.2	3.8	0.08	0.00
Pink 2	88.1	8.8	2.6	0.29	0.01	0.00
Pink 4	87.6	8.7	3.3	0.36	0.01	0.00
White 2	88.1	8.8	2.3	0.25	0.01	0.00
White 3	89.1	8.9	0.97	0.11	0.00	0.00
White 4	89.6	8.9	0.37	0.04	0.00	0.00

Table 4.3 Compositions (in wt%) of layers in the Marble Bar chert. Errors were calculated with the absolute error values determined in *Chapter 3* (see *Table 4.2*). White 4 is a microcrystalline layer.

The maps (*Figures 4.5 and 4.6*) confirm that the color layering in this sample is consistent with chemical variations. *Figure 4.6* shows that the pink layers are regularly spaced and of similar thickness, and that, against expectations, they do not contain large amounts of Fe but are relatively Si-rich. Thin layers between the pink layers are enriched in Fe but also appeared to contain some Ti (not shown) and Mn. Quantitative results (*Table 4.3*) indicate that the pink layers contain even less Fe (~ 3 wt% Fe_2O_3) than predicted from the qualitative scans.

From qualitative multi-element overlays created by the Orbis software (*Figure 4.7*), it was inferred that the main mineral phases in this sample are quartz and several iron oxides or iron carbonates that contain Mn (*Table 4.5*).

Figures 4.8 and 4.9 are binary variation diagrams for the Si-rich (white, pink and orange) and the Fe-rich (red and black) layers, respectively. The Fe-Si diagrams for the Si-rich group suggest the presence of two Fe phases, one being more dominant in the orange layer. In the corresponding Fe-Mn diagrams, two data clouds with different densities can be seen. The Fe-Si diagrams for the Fe-rich layers show patterns consistent with the presence of Si and Fe-rich phases as main components. The Fe-Mn diagrams for the Fe-rich group shows a clear distinction between the red and black layers with some overlap. This relationship was further examined by defining each red and black layer individually in diagrams where all the layers were color-coded (*Figure 4.10a and c*). These Fe-Mn diagrams for the red layers show a fan-shape pattern. This implies variations in Fe/Mn ratios in the layers that, except for the red-1 layer (purple in the

graph), follow a systematic stratigraphic order. In the black layers this fan is less pronounced but can still be noted. Quantitative data for the red layers confirmed these Fe-Mn relationships (*Figure 4.10b*). Note that the Fe-Mn graphs tend to show a curvature for each individual red and black layer, which becomes less strong at higher Fe and Mn contents.

Summaries of results for each different color layer can be found in *Table 4.4*.

Red layers	Black layers	Pink layers	Orange layers	White layers
<ul style="list-style-type: none"> • ~60 wt% Si • ~30 wt% Fe • ~0.1 wt% Mn • Distinct Fe-Mn-stratigraphy relation that make a fan (except for layer Red1) 	<ul style="list-style-type: none"> • ~57 wt% Si • ~34 wt% Fe • ~0.08 wt% Mn (data only from 1 black layer) • Different Fe-Mn phases in each layer but these show no distinct relation with the stratigraphy 	<ul style="list-style-type: none"> • ~88 wt% Si • ~3 wt% Fe • ~0.01 wt% Mn • Regularly spaced • Similar thickness 	<ul style="list-style-type: none"> • Low Mn • Generally low Fe, but some higher values are seen • 2 Fe phases present where one is more abundant 	<ul style="list-style-type: none"> • ~89 wt% Si • ~1 wt% Fe • ~0 wt% Mn • 2 Fe phases present

Table 4.4 Summary of layer characteristics.

4.3.1.2 Veins

The qualitative linescans across veins (*Figure 4.12*) show that the veins are either Si and Fe-rich or only Si-rich. However, not all visible veins could be chemically distinguished from their host, as compositions are sometimes almost equal (*Figure 4.12c*). The linescans through Si-rich veins (*Figure 4.12b*) show that Al follows the Si trend. The linescans further display variable highs and lows for most elements. Although relative amounts are sometimes difficult to assess, it is clear that Si and Fe are most abundant, whereas the other elements (Mg, Al, S, K, Ca, Ti, and Mn) are present in minor amounts only.

4.3.2 Sample 2 (S-chert): White and various Grey layers

Figure 4.13 shows qualitative linescan trends for selected elements overlain on microphotographs of the color layers. A clear difference with the C-chert sample is that the dominant elements are Si, Al and K rather than Si and Fe. Also, Al and K usually correlate, which is particularly obvious in white layers, although exceptions exist as well. Both elements show anti-correlations with Si. Element maps (*Figure 4.15*) and a K-Al diagram (*Figure 4.18*) confirm these observations.

In intra-layer linescans the Mg, Fe and Si trends tend to be similar those of Al and K (*Figure 4.14*). From Fe trends and from multi-element overlays (*Figures 4.16 and 4.17*) where high Fe also coincides with high Al and K, it can be inferred that this sample is

composed of quartz and Fe-bearing sericite as two main minerals (*Table 4.5*). The few Ti peaks seen in *Figures 4.13* and *4.17* suggest the presence of minor amounts of rutile.

As expected, the presence of sericite is restricted to sample 2. Its absence in sample 1 was confirmed in intra-layer element overlays (not shown) and a sericite (Al-K) reference line constructed from sericite-rich spots in sample 2 (*Figure 4.11*).

Ankerite	$\text{Ca}(\text{Mg,Fe,Mn})(\text{CO}_3)_2$		
Chlorite	$(\text{Mg,Fe,Al})_6(\text{Si,Al})(\text{OH})_8$		
Dolomite	$\text{CaMg}(\text{CO}_3)_2$		
Goethite	$\text{FeO}(\text{OH})$	May contain Mn	Possibly present in sample 1
Hematite	Fe_2O_3	May contain Mn	Possibly present in sample 1
Illite	$(\text{K,H}_3\text{O})(\text{Al,Mg,Fe})_2(\text{Si,Al})_4\text{O}_{10}[(\text{OH})_2,\text{H}_2\text{O}]$		
Kaolinite	$\text{Al}_4(\text{Si}_4\text{O}_{10})(\text{OH})_8$		
Magnetite	Fe_3O_4	May contain Mn	Possibly present in sample 1
Quartz	SiO_2		Present in sample 1 and 2
Rutile	TiO_2		Present in sample 2
Sericite	$\text{K}(\text{Al,Fe,Mg})_2(\text{Si,Al})_4\text{O}_{10}(\text{OH})_2 \cdot n\text{H}_2\text{O}$		Present in sample 2
Siderite	FeCO_3	May contain Mn	Possibly present in sample 1

Table 4.5 Minerals that can be present in Archaean cherts and BIFs (Kato and Nakamura, 2003; Floor, 2004; van Bergen, pers. comm. 2010). 'Possibly present' means that qualitative μ -XRF spectrometry could not unequivocally identify the mineral, mainly due to limitations in the measurement of O and C.

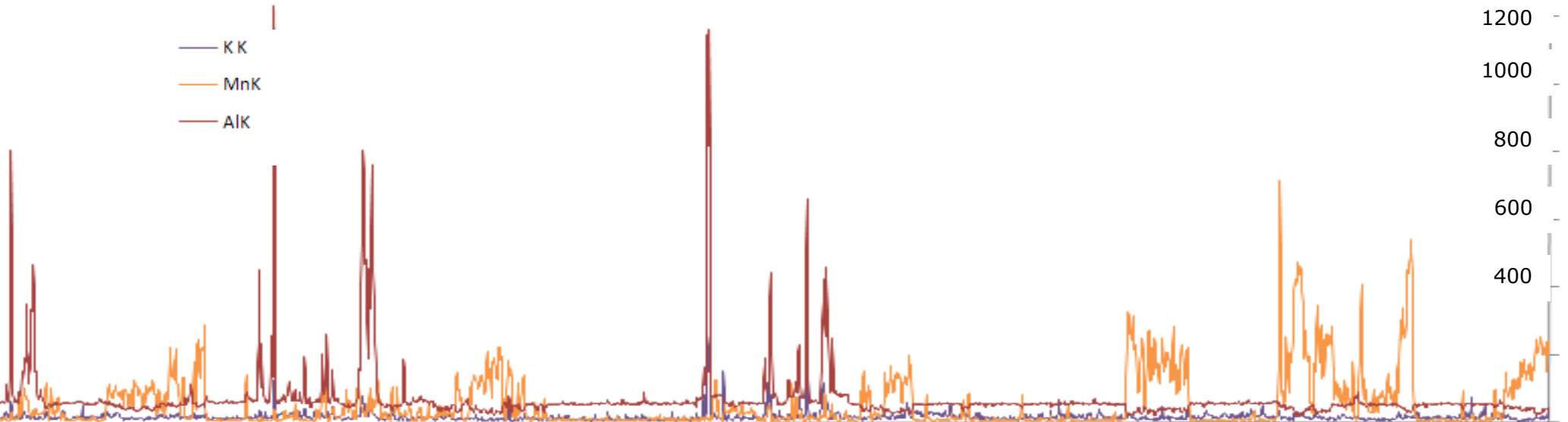
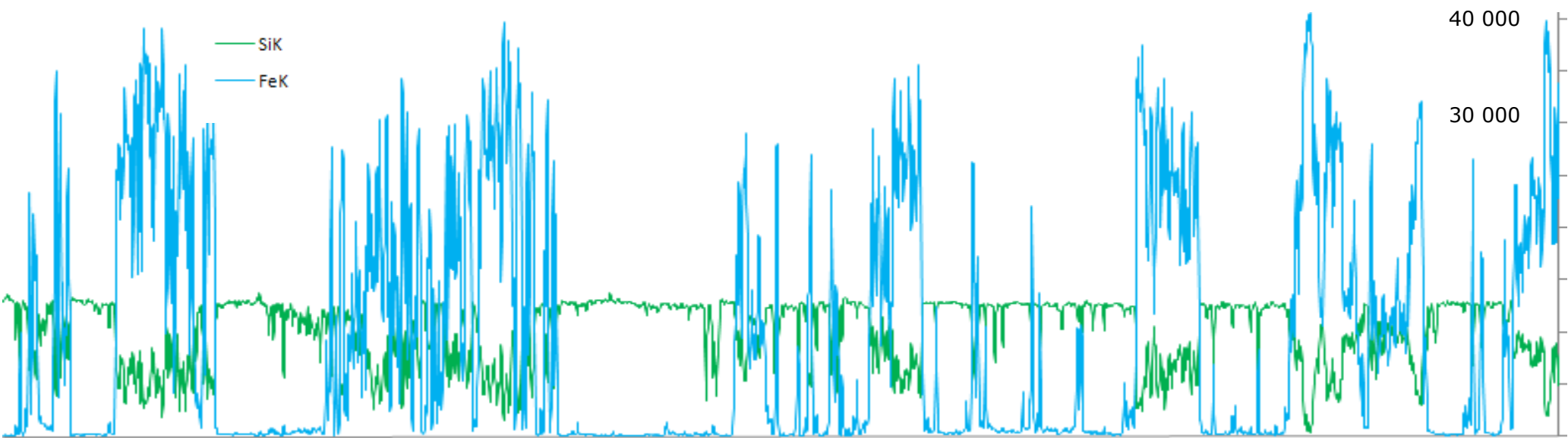


Figure 4.4 Major and minor element linescan 1 (K-lines) in sample 1. Length is ~9.5 cm.

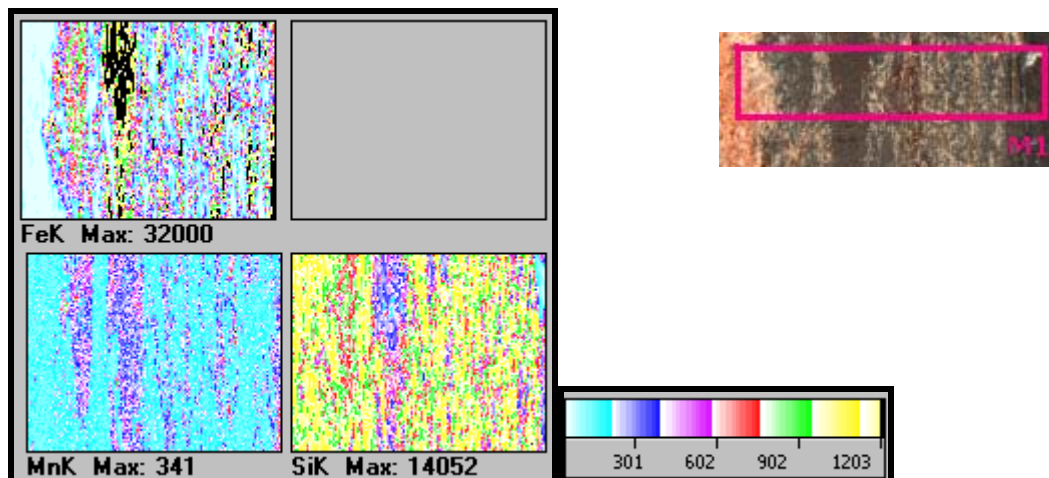


Figure 4.5 Element maps in sample 1 (M1). The color scheme (scale on the right) was adapted to improve the concentration contrasts. Note that the 4:5 dimensions of the shape here deviate from the actual measured M1 surface. The approximate size of the map is 1.3 x 0.3 cm.

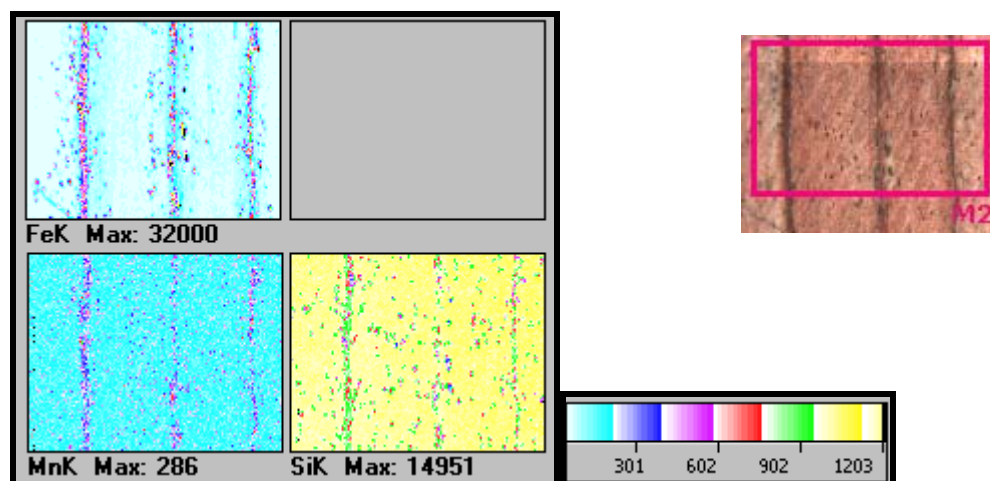


Figure 4.6 Element maps in sample 1 (M2). The color scheme (scale on the right) was adapted to improve the concentration contrasts. Note that the 4:5 dimensions of the shape here deviate from the actual measured M1 surface. The approximate size of the map is 0.9 x 0.5 cm.

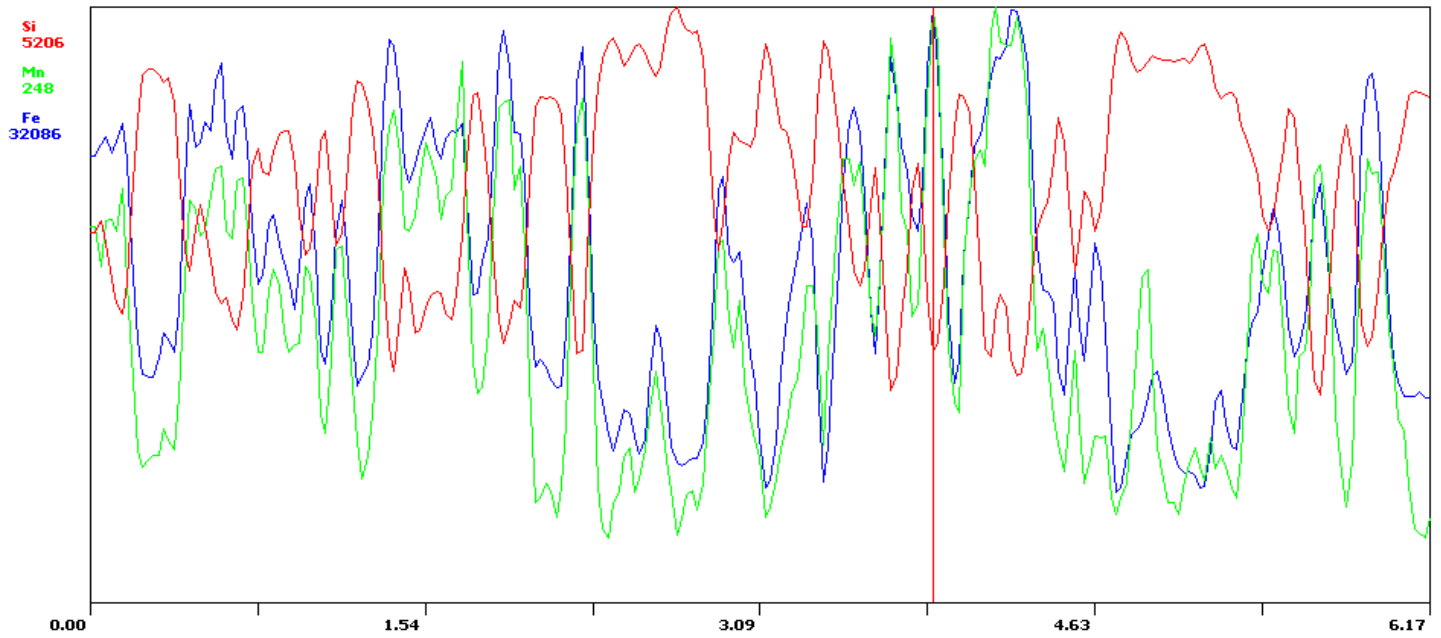


Figure 4.7 Element overlays (sample 1), illustrating the presence of quartz and Fe-oxide (or Fe-carbonate) minerals that contain some Mn.

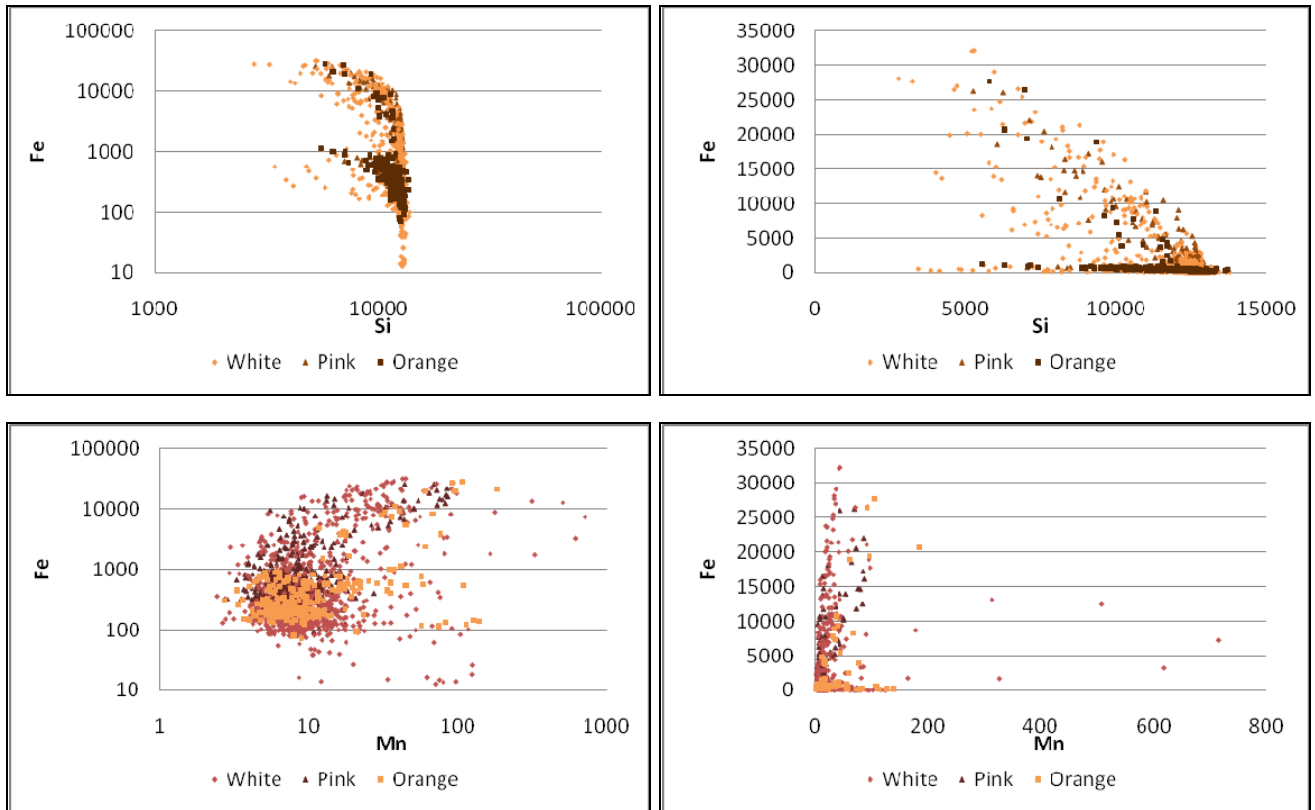


Figure 4.8 Si-Fe and Mn-Fe diagrams for the white, pink and orange Si-rich layers in sample 1 (logarithmic and normal scale).

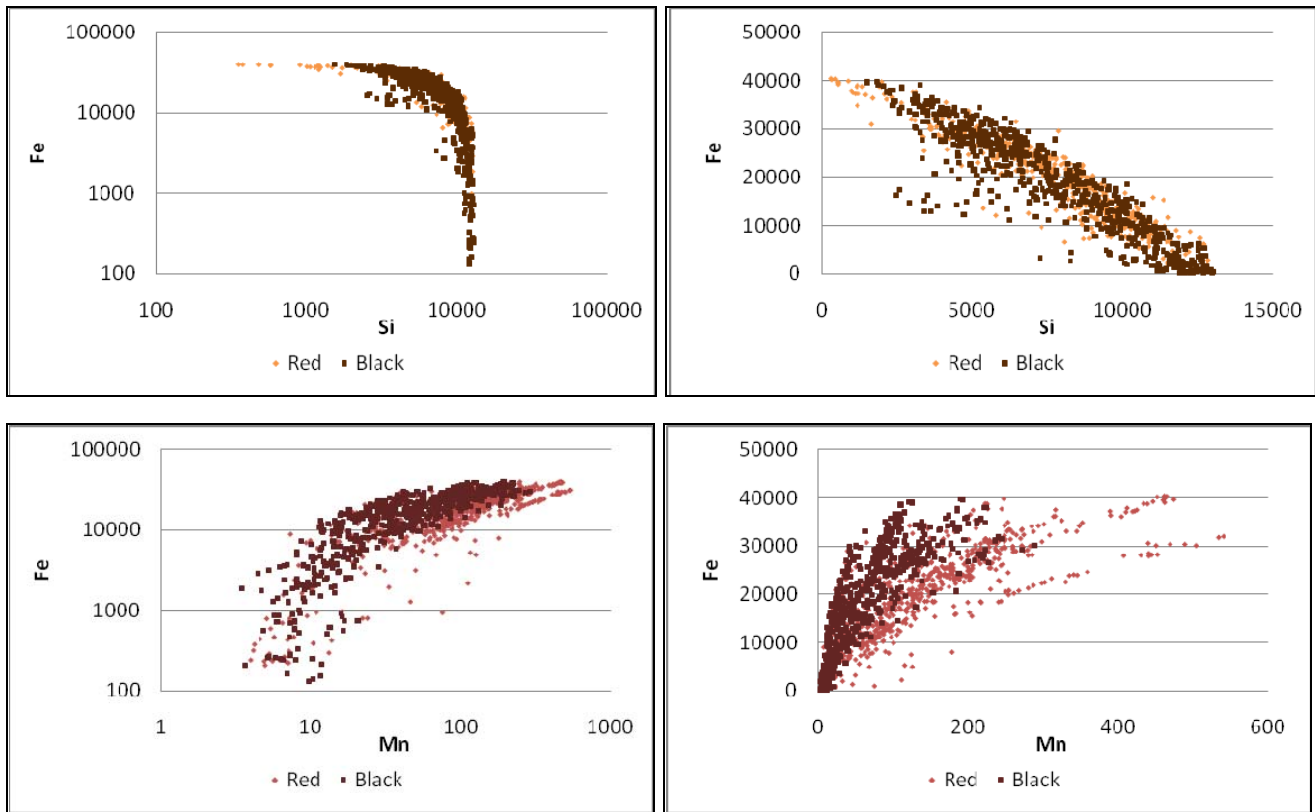
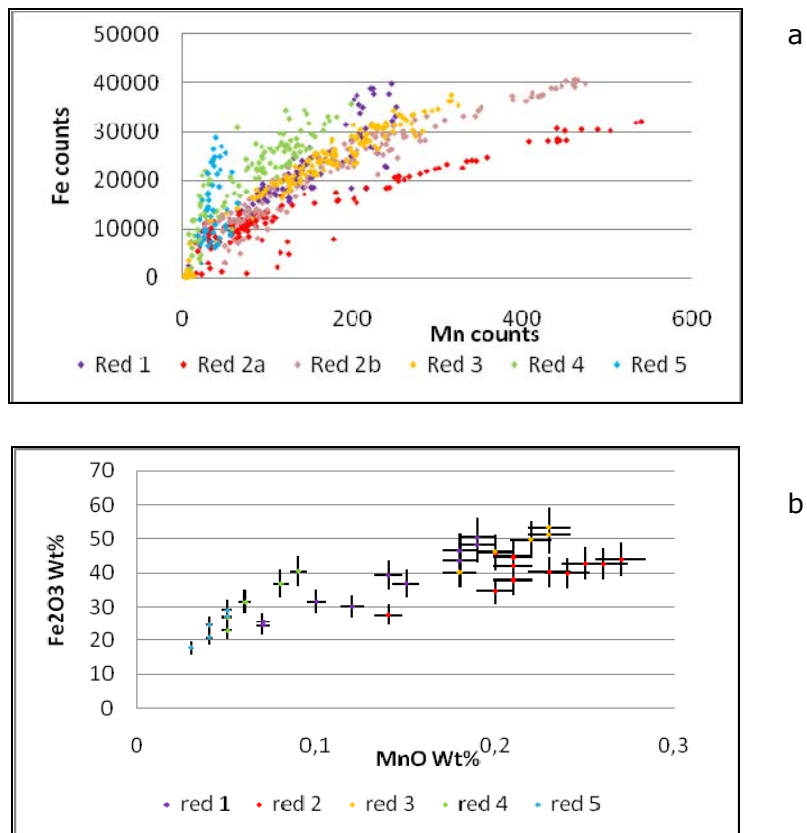


Figure 4.9 Si-Fe and Mn-Fe diagrams for the red and black Fe-rich layers of sample 1 (logarithmic and normal scale).



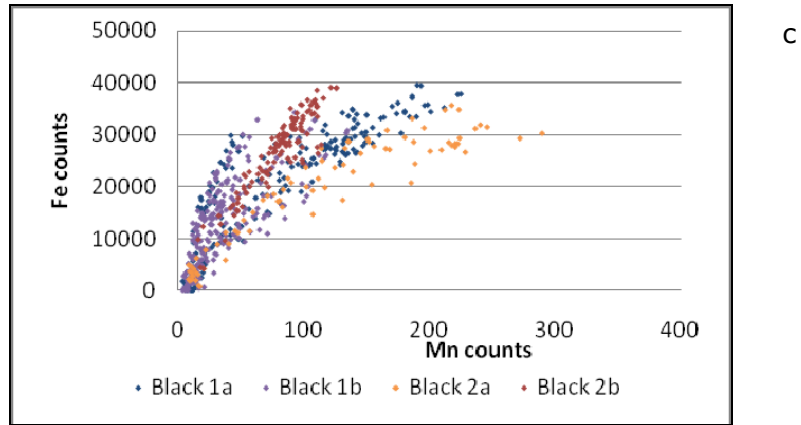


Figure 4.10 Fe-Mn diagrams for the red (*a*, *b*) and black (*c*) layers of sample 1 (normal scale), with individual layers shown in different colors. Note the varying Fe-Mn relationships in the red layers. The qualitative data (*a*, *c*) are the same as in Figure 4.9. Due to the large (2-mm) beam size needed for the quantitative data (*b*), it was not possible to distinguish between red 2a and red 2b. Error bars in the diagram with quantitative data for the red layers are based on errors for the Fe-rock standard (see Chapter 3).

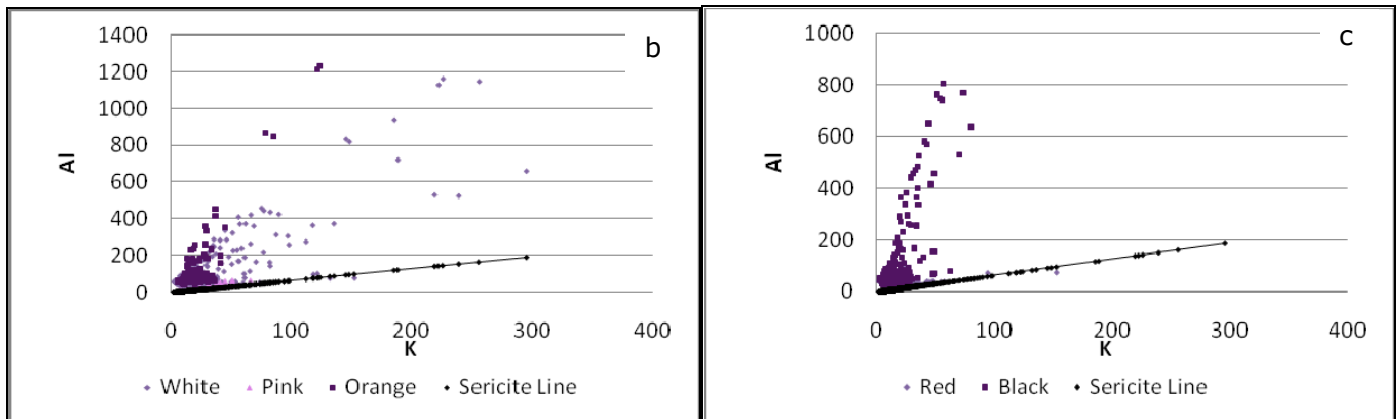
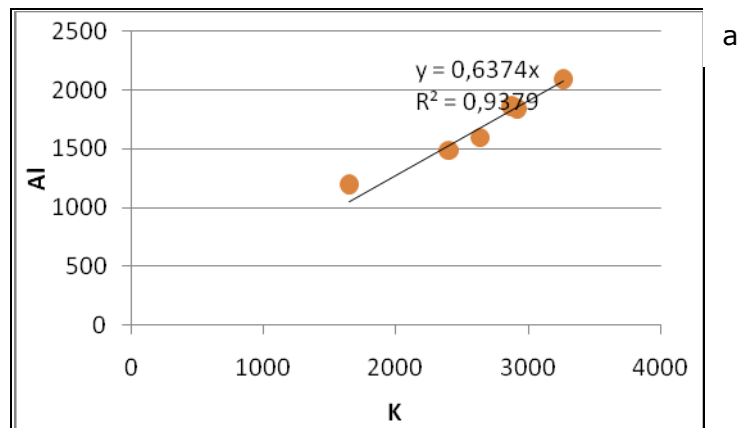


Figure 4.11 Al-K diagrams. (*a*) sample 2; six points where sericite was identified were plotted to create a sericite identification line. (*b*) Si-rich layers of sample 1 the with the sericite identification line. (*c*) Fe-rich layers of sample 1 with the sericite identification line.

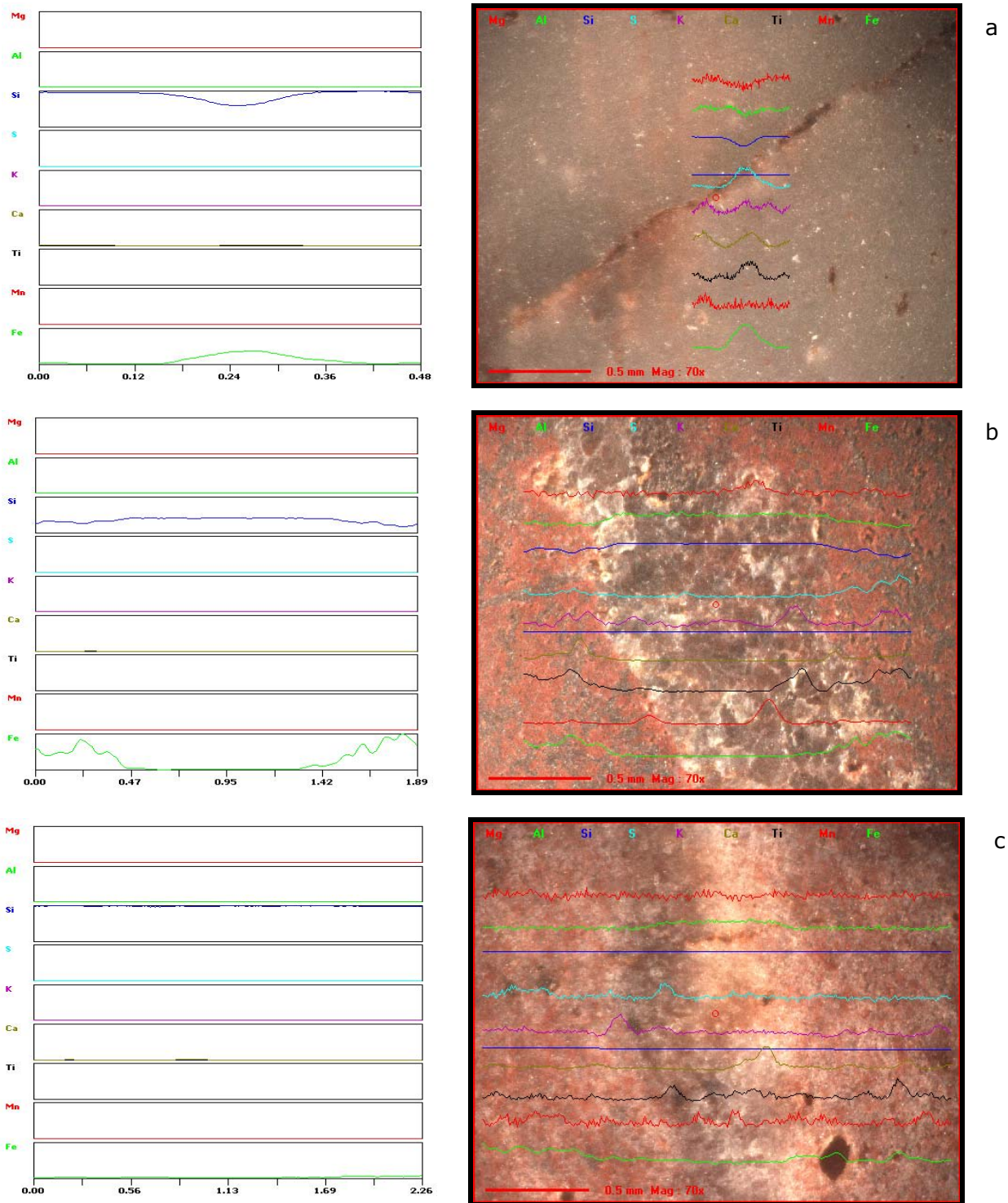


Figure 4.12 Line scans through veins from in sample 1. All the elements are displayed at the same scale in the graphs, but at different scales in the images to highlight (minor) variations. Note that iron and silicon are the main elements. The straight blue line in the center of the image is the line where the scan was actually made. a) Vein linescan 1 (V1). b) V2. c) V5. Note that Al, Ca, K, Mg, S and Ti data can be ignored.

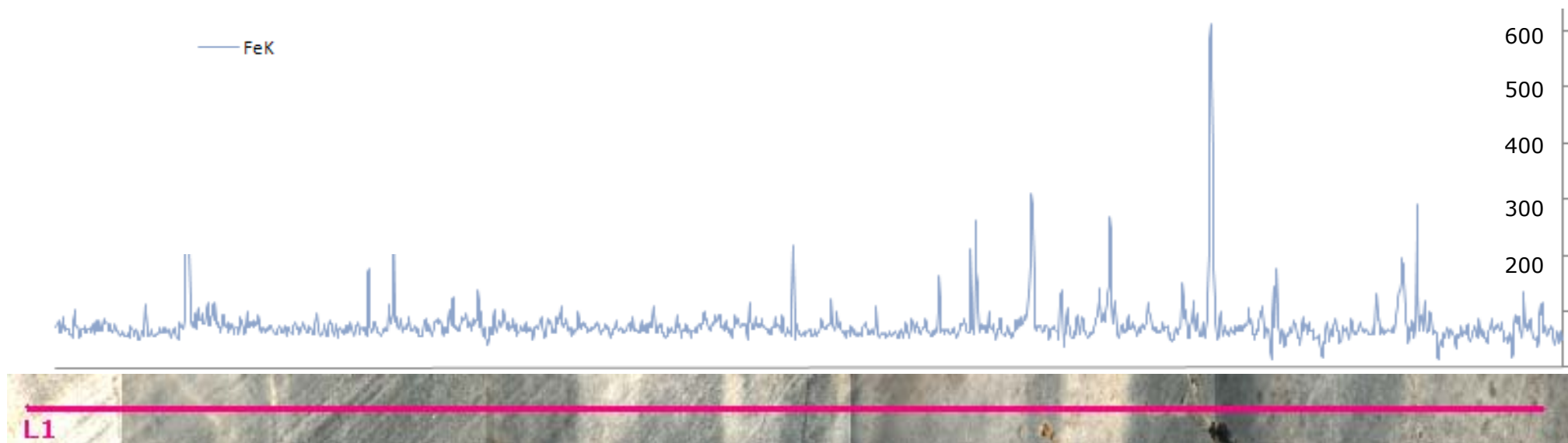
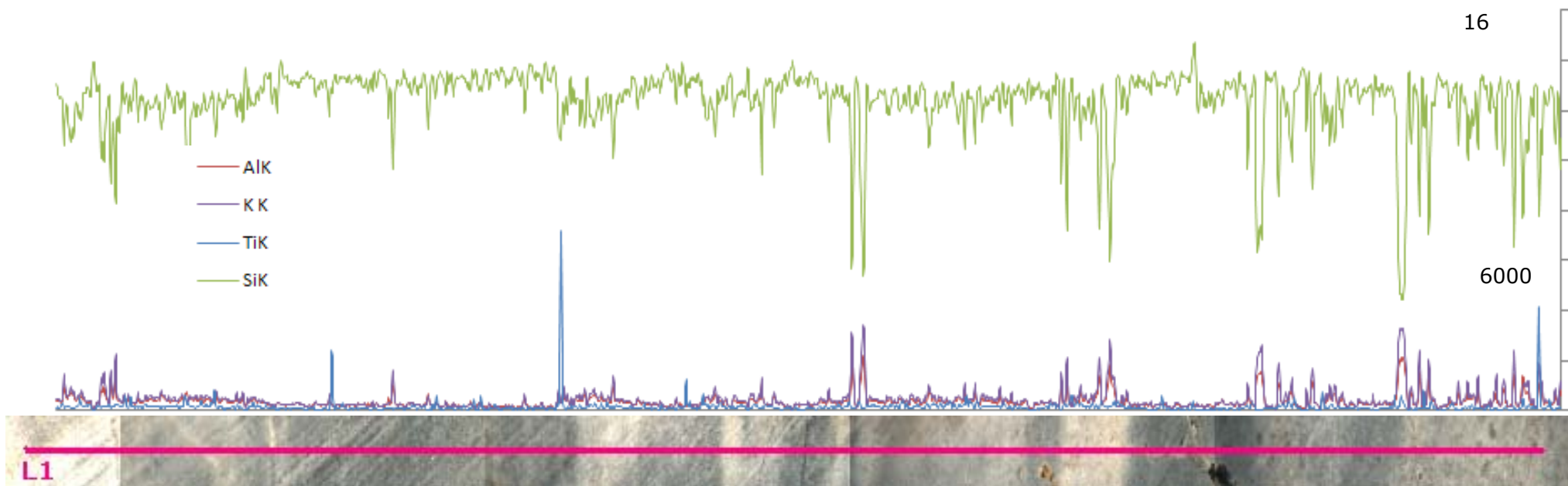


Figure 4.13 Major and minor element linescan 1 (K-lines) in sample 2. Length is ~6 cm.

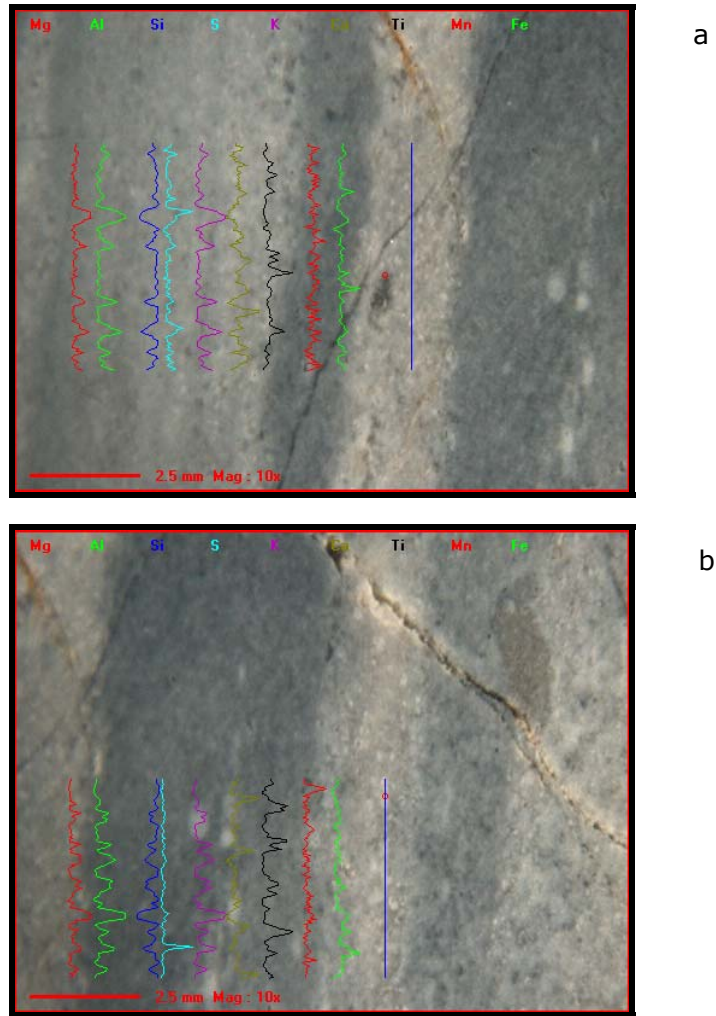


Figure 4.14 Linescans in sample 2. Elements are displayed at different scales. Note that silicon is the most abundant element. The straight blue line in the centre of the image is the line where the scan was actually made. a) Linescan 2 (L2). b) L5. Note that the Ca, Mg, Mn, S and Ti data can be ignored.

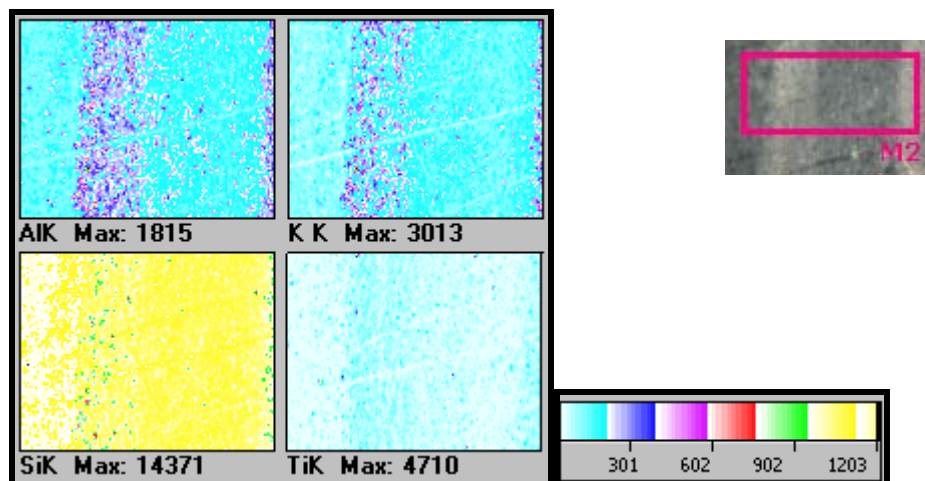


Figure 4.15 Element maps of sample 2 (M2). The color scheme (scale on the right) was adapted to improve the concentration contrasts. Note that the 4:5 dimensions of the shape here deviate from the actual measured M2 surface. The approximate size of the map is 0.7 x 0.3 cm.

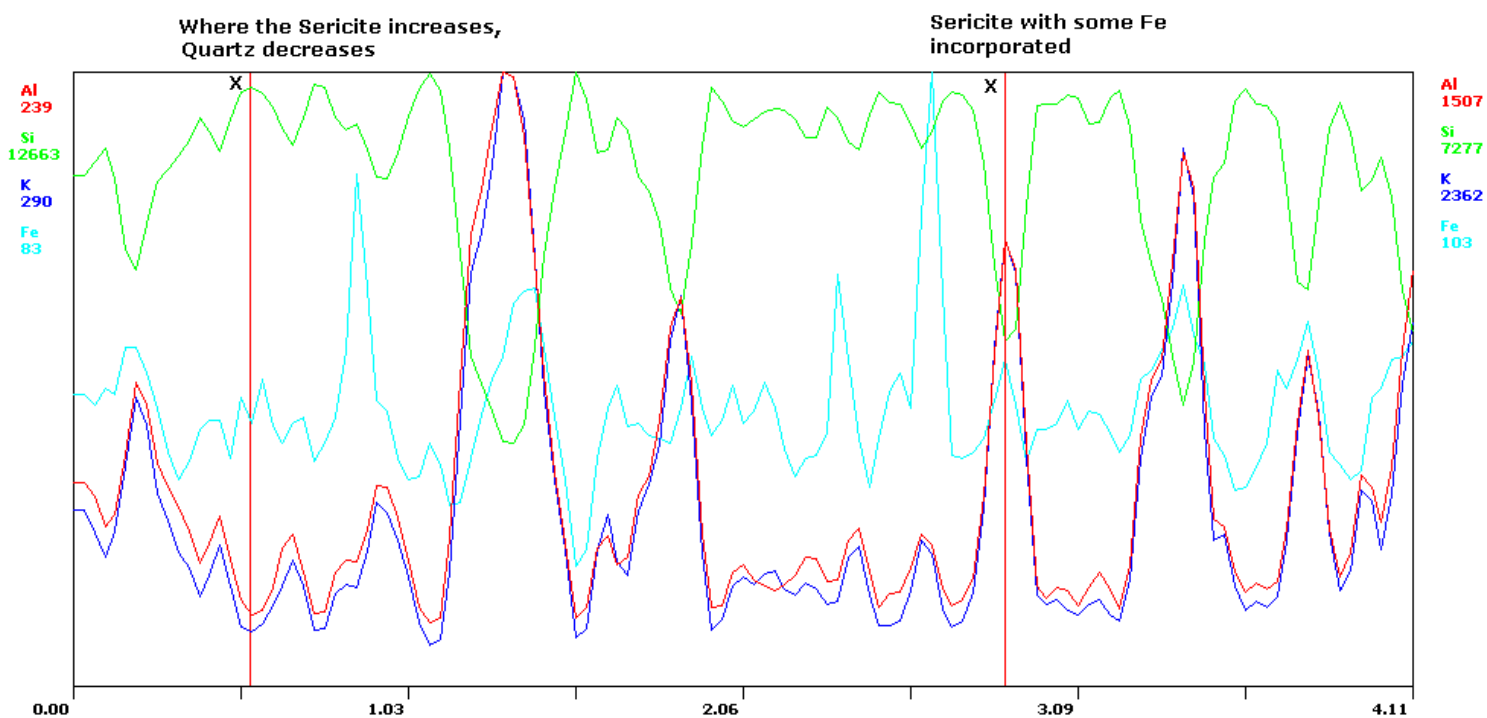


Figure 4.16 Element overlays for sample 2, showing the presence of sericite and quartz in a white layer (L3). Similar trends were observed in the other layers.

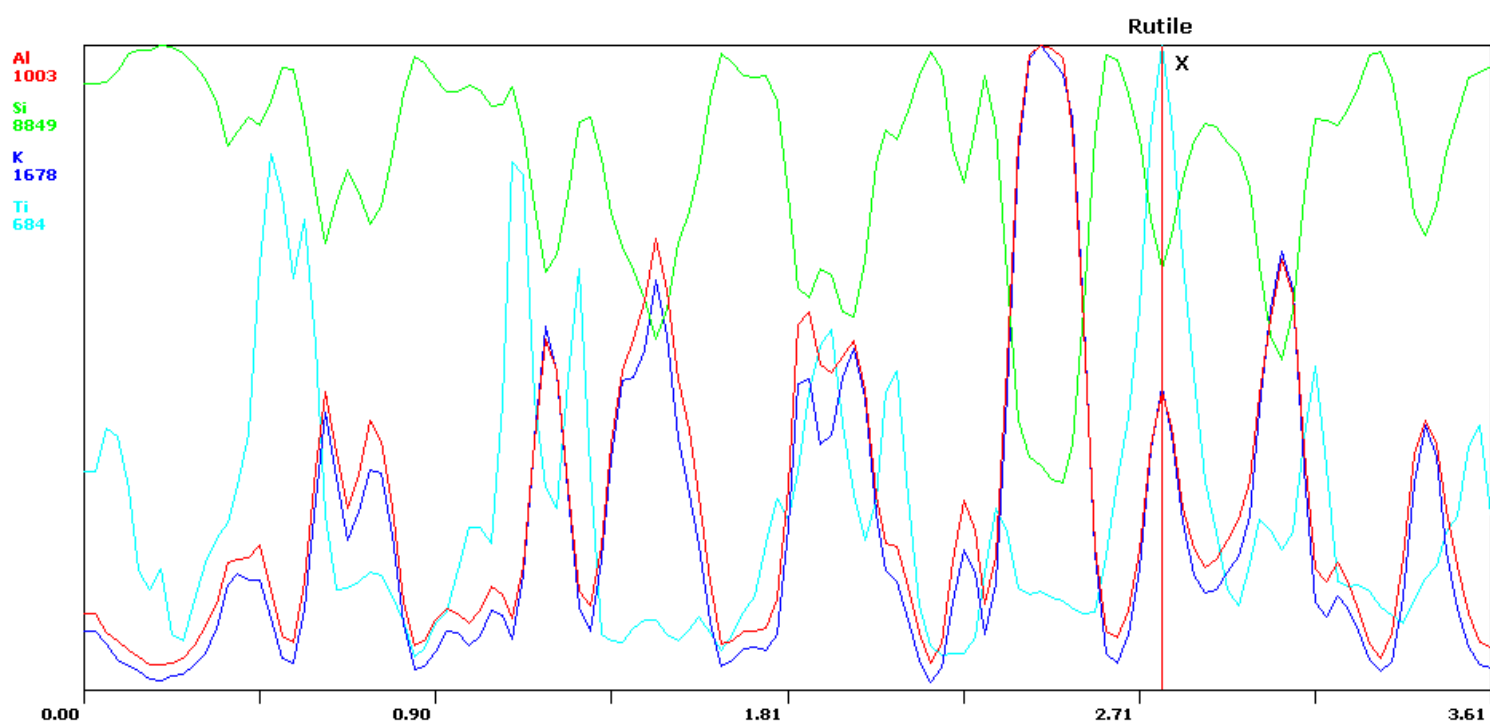


Figure 4.17 Element overlays of sample 2, showing the possible presence of rutile grains in a light layer (L5). Similar peaks were observed in the other layers.

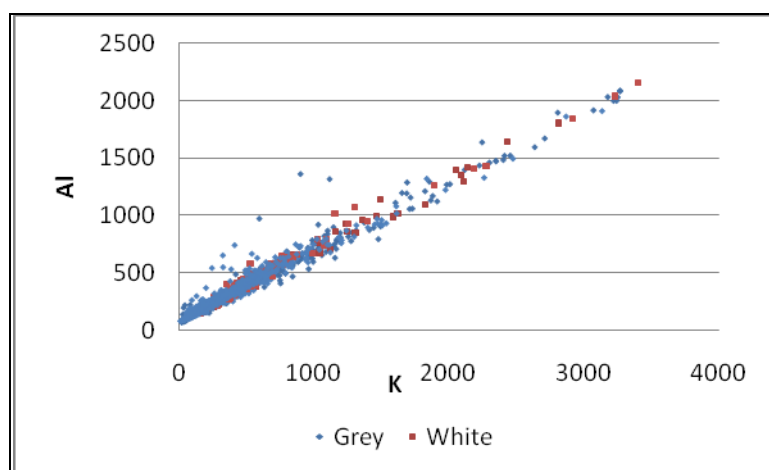


Figure 4.18 K-Al diagram for sample 2, suggesting that grey and white layers represent mixtures of quartz (low Al and K) and sericite (high Al and K).

4.4 Discussion

4.4.1 Sample 1 (C-chert): Red, Pink, White and Black layers

4.4.1.1 Quality of element analysis

Qualitative analyses were very good for Si and Fe since these elements are present in such high amounts that artifacts or statistical errors were negligible. Quantitative results involved errors in SiO_2 and Fe_2O_3 concentrations of ~ 10 wt%. Hence, μ -XRF spectroscopy is a suitable method to quickly determine variations in the concentrations of major elements between the layers of finely laminated cherts, and to identify chert samples as either C or S-type.

Despite the relatively low count rates for *Mn*, the data for this element were reproducible and were not an artifact caused by the high amounts of Fe present. Previous work had already confirmed the presence of Mn (Van Bergen, pers. comm. 2010). From examination of several spectra it was concluded that background fits performed by the software were not satisfactory and resulted in slightly overestimated net intensities.

Since *Al* was mostly present in low amounts, the results for this element were generally unreliable and are therefore excluded from further interpretation. A likely explanation is that in the energy spectrum the Al K α -line is positioned on the slope of the Si K α -line. High Si concentrations thus appeared to give the Al data a false boost. However, the Al peaks observed in linescans are real since the count rates increased about tenfold.

The low intensities for *K* should be ignored for statistical reasons, but the slightly higher count rates might be of use in combination with the associated Al peaks. Given the low concentrations of *Ca* and *Mg* these elements should be ignored as well.

The data for *S* were discarded because its K α -line is too close to the Rh line which resulted in erroneous data.

The putative presence of low amounts of *Ti* could not be confirmed. From inspection of the spectra it appeared that the counts assigned to Ti actually represented background radiation, or had been influenced by escape (the kV of a given element, here Fe, minus 1.74 kV of Si of the detector) or diffraction peaks.

In summary, the only concentrations reported for the C-chert sample are SiO₂, Fe₂O₃^{total} (all iron taken as Fe³⁺) and MnO. For SiO₂ and Fe₂O₃^{total} this was determined by their large share in the overall composition of the chert, and for MnO by its unequivocal relationship with Fe₂O₃^{total} visible in the qualitative data. The other elements (Al, K, Mg, Ca, S, and Ti) generally yielded results that were too unreliable for use due to the large errors involved at very low concentrations (see *Chapter 3*).

4.4.1.2 Red and black layers

The Fe-Mn diagram for these dark layers points to the presence of different mineral phases that host these elements, or to a single phase with variable Fe/Mn ratios. Possible genetic explanations will be discussed below. Overlaps at low Fe and Mn concentrations in the logarithmic graph may partly reflect inadequate definitions of boundaries between the layers.

The slight curvatures in the Fe-Mn graphs for the red and black layers are possibly an effect of an imprecise background definition, which would particularly affect the net count rate for Mn, given its much lower concentrations relative to Fe. This error diminishes at higher Mn concentrations, coinciding with higher Fe concentrations, which explains the curvatures of the trends.

4.4.1.3 Pink and orange layers

From a comparison with white layers it was found that only 1-2.6 wt% Fe₂O₃ gave the color to these layers and make them appear as pink (*Table 4.3*). Part of this Fe content comes from Fe-rich grains present in the matrix (*Figure 4.19*). White layers without such grains contain only 0.4 wt% Fe₂O₃, while the other two that do contain Fe-rich grains, have Fe₂O₃ contents >1 wt%.

A possible explanation for the periodicity of these layers, apparent from their comparable thicknesses, will be discussed below.

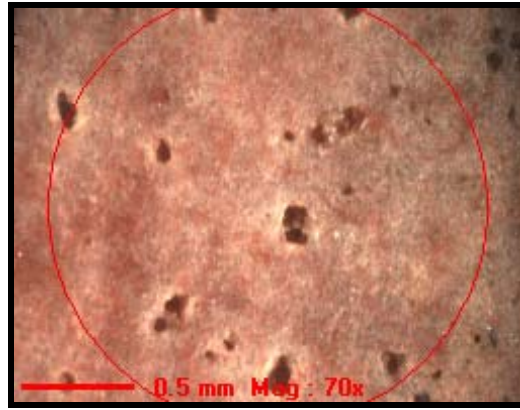


Figure 4.19 Area of a pink layer in sample 1 targeted for quantitative analysis. Red circle indicates the size of the beam created by the 2 mm aperture. Brown, Fe-rich grains can be seen in the pink, Si-rich matrix.

4.4.1.4 White layers

The Fe-Mn diagrams for this group of Si-rich layers shows two data clouds with different densities. A comparison with Fe-Mn diagrams for the Fe-rich layers suggests that the dense cloud represents a mineral phase present only in the Si-rich layers, while the other cloud appears to signal a phase similar to one present in the Fe-rich layers.

The Al peaks in *Figure 4.4* might reflect some Al substitution for Si, but is more likely attributable to the presence of an Al-bearing phase next to quartz. Because K shows enrichments at the same locations as Al, this mineral is probably feldspar (rather than sericite which is not expected in this type of chert).

4.4.1.5 Minerals

Options as to minerals present in the *red and black* layers are hematite, goethite, magnetite, and siderite (*Table 4.5*). The quantitative data could not distinguish between these Fe-rich minerals, partly because no oxygen was measured. Because of this uncertainty and because the red versus black coloring could not be related to compositional differences, it is assumed that the color variations are caused by different populations of Fe-(hydr)oxide minerals.

The Fe-rich mineral(s) responsible for the *orange* color of several layers could not be identified. One of the four Fe-minerals suggested being present in the red and black layers is a conceivable option. The same could be valid for the *pink* layers.

The dominant mineral in the *white* layers is presumably quartz, since SiO₂ as main oxide is present in amounts of ~89 wt%. The small amounts of Fe in the white layers likely result from measurements across boundaries with Fe-rich layers.

4.4.1.6 Veins

Roughly coinciding trends of Al and Si in the Si-rich vein shown in *Figure 4.12b* might suggest Al substitution for Si but a more likely explanation is an artifact of the method, since the Al line used lies on the slope of the Si line in the energy spectrum.

Some of the 'veins' have compositions almost equal to that of their host, despite color variations (*Figure 4.12c*). Minor element distributions could be responsible, so that these phenomena may thus not represent veins.

4.4.2 Sample 2 (S-chert): White and various Grey layers

4.4.2.1 Quality of element analysis

The results for *Si* data were of the same good quality as those obtained on sample 1, since it is the main element also here. In contrast, low amounts of *Fe* resulted in poor statistics. Some higher peaks represent elevated concentrations of Fe as constituent of a mineral phase. The same observation applies to *Ti*.

The other main elements in this sample are *Al* and *K*. Their analytical results are suitable to use for interpretations.

The *Mg* data were discarded due to very low count rates, as were the *S* data because of interference with the Rh line. In the linescans, *Ca* and *Mn* were not detectible above the background radiation.

4.4.2.2 Laminations

The laminae in this sample did not consistently display obvious chemical and visual differences. This suggests that the bulk composition of this chert is close to that of the individual layers. Either small chemical differences could not be detected with the μ -XRF for the elements investigated or they are due to minor or trace elements that were not measured. It is unlikely that the laminae were created by changes in depositional process, but fluctuations in sediment supply (e.g. type of sediment) might have been responsible instead (see discussion below).

The main minerals inferred to be present in this S-chert were quartz (chert) and Fe-bearing sericite. This was most evident in element maps (*Figure 4.16*) which showed that quartz (Si) contents decrease when sericite (K and Al) contents increase. Rutile was found as an accessory mineral.

The white layers probably contain more sericite than the grey layers, but the evidence is not fully conclusive. Positive relations between Al and K in the linescans and maps would confirm this, but an Al-K plot (*Figure 4.18*) is unconvincing.

4.4.3 Background on Archaean environments of chert deposition

Present-day hydrothermal settings can be taken as analogue for ancient (Precambrian) systems (Baross and Hoffman, 1985; De Vries, 2007) even though properties of the oceans probably have changed. The terrestrial trace-element signature of modern seawater is similar to that in the Archaean, indicating that processes controlling these signatures have remained rather constant (Bolhar et al., 2005). The Galapagos spreading center and associated hydrothermal mounds is a possible analogue for Archaean depositional settings of BIFs (Dymek and Klein, 1988). Similarities in REE signatures point to parallel genetic processes. However, deposition of Mn-oxides at the oxygenated seawater-sediment interface of the Galapagos mounds (Lalou et al., 1983) contrasts with the low Mn contents generally found in BIF samples, which may reflect the more reducing conditions of the Archaean.

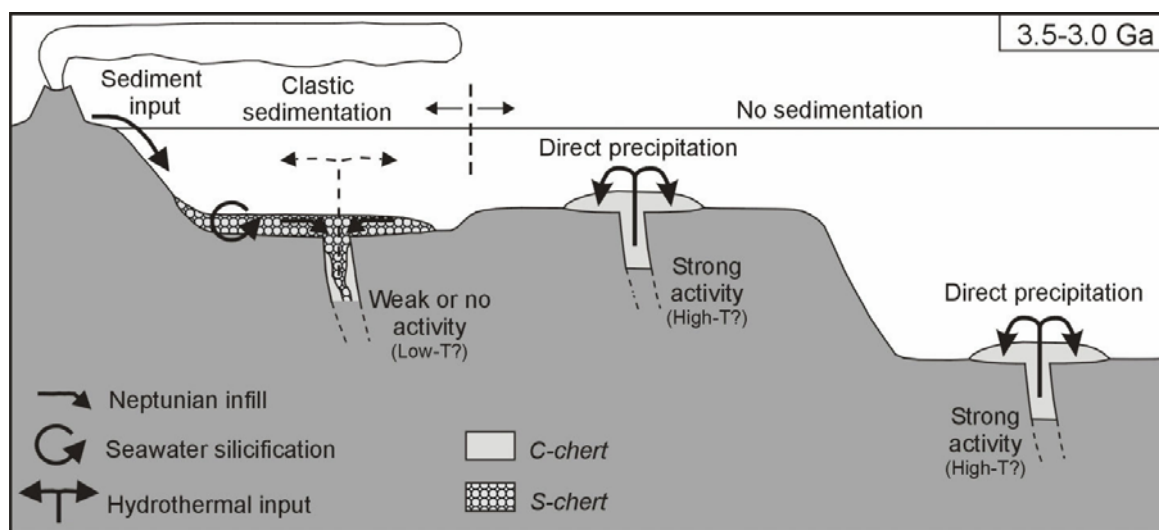


Figure 4.20 Schematics of Archaean chert formation. S-cherts (and dikes) formed in sediment-rich near-shore environments, whereas C-cherts originated in shallow or deep marine environments with low sediment input and relatively high hydrothermal activity. (Source: Van den Boorn, 2008)

Cherts have been deposited in various environments, ranging from shallow platforms to deep marine, are also found in lakes (Lowe; 1999, referred to in Rouchon, 2008). *Figure 4.20* pictures a generalized scheme of chert-forming settings in the Archaean as envisaged by Van den Boorn (2008), direct precipitation of cherts (or BIFs) occurred from mixtures of hydrothermal vent fluids and seawater in regions of low sedimentation. The silica in these chemically precipitated cherts (C-chert, sample 1) is believed to be

largely of hydrothermal origin, as is the associated Fe. Silica and Fe-(hydr)oxides thus formed where hydrothermal fluids came into contact with ocean water.

In contrast, silicified precursor cherts (S-chert, sample 2) are silicification products of sediments that interacted with seawater. Any hydrothermal activity was probably minor. The silica is derived from the precursor sediment and from seawater that was saturated in silica in absence of silica-secreting organisms (De Vries, 2004). These cherts are Fe-poor but relatively rich in Al and Ti, as is expressed in the presence of mica and Ti-oxide.

Other hypothesized chert-forming environments include active calderas (Van Kranendonk et al., 2003; Bolhar et al. 2005) and areas where 'standard' hydrothermal venting is followed by transport to shallow shelves (Gnaneshwar Rao, and Naqvi, 1995; Sunder Raju, 2009). Although the deposition model of Van den Boorn et al. (2008) was adopted for the samples investigated here, these other models are briefly reviewed, as they provide additional insights into alternative chert-forming processes.

A volcanic caldera setting was put forward to explain jasper and siderite bandings found in Archaean cherts (and BIFs) from other regions in the Pilbara craton than where the studied samples came from. Van Kranendonk et al. (2003) proposed that seawater entered the crater periodically during periods of hydrothermal quiescence and was diluted by hydrothermal fluids that were still present. Jasper precipitated during the periods of low hydrothermal activity, whereby the Si was primarily supplied by saturated seawater, and the Fe (hosted by hematite and goethite, which give the jasper its reddish color) by the residual hydrothermal fluids. During periods of increased hydrothermal activity, siderite was deposited. Bolhar et al. (2005) and various others (e.g., Coale et al., 1991; Morris, 1993) suggested that the periodicity was caused by varying hydrothermal intensities or changes in the magma reservoir. Alternatively, changing permeabilities, driven by hydrothermal sediment accumulations, played a role (Moorby, 1983). The fine laminations -characteristic for many Archaean cherts - might be associated with syn-sedimentary diagenesis (Chown et al., 2000).

The second alternative (Gnaneshwar Rao, and Naqvi, 1995; Sunder Raju, 2009) involves basin-wide circulation, whereby warm and Si+Fe enriched hydrothermal fluids migrated to shallower shelf regions, where ferrous iron oxidizes and iron(hydr)oxides formed. Settling of these minerals as well as silica would then have produced BIFs during periods when the coast receded and low energy conditions prevailed. This model seems inadequate for the samples examined as it would not explain the fine laminations and the absence of pyrite grains of various sizes that should be common (Gnaneshwar Rao and Naqvi, 1995; Sunder Raju, 2009).

BOX 4.1 Trace element and Si-Isotope Characteristics of the investigated Archean cherts

Besides the major and minor element constituents investigated here, trace element and isotope ratios provide important information on the origin of Archean cherts (Usie et al., 1997; Leistel et al., 1998; Bolhar et al., 2004, 2005; Chu et al., 2006; Van den Boorn, 2008; Van den Boorn et al. 2010). As summarized in the *Table* below, cherts of hydrothermal and seawater origins have different REE and Si-isotope characteristics, which may also vary depending on the specific site and other aspects, e.g. the nature of terrestrial input. Hence, trace-element and stable-isotope data are sometimes inconclusive. Nevertheless, Y/Ho and $\delta^{30}\text{Si}$ signatures appear to be diagnostic. Cherts with a dominant hydrothermal source mainly display chondritic Y/H₀ ratios and negative $\delta^{30}\text{Si}$ values, while cherts that are derived from seawater have superchondritic Y/H₀ ratios and positive $\delta^{30}\text{Si}$ values.

The *Table* lists some geochemical characteristics by which seawater and hydrothermal fluids have been distinguished as source of chert-forming constituents (e.g., Van den Boorn et al., 2010). Anomalously high Eu values could be attributable to enrichment due to continental crust erosion (Bolhar et al., 2004). The REE+Y patterns of S-chert are less diagnostic because these signatures are often dominated by the precursor material (Van den Boorn, 2008).

	Seawater origin	Hydrothermal origin
Y/Ho ratio	26-44 ^{***} , 29-72 [^] , Superchondritic ^{***, ***} (depending on the formation)	Chondritic ^{***} (25.4±0.6 ^{**}) (depending on the formation)
Eu/Eu* ratio	1.8-5.6 [^]	1.7-2.4 ^{***} , Positive ^{***, ***, ^*}
Ce anomalies	Positive ^{*, ^} , negative ^{***}	Negative [*]
La anomalies	Positive ^{***, ***, ^}	Positive ^{^*}
$\delta^{30}\text{Si}$	Positive (0.1 to 1.1‰) and negatively correlated with Al ₂ O ₃ [^]	Negative (-2.4 to +0.6‰) ^{^*}
Other	LREE and HREE depletion and enrichment ^{***, *, ^, ^*}	LREE depletion ^{^*} , LREE enrichment ^{***}

Table Trace-element and isotope properties of different chert types. Sources: *Usie et al., 1997; **Van Kranendonk et al., 2003; ***Bolhar et al., 2005; ^{*}Chu et al., 2006; [^]Van den Boorn, 2008 and sources therein; ^{^*}Van den Boorn et al., 2010. Note that the Y/Ho ratios from Van den Boorn were taken from the Kitty’s Gap (Panorama Fm.) and Marble Bar (boundary between the Coogan and Salgash Subgroups) cherts, while Bolhar et al. sampled the North Pole area northwest of Marble Bar (Panorama Fm.).

4.4.4 Implications from the analytical results

The results from the Sample 1 C-chert are consistent with data obtained on the same sample by Van den Boorn (2008) and with other findings at Marble Bar (Kato and Nakamura, 2003). The red, black and white layers of various thicknesses point to changes in the composition of precipitated material and thus in the conditions of deposition. The dark Fe-rich layers may have been deposited when hydrothermal activity prevailed, and the Fe-poor white layers when it was almost nonexistent. Given their regular spacing and thickness, the pink layers may represent a periodicity in hydrothermal activity of moderate intensity when fluids mixed with larger amounts of seawater, similar to what was described above for jasper deposition during periods of volcanic quiescence.

The red-black color differences between the Fe-rich layers of Sample 1 might be attributable to changes in mineral composition, which, in turn, may reflect a different precipitation process, or a shift in the composition of the hydrothermal fluid, caused by changing water-rock interactions. Since the μ -XRF could not distinguish between various Fe-minerals, such changes in precipitation processes are difficult to constrain. Presumably, the redox and pH conditions played a role since Archaean hydrothermal fluids may have been relatively acidic and reducing (Bolhar et al., 2005).

The most remarkable discovery was the Fe-Mn relationship whereby Fe/Mn ratios of individual layers appeared to change in stratigraphic order (*Figure 4.13*). Presumably, Mn^{2+} ions replaced Fe^{2+} ions in Fe-rich minerals to a variable extent, since these two elements have comparable ionic radii and valencies. This type of replacement is still observed today (e.g., Ishibashi et al, 2008). If it is assumed that the hydrothermal fluid supplied both elements, the Fe/Mn variations could be indicative for changes in hydrothermal activity or in the conditions that controlled their uptake in minerals. The hypothesis of a hydrothermal supply is reasonable, because concentrations of Fe and Mn in these fluids are approximately six times higher than in normal seawater (Chu et al., 2006 and sources therein). It is thus conceivable that the Mn content of the hydrothermal fluids, relative to Fe, increased or decreased with changes in water-rock ratios (cf., Hajash and Archer, 1980), or with progressive maturation of the percolated host rock at depth.

However, because Mn in hydrothermal fluids is present in similar amounts as Fe (Morris, 1993), it must be explained why the Mn contents in the cherts are orders of magnitude lower than the Fe contents. Considering the overall low Mn contents in BIFs, either Fe is favored over Mn during precipitation, or Mn is directly re-dissolved again (Morris, 1993). Fractionation between Fe and Mn during BIF formation is probably highly efficient

(Gnaneshwar Rao, and Naqvi, 1995), whereby degree of oxidation and pH are probably important controls. At relatively oxidizing conditions and neutral or acidic pH, manganese tends to be more soluble than iron (Glasby and Schultz, 1999), so that precipitation of Fe-rich minerals is favored. Hence, the changing Fe/Mn ratios observed in Sample 1 could be the result of variations in oxidation state and/or pH. Alternatively, precipitation of multiple Fe-minerals in different proportions may have affected the Fe/Mn ratio.

According to Van den Boorn (2008), S-cherts were deposited in a near-shore environment where terrestrial sediment supply was high. These sediments were subsequently replaced by silica. The resulting chert retained some characteristics of the precursor sediment and other minerals such as sericite. The sericites in sample 2 are probably alteration products of feldspars present in the volcanic precursor rock (Van den Boorn, 2008). The rutile grains that appeared as Ti spikes are residues that survived the silicification process. Zircon was also expected as an insoluble residue in sample 2, but could not be detected with the μ -XRF.

Background information on trace-element and Si-isotope signatures for a hydrothermal or seawater origin can be found in *Box 1*,

4.5 Conclusions

C-cherts show stronger visible and chemical differences between laminae than S-cherts.

The distinct layers in the C-chert sample range in composition from almost pure Si to Si and Fe-rich, whereas the entire S-chert sample is characterized by high contents of Si, Al and K.

As expected, Si and Fe are the principal elements of the C-chert that also determine its layering. Layer colors correspond to chemical compositions: red and black layers are Fe-rich, white layers are Si-rich and Fe-poor, and orange or pink layers are Si-rich with minor amounts of Fe. Compositional systematics point to the presence of quartz, Fe-oxides and/or Fe-carbonates, and possibly some feldspar. The Fe-rich minerals are unidentified but could be (a combination of) goethite, hematite, magnetite, and siderite. They are abundant in the red layers. Systematic variations in Fe/Mn ratios of these layers probably reflect fractionation between these elements induced by changing conditions in the depositional environment near hydrothermal vents.

Key differences between and within layers of the C-chert are summarized in *Table 4.6*.

Inter-layer variations	<i>Red and Black</i>	<i>Pink</i>	<i>White</i>
	Si- and Fe-rich with minor Mn	Si-rich with minor Fe	Si-rich
Intra-layer variations (inferred minerals)	<i>Red and Black</i>	<i>Pink</i>	<i>White</i>
	Hematite, Goethite, Magnetite, Siderite (potentially present)	Mainly quartz in the Si-rich matrix; minor amounts of Fe-rich grains, probably similar to those in the red layers	Quartz

Table 4.6 Summary of inter- and intra-layer variations in the C-chert.

The main elements in the S-chert are Si, Al and K. The element trends point to quartz and sericite as dominant minerals. Some rutile grains are present as well. Layering tends to correspond to sericite abundance, but evidence is not always conclusive.

Results for elements should be considered with care or should be discarded are listed in Tables 4.7 and 4.8 for samples 1 and 2, respectively.

Elements Sample 1	Reasons for taking extra care or elimination
Al	Only applies at low intensities. Al K α -line sits on the slope of the Si K α -line and can only be used when concentrations are sufficiently high.
Ca	Large errors due to low concentrations make data unreliable
K	Large errors due to low concentrations make data unreliable
Mg	Large errors due to low concentrations make data unreliable
S	K α -line is too close to the Rh line
Ti	Large errors due to low concentrations, Fe escape and/or diffraction peaks

Table 4.7 Overview of elements in sample 1 that should be viewed with care or should be discarded.

Elements Sample 2	Reasons for taking extra care or elimination
Ca	Large errors due to low concentrations make data unreliable
Fe	Large errors due to low concentrations make data unreliable but Fe-rich phases are detectible
Mg	Large errors due to low concentrations make data unreliable
Mn	Large errors due to low concentrations make data unreliable
S	K α -line is too close to the Rh line
Ti	Large errors due to low concentrations make data unreliable but Ti-rich phases are detectible

Table 4.8 Overview of elements in sample 2 that should be viewed with care or should be discarded.

Collectively, the μ -XRF results are consistent with the distinct origins of the investigated chert samples proposed by Van den Boorn et al. (2008). These authors inferred that C-cherts formed as chemical precipitates from mixtures of hydrothermal fluids and

seawater near submarine vents, whereas S-cherts represent volcanic precursor sediments that were silicified by silica-saturated seawater.

Given this context, the pink layers in the C-chert sample likely formed during periods of low hydrothermal activity when seawater dominated in the fluid mixtures and only minor hydrothermal supplies of iron were sufficient to yield the pink color. The red/black and white layers represent periods of intense and no hydrothermal activity, respectively. The red and black layers have comparable major element compositions, so that the reason of this color difference remains obscure.

General Conclusions and Recommendations

This research has demonstrated the suitability of the μ -XRF technique for acquiring compositional information on geological samples at mm-cm scale. Following a comprehensive initial test phase, it was possible to rapidly determine variations between and within laminae of Archaean cherts in a non-destructive way, and to draw conclusions concerning their origin.

The Orbis μ -XRF appeared to produce fairly good qualitative results when using a 30- μ m polycapillary, an amplifier time of 6.4 μ s, and voltages between 20 and 30 keV. An appropriate current should be chosen in relation to the expected dead time, which should preferably not exceed 30%. Similar settings can be used for quantitative analysis, but a 2-mm aperture instead of the polycapillary should be used to minimize possible effects from small-scale sample inhomogeneity. Quantitative results tended to gain accuracy at higher currents. Analytical error in quantitative determinations of major elements was ca. 10%, which allowed obtaining adequate insights into compositional variations of the chert laminae.

Advantages of μ -XRF spectroscopy as analytical technique are that the instrument proved easy to use, that not much sample preparation is needed, and that it produces qualitative results rather fast. The μ -XRF can cope with various types of samples, and their surfaces do not need to be smooth. Still, it appeared that flat samples were easier to work with, as less focusing was needed and less spectral artifacts were produced. When working with irregular surfaces, use of the autofocus mode is recommended to ensure that results are meaningful. Depending on the size of an area of interest, detailed chemical maps could be generated within hours of scanning time. When creating line-scans in auto-mode, spectral data from individual spots could be stored in formats suitable for off-line processing with standard software.

The quantitative results were obtained by using the standardless routine provided with the instrument. Its reliability was tested by analyzing geological materials with known compositions. Although reproducibility is good, concentrations could deviate by \sim 10% from recommended values, even for highly abundant elements. More testing and measurements against validated standards are recommended to improve the accuracy of results.

Encountered disadvantages mainly concern design and available software. Because magnifying cameras and the X-ray detector are positioned at different angles to the sample, overlays of image and element-intensity graphs were not always precise, and element maps were often shifted relative to the designated area. Also, the data

reduction software used could not produce acceptable quantitative data for minor and trace elements, while errors for major elements ranged between 0.5 and 20%. The handling of sum peaks, escape peaks and diffraction peaks in the spectra needed special attention.

The overall conclusion of this work is that μ -XRF technique promises to be a versatile in-situ technique for analysis of solid geological materials that bridges the gap between standard XRF analysis of bulk samples and electron-microprobe analysis at micron-scale. Considerable analytical effort remains needed to obtain μ -XRF data of comparable quality as these techniques.

Acknowledgements

My gratitude goes to Manfred van Bergen for his guidance and comments, to Paul Mason for being my second advisor, to Tilly Bouten for her continued support and expertise with hard-headed analytical machines, and to the Deltares colleagues for kindly providing geological standards. I thank Loes van den Berg for assistance and Sander van den Boorn for his samples.

Literature

- Arai, T. (2006) *Handbook of Practical X-ray Fluorescence Analysis*, 1st ed. pp. 2, Springer, Heidelberg
- Baross, J. A. and Hoffman, S. E. (1985) *Submarine hydrothermal vent and associated gradient environments as sites for the origin and evolution of life*. *Origins of Life*, Vol. 15, pp. 327-345
- Beeson, S. and Mayer, J. W. (2008) *Physics and Astronomy, Patterns of Light*. pp. 157-164, Springer, New York
- Behrends, T. and Kleingeld, P. (2009) *Bench-top Micro-XRF – a useful apparatus for geochemists?* *Geochemical News*, Vol. 138
- Bolhar, R. et al. (2005) *A trace element study of siderite–jasper banded iron formation in the 3.45 Ga Warrawoona Group, Pilbara Craton—Formation from hydrothermal fluids and shallow seawater*. *Precambrian Research*, Vol. 137, pp. 93-114
- Bolhar, R. et al. (2004) *Characterization of early Archaean chemical sediments by trace element signatures*. *Planetary Science Letters*, Vol. 222, pp. 43-60
- Bolhar, R. et al. (2005) *A trace element study of siderite–jasper banded iron formation in the 3.45 Ga Warrawoona Group, Pilbara Craton—Formation from hydrothermal fluids and shallow seawater*. *Precambrian Research*, Vol. 137, pp. 93-114
- Boorn, Van den S. H. J. M. (2008) *Silicon isotopes and the origin of Archaean cherts*. PhD manuscript, pp. 1-6, 87-156
- Boorn, Van den S. H. J. M. et al. (2010) *Silicon isotopes and Trace elements in Early Archaean cherts*. *Geochimica et Cosmochimica Acta*, Vol. 74, pp. 1077-1103
- Bruker AXS (2010) *Working Principle*. Website visited January 13th 2010. <http://www.bruker-axs.com/xflashesddx-raydet0.html>
- Chown, E. H. et al. (2000) *The relation between iron-formation and low temperature hydrothermal alteration in an Archean volcanic environment*. *Precambrian Research*, Vol. 101, pp. 263-275
- Cloud, P. E. (1972) *A Working Model of the Primitive Earth*. *American Journal of Science*. Vol. 272, Iss. 6. pp. 537-548
- Coale, K. H. et al. (1991) *In situ mapping of dissolved iron and manganese in hydrothermal plumes*. *Nature*, Vol. 352, pp. 325-328
- Chu, N.-C. et al. (2006) *Evidence for hydrothermal venting in Fe isotope compositions of the deep Pacific Ocean through time*. *Earth and Planetary Science Letters*, Vol. 245, pp. 202–217

- Dymek, R. F. and Klein, C. (1988) *Chemistry, petrology and origin of banded ironformation lithologies from the 3800 ma Isua supracrustal belt, West Greenland*. Precambrian research, Vol. 39, pp. 247-302
- Edax, AMETEK Inc. (2009) *EDXRF training lectures Orbis setup and Hardware*
- Edax, AMETEK Inc. (2009) *EDXRF training lecture Properties and Production of X-rays*
- Floor, G.H. (2004) *Geochemical characteristics and origin of Early Archean cherts from Pilbara, Western Australia, and Barbeton, South Africa*. Thesis at Utrecht University. pp. 1-75
- Ginibre, C. et al. (2007) *Crystal Zoning as an Archive for Magma Evolution*. Elements, Vol. 3, pp. 261-266
- Glasby, G. P. and Schulz, H. D. (1999) *EH, pH Diagrams for Mn, Fe, Co, Ni, Cu and As under Seawater Conditions: Application of Two New Types of EH, pH Diagrams to the Study of Specific Problems in Marine Geochemistry*. Aquatic Geochemistry, Vol. 5, pp. 227-248
- Glikson, A.Y. (1971) *Primitive Archaean element distribution patterns: chemical evidence and geotectonic significance*. Earth and Planetary Science Letters, Vol. 12, pp. 309-320
- Gnaneshwar Rao, T. and Naqvi, S.M (1995) *Geochemistry, depositional environment and tectonic setting of the BIF's of the Late Archaean Chitradurga Schist Belt, India*. Chemical Geology, Vol. 121, pp. 217-243
- Hajash, A. and Archer, P. (1980) *Experimental Seawater/Basalt Interactions: Effects of Cooling*. Contrib. Mineral. Petrol., Vol. 75, pp. 1-13
- HORIBA, Ltd. (2010) *XRF Tutorial*. Website last visited January 21st 2010. <http://www.horiba.com/fr/scientific/products/x-ray-fluorescence-analysis/tutorial/>
- Ishibashi, J. et al. (2008) *Marine shallow-water hydrothermal activity and mineralization at the Wakamiko crater in Kagoshima bay, south Kyushu, Japan*. Journal of Volcanology and Geothermal Research, Vol. 173, pp. 84-98
- Janssens, K. et al. (2004) *Confocal microscopic X-ray fluorescence at the HASYLAB microfocuss beamline: characteristics and possibilities*. Spectrochimica Acta Part B, Vol.59, pp. 1637-1645
- Janssens, K. (2005) *Comprehensive Analytical Chemistry XLII, Non-destructive micro analysis of cultural heritage materials*. Article in Press, pp. 129 – 226, Elsevier B. V., Amsterdam
- Jeol, Ltd. (2009) *Scanning Electron Microscope A to Z*. pp. 27-28
- Kanngieger, B. et al. (2005) *Three-dimensional micro-XRF investigations of paint layers with a tabletop setup*. Spectrochimica Acta Part B, Vol. 60, pp. 41-47
- Kato, Y. and Nakamura, K. (2003) *Origin and global tectonic significance of Early Archaean cherts from the Marble Bar greenstone belt, Pilbara Craton, Western Australia*. Precambrian Research, Vol. 125, pp. 191-243
- Kranendonk, Van M. J. et al. (2003) *Geological and trace element evidence for a marine sedimentary environment of deposition and biogenicity of 3.45 Ga stromatolitic carbonates in the Pilbara Craton, and support for a reducing Archaean ocean*. Geobiology, Vol. 1, pp. 91-108
- Kumakhov, M.A. and Komarov, F.F. (1990) *Multiple reflection from surface X-ray optics*. Physics reports, Vol. 191, Iss. 5, pp. 289-350

- Langhoff, N. and Simionovici, A. (2006) *Handbook of Practical X-ray Fluorescence Analysis*, 1st ed. Springer, Heidelberg, pp. 33-37
- Lalou, C. et al. (1983) *Hydrothermal manganese oxide deposits from Galapagos mounds, DSDP Leg 70, hole 509B and "Alvin" dives 729 and 721*. Earth and Planetary Science Letters, Vol. 63, pp. 63-75
- Leistel, J.M. et al. (1998) *Chert in the Iberian Pyrite Belt*. Mineralium Deposita, Vol. 33, pp. 59-81
- Malzer, W. and Kanngießner, B. (2005) *A model for the confocal volume of 3D micro X-ray fluorescence spectrometer*. Spectrochimica Acta Part B, Vol.60, pp. 1334 – 1341
- Miller, T. C. et al. (2005) *Characterization of small particles by micro X-ray fluorescence*. Spectrochimica acta. B, atomic spectroscopy, Vol. 60, Iss. 11, pp. 1458-1467
- Molloy, J. L. and Sieber, J. R. (2008) *Classification of microheterogeneity in solid samples using μ XRF*. Analytical and Bioanalytical Chemistry, Vol. 392, pp. 995-1001
- Moorby, S.A. (1983) *The geochemistry of transitional sediments recovered from the Galapagos Hydrothermal Mounds Field during DSDP Leg 70 implications for mounds formation*. Earth and Planetary Science Letters, Vol. 62, pp. 367-376
- Morris, R.C. (1993) *Genetic modelling for banded iron-formation of the Hamersley Group, Pilbara Craton, Western Australia*. Precambrian Research, Vol. 60, pp. 243-286
- Papadopoulou, D.N. et al. (2006) *Development and optimisation of a portable micro-XRF method for in situ multi-element analysis of ancient ceramics*. Talanta, Vol. 68, Iss. 5, pp. 1692-1699
- Papineau, D. (2010) *Mineral Environments on the Earliest Earth*. Elements, Vol. 6, pp. 25-30
- Qin, L. and Humayun, M. (2008) *The Fe/Mn ratio in MORB and OIB determined by ICP-MS*. Geochimica et Cosmochimica Acta, Vol. 72, pp. 1660–1677
- Röntgen, W.C (1896) *On a new kind of rays*. Journal of the Franklin Institute, Vol. 141, Iss. 3, pp. 183 - 191
- Rouchon, V. and Orberger, B. (2008) *Origin and mechanisms of K–Si-metasomatism of ca. 3.4–3.3 Ga volcanoclastic deposits and implications for Archean seawater evolution: Examples from cherts of Kittys Gap (Pilbara craton, Australia) and Msauli (Barberton Greenstone Belt, South Africa)*. Precambrian Research, Vol. 165, pp. 169–189
- Schopf, J.W. et al. (2002) *Laser-Raman imagery of Earth's earliest fossils*. Nature, Vol. 416, pp. 73-76
- Sunder Raju, P.V. (2009) *Petrography and geochemical behavior of trace element, REE and precious metal signatures of sulphidic banded iron formations from the Chikkasiddavanahalli area, Chitradurga schist belt, India*. Journal of Asian Earth Sciences, Vol. 34, pp. 663–673
- Tsuji, K. et al. (2008) *X-ray Spectrometry*. Analytical Chemistry, Vol. 80, pp. 4421–4454
- Usui, A. et al. (1997) *Distribution and composition of marine hydrogenetic and hydrothermal manganese deposits in the northwest Pacific*. Geological Society, London, Special Publications, Vol. 119, pp. 177-198
- Vincze, L. et al. (2004) *Three-dimensional trace element analysis by confocal X-ray microfluorescence imaging*. Analytical Chemistry, Vol. 76, pp. 6786–6791.

- Vries, de S. T. (2004) *Early Archaean sedimentary basins: depositional environment and hydrothermal systems* Examples from the Barberton and Coppin Gap Greenstone Belts. *Geologica Ultraiectina*, Vol. 244, pp. 98
- Westall, F. et al. (2006) *The 3.466 Ga "Kitty's Gap Chert," an early Archaean microbial ecosystem*. *GSA Special papers*. Vol. 405. pp. 105-131
- Xiao-Yan et al. (2007) *Investigation of a Tabletop Confocal Micro X-Ray Fluorescence Setup*. *Chinese Phys. Lett.* Vol. 24, pp. 3368-3370

Appendix 1: Standard deviations in measurements of international standards under variable conditions

Abnormal high standard deviations are marked in red. Data in the first two 30 and 20 keV columns are those measured against the 30 keV WAX reference spectrum. The other data (50, 40, 30, and 20 keV columns) are measured against the 50 keV WAX reference spectrum. The elements marked in *italic* have concentrations <1%. Graphs are displayed at the end of the standard deviation tables.

The standard-deviation formula used is:

$$\sqrt{\frac{\sum (x - \bar{x})^2}{n}} \quad (n=6)$$

This is the STDEVP function of Microsoft Excel 2007. This formula assumes that the arguments (data) used in the calculation represent the entire population.

3.2 us, 100uA

Standard ID	JB-1b	Std. Dev. in %					
		30keV	20keV	50keV	40keV	30keV	20keV
Na ₂ O		9.39	7.50	8.16	10.61	12.76	10.32
MgO		3.69	3.93	2.54	1.48	2.08	2.22
Al ₂ O ₃		0.69	1.17	1.17	0.60	1.48	0.47
SiO ₂		0.79	0.36	0.92	0.51	0.81	0.64
<i>P₂O₅</i>		<i>7.85</i>	<i>2.75</i>	<i>3.26</i>	<i>4.89</i>	<i>5.64</i>	<i>5.54</i>
K ₂ O		1.64	1.90	1.08	1.13	1.35	2.12
CaO		1.24	0.84	0.71	1.04	1.96	1.32
TiO ₂		1.68	2.07	1.70	1.17	2.56	4.88
<i>MnO</i>		<i>4.94</i>	<i>4.47</i>	<i>4.77</i>	<i>1.94</i>	<i>5.56</i>	<i>4.08</i>
Fe ₂ O ₃		1.19	0.94	1.51	1.30	1.80	1.61

6.4 us, 100uA

Standard ID	JB-1b	Std. Dev. in %					
		30keV	20keV	50keV	40keV	30keV	20keV
Na ₂ O		3.56	8.04	3.56	10.88	4.89	3.96
MgO		1.62	1.63	2.57	2.55	2.63	2.02
Al ₂ O ₃		0.91	0.56	0.90	0.95	1.27	1.65
SiO ₂		0.42	0.81	0.61	1.06	0.52	0.51
<i>P₂O₅</i>		<i>2.70</i>	<i>4.16</i>	<i>5.01</i>	<i>7.29</i>	<i>3.68</i>	<i>5.55</i>
K ₂ O		1.62	3.25	1.62	1.95	1.43	1.96
CaO		1.16	1.04	0.78	2.28	0.84	1.31
TiO ₂		1.06	2.03	1.44	3.04	0.99	3.43
<i>MnO</i>		<i>4.00</i>	<i>4.25</i>	<i>3.78</i>	<i>4.54</i>	<i>2.67</i>	<i>5.23</i>
Fe ₂ O ₃		0.70	0.90	0.91	2.59	0.91	1.40

3.2 us, high uA

Standard ID	JB-1b	Std. Dev. in %					
		30keV	20keV	50keV	40keV	30keV	20keV
Na ₂ O		4.01	3.30	4.48	6.46	3.41	3.21
MgO		1.02	1.07	0.68	0.55	0.83	0.95
Al ₂ O ₃		0.58	0.30	0.52	0.70	0.38	0.41
SiO ₂		0.21	0.18	0.11	0.28	0.26	0.18
P ₂ O ₅		2.09	1.95	1.05	1.34	0.68	2.30
K ₂ O		0.49	0.79	0.46	0.47	0.71	1.29
CaO		0.54	0.52	0.68	0.62	0.44	0.52
TiO ₂		1.62	1.36	1.90	1.45	1.28	1.21
MnO		2.57	0.00	3.04	1.94	2.05	2.35
Fe ₂ O ₃		0.65	0.47	0.71	0.48	0.44	0.60

6.4 us, high uA

Standard ID	JB-1b	Std. Dev. in %					
		30keV	20keV	50keV	40keV	30keV	20keV
Na ₂ O		6.95	2.55	5.99	10.41	6.80	3.35
MgO		0.64	1.65	2.17	1.90	1.36	1.19
Al ₂ O ₃		0.39	0.68	0.65	1.07	0.30	0.20
SiO ₂		0.44	0.27	0.72	0.98	0.45	0.27
P ₂ O ₅		2.52	2.13	2.70	2.93	2.07	1.99
K ₂ O		0.98	1.29	0.88	1.57	1.29	0.39
CaO		1.06	0.38	0.72	1.58	0.77	0.74
TiO ₂		2.05	1.71	1.50	2.39	1.21	2.59
MnO		2.17	4.34	2.57	2.09	4.30	2.31
Fe ₂ O ₃		1.25	0.44	1.15	1.89	1.35	0.76

3.2 us, 100uA

Standard ID	GS-N	Std. Dev. in %					
		30keV	20keV	50keV	40keV	30keV	20keV
Na ₂ O		4.78	6.74	4.37	5.75	9.57	3.43
MgO		5.55	4.51	5.03	3.98	3.70	5.36
Al ₂ O ₃		0.77	0.44	1.24	0.97	1.67	1.46
SiO ₂		0.42	0.48	0.56	0.43	0.75	0.64
P ₂ O ₅		4.54	4.58	6.17	7.32	10.40	4.41
K ₂ O		1.05	1.74	1.48	1.66	1.19	0.99
CaO		2.26	1.31	2.25	2.00	1.88	1.33
TiO ₂		2.54	3.72	2.61	1.95	1.78	2.73
MnO		5.45	7.69	5.20	6.62	8.25	7.07
Fe ₂ O ₃		0.91	1.51	0.84	1.78	1.39	2.12

6.4 us, 100uA

Standard ID	GS-N	Std. Dev. in %					
		30keV	20keV	50keV	40keV	30keV	20keV
Na ₂ O		5.62	5.99	14.86	14.05	9.60	4.32
MgO		2.38	4.58	3.86	8.40	6.48	4.73
Al ₂ O ₃		0.38	1.25	1.19	0.98	0.89	0.91
SiO ₂		0.49	0.61	1.64	1.75	0.87	0.57
P ₂ O ₅		6.51	7.18	10.30	7.37	5.53	5.98
K ₂ O		0.86	1.39	2.92	3.04	1.31	2.15
CaO		1.82	1.52	2.86	3.37	2.18	1.80
TiO ₂		1.23	2.82	4.09	4.45	3.50	1.37
MnO		8.25	7.07	0.00	5.45	7.07	5.45
Fe ₂ O ₃		1.07	2.10	2.26	4.17	2.99	1.85

3.2 us, high uA

Standard ID	GS-N	Std. Dev. in %					
		30keV	20keV	50keV	40keV	30keV	20keV
Na ₂ O		2.94	3.04	4.50	1.91	1.02	1.33
MgO		0.97	1.01	1.50	2.81	1.30	1.26
Al ₂ O ₃		0.75	0.53	0.58	0.28	0.27	0.57
SiO ₂		0.24	0.28	0.25	0.31	0.08	0.25
P ₂ O ₅		2.82	2.02	2.85	3.67	2.59	2.57
K ₂ O		0.36	0.47	0.40	0.47	0.43	0.53
CaO		0.64	1.48	0.51	0.96	0.77	0.67
TiO ₂		0.96	0.84	0.79	1.21	1.49	1.23
MnO		7.44	6.39	0.00	0.00	6.04	0.00
Fe ₂ O ₃		0.76	0.57	1.00	0.73	0.42	0.78

6.4 us, high uA

Standard ID	GS-N	Std. Dev. in %					
		30keV	20keV	50keV	40keV	30keV	20keV
Na ₂ O		5.78	3.81	6.28	16.26	9.41	1.39
MgO		2.27	0.89	3.35	6.80	2.97	1.74
Al ₂ O ₃		0.68	0.33	0.32	0.82	0.74	0.57
SiO ₂		0.51	0.27	0.67	1.56	0.84	0.19
P ₂ O ₅		2.75	2.25	4.11	5.87	5.35	1.89
K ₂ O		1.01	0.75	1.46	3.15	1.96	0.61
CaO		1.06	0.82	0.86	4.10	2.09	1.45
TiO ₂		1.41	0.88	1.89	4.98	3.36	2.09
MnO		0.00	6.39	5.45	5.88	6.04	0.00
Fe ₂ O ₃		1.67	1.49	1.29	4.22	2.67	1.14

3.2 us, 100uA

Standard ID	FER-4	Std. Dev. in %				
		30keV	20keV	50keV	40keV	30keV
<i>Na₂O</i>		21.25	15.04	28.58	27.76	32.25
MgO		5.60	4.23	13.13	7.44	10.91
Al ₂ O ₃		6.96	4.60	2.97	3.97	7.38
SiO ₂		1.37	0.89	0.72	1.20	1.28
<i>P₂O₅</i>		8.72	8.60	8.70	11.26	11.15
<i>K₂O</i>		2.44	4.56	3.39	1.71	4.55
CaO		1.97	0.61	1.65	1.89	1.92
<i>TiO₂</i>		0.00	9.13	4.88	7.50	9.75
<i>MnO</i>		2.62	4.24	2.28	2.28	1.85
Fe ₂ O ₃		1.09	0.64	2.34	1.96	2.04

6.4 us, 100uA

Standard ID	FER-4	Std. Dev. in %					
		30keV	20keV	50keV	40keV	30keV	20keV
<i>Na₂O</i>		11.34	14.44	12.55	9.49	6.79	6.59
MgO		2.46	9.13	4.09	6.43	2.02	4.29
Al ₂ O ₃		6.29	3.41	4.30	5.42	10.43	3.82
SiO ₂		0.99	1.11	1.04	0.78	0.88	0.77
<i>P₂O₅</i>		4.20	5.88	5.44	4.17	8.61	9.20
<i>K₂O</i>		5.77	3.44	4.22	4.16	6.75	6.86
CaO		1.46	2.24	1.79	1.56	1.92	1.23
<i>TiO₂</i>		10.21	10.10	8.41	5.44	10.16	12.07
<i>MnO</i>		3.44	3.39	2.89	4.08	1.85	2.44
Fe ₂ O ₃		0.41	0.55	2.41	0.87	1.72	1.15

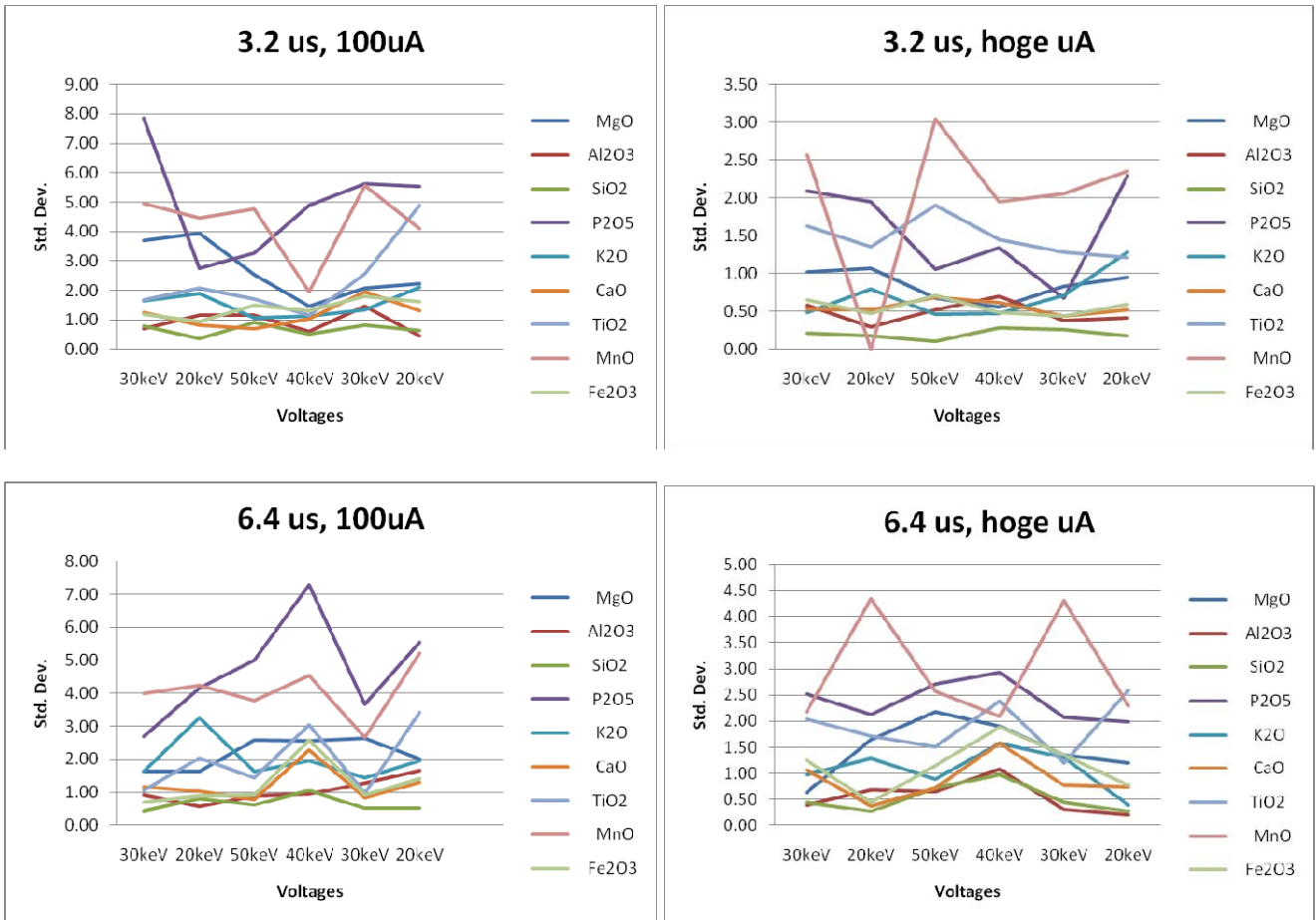
3.2 us, high uA

Standard ID	FER-4	Std. Dev. in %					
		30keV	20keV	50keV	40keV	30keV	20keV
<i>Na₂O</i>		9.19	18.99	13.52	34.51	17.60	13.33
MgO		2.41	3.38	3.79	2.30	4.53	2.48
Al ₂ O ₃		6.75	2.97	1.35	3.34	7.45	1.33
SiO ₂		0.65	0.70	0.64	0.33	0.46	0.59
<i>P₂O₅</i>		5.54	5.53	5.05	5.94	5.05	4.68
<i>K₂O</i>		3.78	3.99	3.89	2.75	4.45	2.97
CaO		2.66	1.77	1.40	1.59	2.14	1.67
<i>TiO₂</i>		4.07	4.07	5.05	0.00	4.07	6.99
<i>MnO</i>		2.22	0.00	1.76	1.76	2.28	0.00
Fe ₂ O ₃		1.14	0.84	0.84	0.68	1.11	0.89

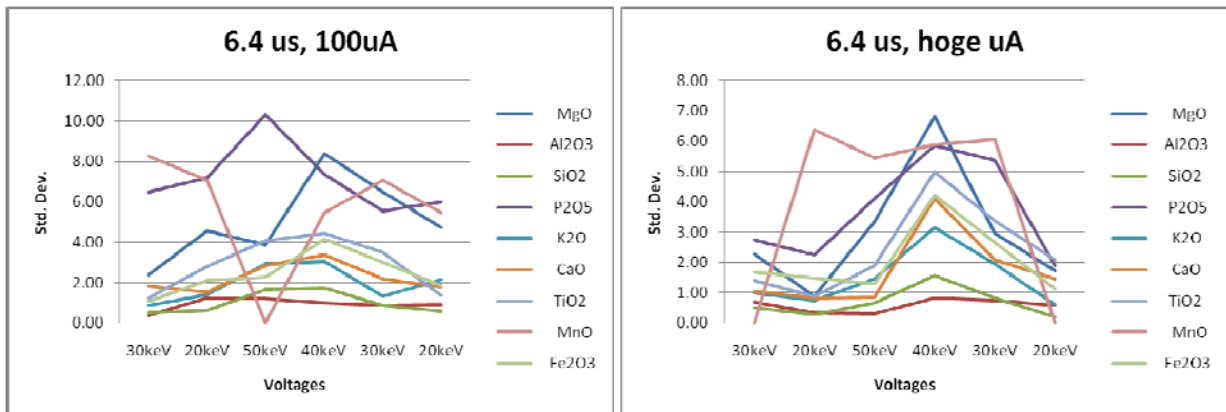
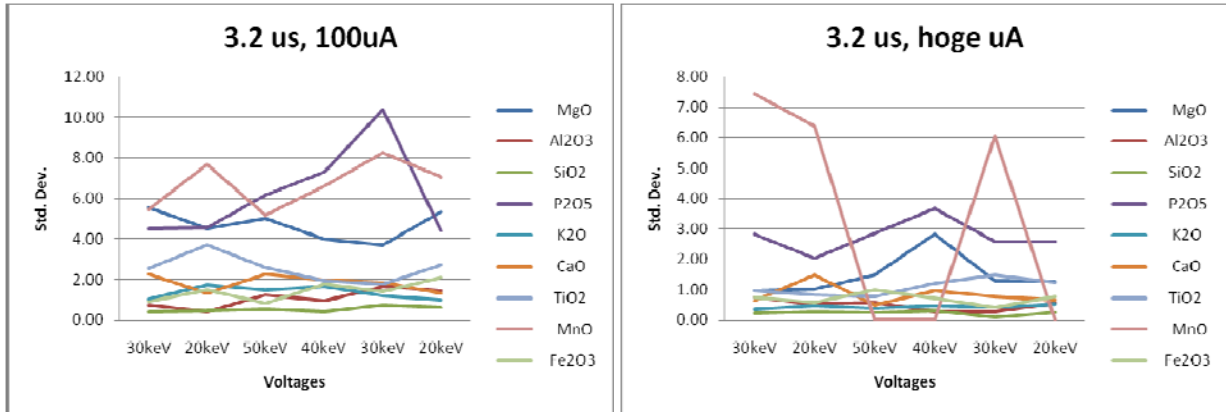
6.4 us, high uA

Standard ID	FER-4	Std. Dev. in %					
		30keV	20keV	50keV	40keV	30keV	20keV
Na ₂ O		5.78	6.30	18.36	14.53	5.65	2.92
MgO		2.77	2.85	7.09	6.19	2.45	4.58
Al ₂ O ₃		7.55	2.44	2.62	3.20	3.35	4.13
SiO ₂		1.13	0.64	1.18	0.84	0.48	0.99
P ₂ O ₅		1.16	3.37	8.41	8.22	1.52	5.35
K ₂ O		2.44	1.88	4.35	2.08	3.01	3.12
CaO		1.92	1.88	1.94	1.60	1.32	1.95
TiO ₂		4.56	7.78	8.41	5.88	8.41	7.78
MnO		2.18	2.18	3.46	0.00	1.85	2.56
Fe ₂ O ₃		1.06	0.77	2.59	2.00	0.43	0.66

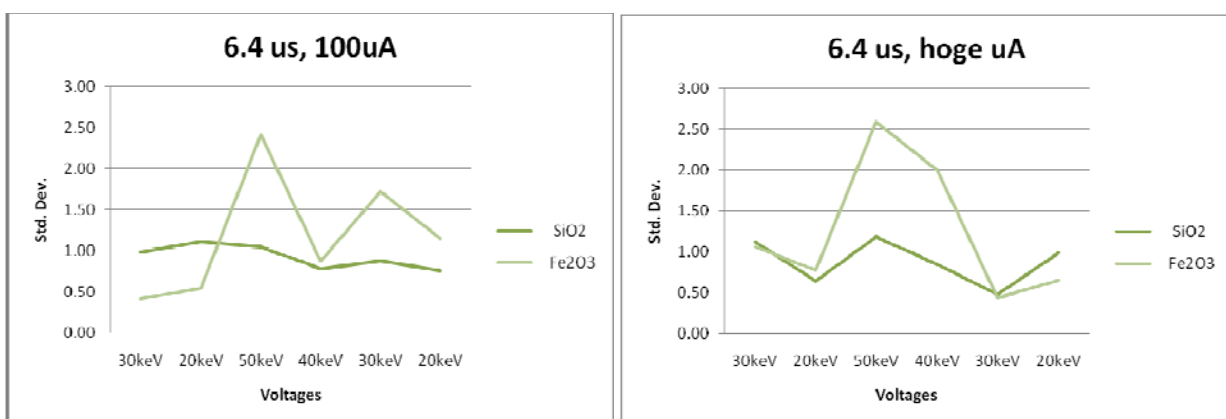
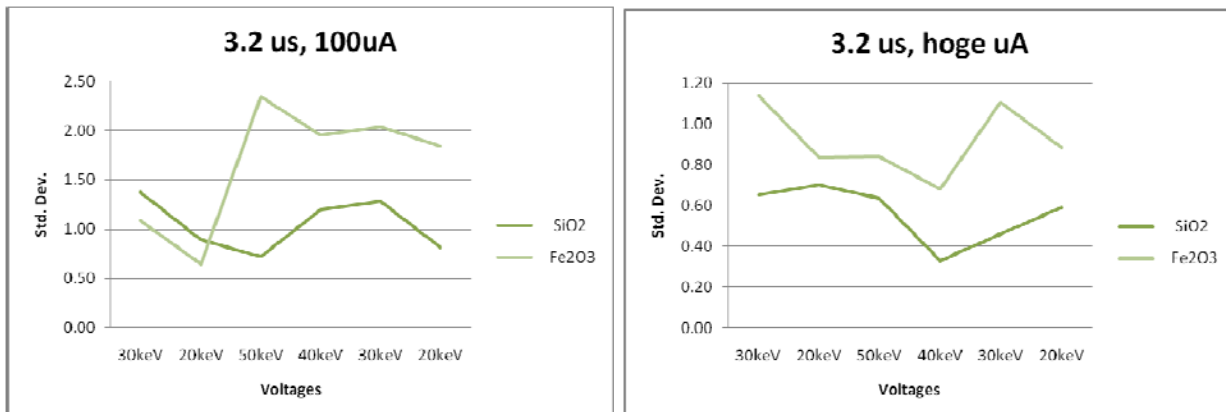
Basalt



Granite



Fe-rock



Appendix 2: Results of measurements on international standards

For each test, concentrations and accuracy data are reported in separate tables. If errors were up to 6%, the results are displayed in **bold** in the accuracy tables. Accepted concentrations in the standards were normalized to 100%. Data reported in the first 30 and 20-keV columns were measured against the 30 keV WAX reference spectrum. The other keV data (50, 40, 30, and 20 keV columns) were measured against the 50 keV WAX reference spectrum. The elements marked in *italic* have concentrations <1%. n=6

3.2 μ s, 100 μ A

Standard ID	Accepted	Measured					
	JB-1b	30keV	20keV	50keV	40keV	30keV	20keV
SiO ₂ %	51.11	47.97	49.22	46.58	47.11	47.80	49.02
TiO ₂ %	1.26	0.95	0.90	1.01	0.99	0.94	0.91
Al ₂ O ₃ %	14.38	13.32	13.83	13.06	13.09	13.40	13.65
MnO %	0.147	<i>0.18</i>	<i>0.17</i>	<i>0.19</i>	<i>0.19</i>	<i>0.18</i>	<i>0.17</i>
MgO %	8.14	9.85	10.09	9.92	9.86	10.11	10.18
CaO %	9.6	6.81	6.58	7.25	7.16	6.80	6.59
Na ₂ O %	2.63	5.61	5.16	5.7	5.23	5.48	5.36
K ₂ O %	1.32	0.96	0.93	0.99	0.98	0.94	0.94
P ₂ O ₅ %	0.256	<i>0.72</i>	<i>0.77</i>	<i>0.72</i>	<i>0.73</i>	<i>0.74</i>	<i>0.79</i>
Fe ₂ O ₃ t %	9.06	12.09	10.84	13.11	13.14	12.08	10.87

Accuracy
(error = 100%- value given below)

	30keV	20keV	50keV	40keV	30keV	20keV
SiO ₂ %	93.86	96.30	91.14	92.17	93.51	95.90
TiO ₂ %	75.66	71.56	80.16	78.57	74.74	72.35
Al ₂ O ₃ %	92.61	96.14	90.82	90.99	93.20	94.92
MnO %	<i>123.58</i>	<i>113.38</i>	<i>129.25</i>	<i>130.39</i>	<i>122.45</i>	<i>114.51</i>
MgO %	121.01	123.98	121.87	121.15	124.22	125.06
CaO %	70.95	68.58	75.52	74.55	70.87	68.63
Na ₂ O %	213.43	196.07	216.73	198.86	208.43	203.87
K ₂ O %	72.60	70.58	75.00	73.99	70.83	70.83
P ₂ O ₅ %	<i>282.55</i>	<i>300.13</i>	<i>281.25</i>	<i>283.20</i>	<i>289.71</i>	<i>306.64</i>
Fe ₂ O ₃ t %	133.44	119.59	144.70	145.03	133.37	120.00

6.4 us, 100 uA

Standard ID	Accepted	Measured					
	JB-1b	30keV	20keV	50keV	40keV	30keV	20keV
SiO ₂ %	51.11	46.65	48.16	44.74	45.1	46.38	48.23
TiO ₂ %	1.26	0.91	0.88	0.96	0.92	0.91	0.89
Al ₂ O ₃ %	14.38	13.91	14.35	13.56	13.66	13.84	14.33
MnO %	0.147	0.17	0.16	0.18	0.18	0.18	0.17
MgO %	8.14	10.19	10.25	10.38	10.33	10.34	10.04
CaO %	9.6	6.83	6.72	7.13	7.05	6.84	6.79
Na ₂ O %	2.63	6.67	5.70	7.61	7.37	6.66	5.65
K ₂ O %	1.32	0.97	0.97	1.01	0.95	0.97	0.97
P ₂ O ₅ %	0.256	0.80	0.80	0.75	0.77	0.79	0.80
Fe ₂ O ₃ t %	9.06	11.39	10.50	12.16	12.12	11.56	10.62

Accuracy
(error = 100%- value given below)

	30keV	20keV	50keV	40keV	30keV	20keV
SiO ₂ %	91.28	94.22	87.54	88.24	90.74	94.36
TiO ₂ %	71.83	70.11	76.19	73.02	72.09	70.63
Al ₂ O ₃ %	96.71	99.78	94.30	94.99	96.27	99.64
MnO %	116.78	109.98	122.45	122.45	120.18	116.78
MgO %	125.12	125.90	127.52	126.90	127.07	123.28
CaO %	71.09	69.98	74.27	73.44	71.25	70.69
Na ₂ O %	253.61	216.54	289.35	280.23	253.30	214.83
K ₂ O %	73.36	73.23	76.52	71.97	73.11	73.11
P ₂ O ₅ %	312.50	310.55	292.97	300.78	309.24	311.20
Fe ₂ O ₃ t %	125.68	115.89	134.22	133.77	127.59	117.20

3.2 us, high uA

Standard ID	Accepted	Measured					
	JB-1b	30keV	20keV	50keV	40keV	30keV	20keV
SiO ₂ %	51.11	48.65	49.82	47.32	47.56	48.71	49.86
TiO ₂ %	1.26	0.97	0.93	1.05	1.01	0.97	0.91
Al ₂ O ₃ %	14.38	13.42	13.75	13.12	13.16	13.41	13.71
MnO %	0.147	0.18	0.16	0.19	0.19	0.18	0.16
MgO %	8.14	9.80	9.96	9.5	9.64	9.75	9.93
CaO %	9.6	7.00	6.76	7.46	7.32	7.03	6.80
Na ₂ O %	2.63	4.18	4.25	4.25	4.23	4.14	4.22
K ₂ O %	1.32	0.96	0.94	1.03	1.00	0.96	0.94
P ₂ O ₅ %	0.256	0.70	0.70	0.73	0.70	0.69	0.71
Fe ₂ O ₃ t %	9.06	12.61	11.19	13.84	13.66	12.63	11.23

Accuracy
(error = 100%- value given below)

	30keV	20keV	50keV	40keV	30keV	20keV
SiO ₂ %	95.18	97.48	92.58	93.04	95.31	97.56
TiO ₂ %	76.85	73.41	83.33	80.03	77.25	72.49
Al ₂ O ₃ %	93.31	95.63	91.24	91.49	93.24	95.34
MnO %	124.72	108.84	129.25	130.39	123.58	107.71
MgO %	120.39	122.40	116.71	118.47	119.72	121.99
CaO %	72.95	70.38	77.71	76.25	73.19	70.80
Na ₂ O %	159.00	161.72	161.60	160.84	157.48	160.27
K ₂ O %	72.98	71.46	78.03	76.01	72.85	71.34
P ₂ O ₅ %	272.79	274.74	285.16	274.74	270.83	277.34
Fe ₂ O ₃ t %	139.16	123.55	152.76	150.75	139.40	123.93

6.4 us, high uA

Standard ID	Accepted	Measured					
	JB-1b	30keV	20keV	50keV	40keV	30keV	20keV
SiO ₂ %	51.11	46.89	48.07	45.49	45.67	46.58	48.02
TiO ₂ %	1.26	0.93	0.88	0.99	0.96	0.92	0.88
Al ₂ O ₃ %	14.38	13.98	14.24	13.63	13.74	13.94	14.26
MnO %	0.147	0.17	0.16	0.18	0.18	0.17	0.16
MgO %	8.14	10.26	10.41	10.01	10.15	10.27	10.35
CaO %	9.6	6.92	6.73	7.38	7.21	6.88	6.73
Na ₂ O %	2.63	5.91	5.80	6.31	6.2	6.38	5.82
K ₂ O %	1.32	0.96	0.94	1.02	1	0.96	0.95
P ₂ O ₅ %	0.256	0.74	0.80	0.72	0.72	0.77	0.79
Fe ₂ O ₃ t %	9.06	11.72	10.45	12.76	12.64	11.60	10.51

Accuracy
(error = 100%- value given below)

	30keV	20keV	50keV	40keV	30keV	20keV
SiO ₂ %	91.74	94.06	89.00	89.36	91.14	93.95
TiO ₂ %	73.41	69.44	78.57	76.19	72.75	70.11
Al ₂ O ₃ %	97.21	99.01	94.78	95.55	96.91	99.18
MnO %	116.78	107.71	122.45	122.45	117.91	109.98
MgO %	126.06	127.93	122.97	124.69	126.21	127.19
CaO %	72.05	70.07	76.88	75.10	71.67	70.10
Na ₂ O %	224.78	220.47	239.92	235.74	242.46	221.23
K ₂ O %	72.98	71.34	77.27	75.76	72.98	72.10
P ₂ O ₅ %	288.41	311.20	281.25	281.25	302.08	309.24
Fe ₂ O ₃ t %	129.30	115.36	140.84	139.51	128.04	115.97

3.2 us, 100 uA

Standard ID	Accepted	Measured					
	GS-N	30keV	20keV	50keV	40keV	30keV	20keV
SiO ₂ %	65.8	63.41	64.19	61.96	62.17	63.47	64.24
TiO ₂ %	0.68	0.59	0.56	0.62	0.59	0.60	0.56
Al ₂ O ₃ %	14.67	13.32	13.44	12.99	13.07	13.18	13.36
MnO %	0.06	0.07	0.07	0.07	0.20	0.07	0.07
MgO %	2.3	4.02	4.03	4.07	3.90	4.13	3.98
CaO %	2.5	1.88	1.82	2.00	1.98	1.88	1.82
Na ₂ O %	3.77	6.46	6.25	7.49	6.26	6.36	6.35
K ₂ O %	4.63	3.40	3.24	3.59	3.53	3.41	3.28
P ₂ O ₅ %	0.28	0.59	0.67	0.61	0.65	0.62	0.62
Fe ₂ O ₃ t %	3.75	5.09	4.53	5.43	6.46	5.09	4.52

Accuracy
(error = 100%- value given below)

	30keV	20keV	50keV	40keV	30keV	20keV
SiO ₂ %	96.36	97.55	94.16	94.48	96.46	97.63
TiO ₂ %	86.27	82.35	90.44	86.27	87.99	82.35
Al ₂ O ₃ %	90.80	91.64	88.55	89.08	89.82	91.05
MnO %	113.89	108.33	119.44	336.11	116.67	111.11
MgO %	174.71	175.36	176.88	169.35	179.64	173.12
CaO %	75.00	72.80	79.87	79.27	75.27	72.93
Na ₂ O %	171.22	165.83	198.63	165.96	168.57	168.39
K ₂ O %	73.40	70.01	77.43	76.21	73.58	70.88
P ₂ O ₅ %	210.12	239.88	216.07	231.55	222.02	222.62
Fe ₂ O ₃ t %	135.64	120.67	144.67	172.31	135.60	120.53

6.4 us, 100 uA

Standard ID	Accepted	Measured					
	GS-N	30keV	20keV	50keV	40keV	30keV	20keV
SiO ₂ %	65.8	61.41	62.91	59.73	60.30	61.89	63.13
TiO ₂ %	0.68	0.56	0.56	0.59	0.57	0.56	0.54
Al ₂ O ₃ %	14.67	13.88	13.87	13.57	13.64	13.80	13.93
MnO %	0.06	0.07	0.07	0.07	0.07	0.07	0.07
MgO %	2.3	4.34	4.26	4.85	4.46	4.25	4.22
CaO %	2.5	1.88	1.86	1.97	1.92	1.89	1.84
Na ₂ O %	3.77	7.77	6.86	8.73	8.56	7.37	6.69
K ₂ O %	4.63	3.42	3.34	3.59	3.55	3.43	3.34
P ₂ O ₅ %	0.28	0.68	0.71	0.62	0.66	0.67	0.72
Fe ₂ O ₃ t %	3.75	4.80	4.38	5.08	5.09	4.87	4.34

Accuracy
(error = 100%- value given below)

	30keV	20keV	50keV	40keV	30keV	20keV
SiO ₂ %	93.32	95.61	90.78	91.65	94.06	95.94
TiO ₂ %	82.11	82.11	87.25	84.07	82.84	79.90
Al ₂ O ₃ %	94.63	94.55	92.48	92.94	94.09	94.92
MnO %	116.67	111.11	116.67	113.89	111.11	113.89
MgO %	188.77	185.07	211.01	193.84	184.64	183.33
CaO %	75.00	74.20	78.80	76.73	75.47	73.47
Na ₂ O %	206.06	181.83	231.61	226.92	195.45	177.32
K ₂ O %	73.76	72.03	77.47	76.60	73.97	72.17
P ₂ O ₅ %	242.26	253.57	222.62	235.71	240.48	256.55
Fe ₂ O ₃ t %	128.09	116.80	135.33	135.69	129.96	115.64

3.2 us, high uA

Standard ID	Accepted	Measured					
	GS-N	30keV	20keV	50keV	40keV	30keV	20keV
SiO ₂ %	65.8	64.20	65.09	63.38	63.72	64.39	65.12
TiO ₂ %	0.68	0.60	0.56	0.64	0.62	0.60	0.56
Al ₂ O ₃ %	14.67	13.33	13.49	13.13	13.19	13.31	13.45
MnO %	0.06	0.06	0.06	0.07	0.07	0.06	0.06
MgO %	2.3	3.77	3.77	3.81	3.79	3.82	3.79
CaO %	2.5	1.94	1.86	2.08	2.03	1.93	1.85
Na ₂ O %	3.77	5.51	5.32	5.67	5.45	5.40	5.40
K ₂ O %	4.63	3.50	3.38	3.71	3.67	3.50	3.36
P ₂ O ₅ %	0.28	0.61	0.62	0.64	0.62	0.59	0.61
Fe ₂ O ₃ t %	3.75	5.29	4.67	5.69	5.65	5.21	4.60

Accuracy
(error = 100%- value given below)

	30keV	20keV	50keV	40keV	30keV	20keV
SiO ₂ %	97.57	98.92	96.32	96.84	97.85	98.97
TiO ₂ %	88.24	82.84	93.38	90.69	88.48	82.11
Al ₂ O ₃ %	90.88	91.95	89.47	89.93	90.75	91.68
MnO %	105.56	97.22	116.67	116.67	102.78	100.00
MgO %	163.70	163.99	165.80	164.57	165.87	164.57
CaO %	77.47	74.27	83.27	81.27	77.07	74.13
Na ₂ O %	146.07	140.98	150.31	144.61	143.28	143.10
K ₂ O %	75.67	72.93	80.06	79.16	75.52	72.61
P ₂ O ₅ %	216.07	220.24	228.57	220.83	210.71	218.45
Fe ₂ O ₃ t %	141.07	124.49	151.64	150.71	138.89	122.71

6.4 us, high uA

Standard ID	Accepted	Measured					
	GS-N	30keV	20keV	50keV	40keV	30keV	20keV
SiO ₂ %	65.8	62.67	62.92	61.20	60.94	61.87	62.77
TiO ₂ %	0.68	0.58	0.53	0.61	0.58	0.57	0.54
Al ₂ O ₃ %	14.67	13.93	14.01	13.72	13.66	13.82	13.98
MnO %	0.06	0.06	0.06	0.07	0.09	0.06	0.06
MgO %	2.3	4.08	4.23	4.13	4.17	4.34	4.23
CaO %	2.5	1.95	1.83	2.07	2.00	1.91	1.84
Na ₂ O %	3.77	6.41	6.84	7.32	7.26	7.29	6.99
K ₂ O %	4.63	3.52	3.35	3.70	3.61	3.45	3.33
P ₂ O ₅ %	0.28	0.63	0.70	0.62	0.63	0.67	0.71
Fe ₂ O ₃ t %	3.75	4.97	4.34	5.36	5.85	4.83	4.37

Accuracy
(error = 100%- value given below)

	30keV	20keV	50keV	40keV	30keV	20keV
SiO ₂ %	95.24	95.63	93.01	92.62	94.03	95.39
TiO ₂ %	85.29	78.43	89.71	85.54	83.82	78.68
Al ₂ O ₃ %	94.92	95.51	93.54	93.12	94.17	95.26
MnO %	100.00	97.22	113.89	152.78	102.78	100.00
MgO %	177.39	183.77	179.57	181.23	188.77	183.70
CaO %	77.80	73.00	82.87	80.07	76.27	73.67
Na ₂ O %	170.03	181.52	194.25	192.57	193.32	185.46
K ₂ O %	76.10	72.25	79.88	77.97	74.48	71.96
P ₂ O ₅ %	225.00	249.40	222.62	225.00	238.69	254.17
Fe ₂ O ₃ t %	132.49	115.73	142.89	156.09	128.89	116.40

3.2 us, 100 uA

Standard ID	Accepted	Measured					
	FER-4	30keV	20keV	50keV	40keV	30keV	20keV
SiO ₂ %	50.07	44.41	47.88	44.87	46.15	48.62	51.75
TiO ₂ %	0.07	0.09	0.10	0.10	0.09	0.10	0.10
Al ₂ O ₃ %	1.70	2.42	2.55	2.35	2.40	2.57	2.73
MnO %	0.19	0.22	0.21	0.21	0.21	0.20	0.20
MgO %	1.41	2.99	3.13	2.86	3.14	3.19	3.25
CaO %	2.23	1.52	1.56	1.69	1.66	1.67	1.74
Na ₂ O %	0.05	2.48	2.43	3.25	3.02	2.55	2.44
K ₂ O %	0.29	0.19	0.21	0.23	0.22	0.22	0.25
P ₂ O ₅ %	0.13	0.37	0.41	0.37	0.38	0.40	0.46
Fe ₂ O ₃ t %	39.92	39.73	35.96	38.51	37.16	34.91	31.52

Accuracy
(error = 100%- value given below)

	30keV	20keV	50keV	40keV	30keV	20keV
SiO ₂ %	88.69	95.62	89.60	92.16	97.11	103.36
TiO ₂ %	128.57	140.48	138.10	130.95	138.10	147.62
Al ₂ O ₃ %	142.55	150.10	137.94	141.37	150.88	160.29
MnO %	115.79	111.40	108.77	108.77	106.14	105.26
MgO %	211.94	221.87	202.72	222.46	226.12	230.14
CaO %	68.16	69.81	75.71	74.59	74.74	78.10
Na ₂ O %	4960.00	4853.33	6503.33	6030.00	5096.67	4870.00
K ₂ O %	66.67	71.26	77.59	75.29	75.86	84.48
P ₂ O ₅ %	282.05	312.82	287.18	293.59	305.13	350.00
Fe ₂ O ₃ t %	99.53	90.08	96.46	93.09	87.45	78.95

6.4 us, 100 uA

Standard ID	Accepted	Measured					
	FER-4	30keV	20keV	50keV	40keV	30keV	20keV
SiO ₂ %	50.07	44.40	47.90	43.07	45.14	47.91	51.54
TiO ₂ %	0.07	0.08	0.09	0.08	0.09	0.09	0.10
Al ₂ O ₃ %	1.70	2.56	2.60	2.71	2.66	2.86	2.84
MnO %	0.19	0.22	0.23	0.20	0.20	0.20	0.21
MgO %	1.41	3.14	3.03	4.02	3.57	3.46	3.48
CaO %	2.23	1.55	1.63	1.67	1.68	1.76	1.86
Na ₂ O %	0.05	3.60	2.41	6.88	5.31	3.75	2.43
K ₂ O %	0.29	0.20	0.22	0.22	0.23	0.24	0.26
P ₂ O ₅ %	0.13	0.40	0.43	0.50	0.47	0.45	0.48
Fe ₂ O ₃ t %	39.92	38.27	35.89	35.08	35.07	33.69	31.23

Accuracy
(error = 100%- value given below)

	30keV	20keV	50keV	40keV	30keV	20keV
SiO ₂ %	88.67	95.66	86.02	90.16	95.69	102.94
TiO ₂ %	114.29	133.33	116.67	123.81	126.19	147.62
Al ₂ O ₃ %	150.69	152.84	159.51	156.27	168.24	167.06
MnO %	114.04	118.42	105.26	105.26	106.14	107.89
MgO %	222.58	215.13	285.11	253.31	245.27	246.81
CaO %	69.58	72.94	74.74	75.49	79.00	83.26
Na ₂ O %	7203.33	4823.33	13756.67	10626.67	7506.67	4863.33
K ₂ O %	68.97	74.71	77.01	78.16	81.61	89.08
P ₂ O ₅ %	306.41	326.92	380.77	360.26	348.72	366.67
Fe ₂ O ₃ t %	95.86	89.91	87.87	87.85	84.40	78.23

3.2 us, high uA

Standard ID	Accepted	Measured					
	FER-4	30keV	20keV	50keV	40keV	30keV	20keV
SiO ₂ %	50.07	45.04	48.35	45.22	46.97	49.33	52.33
TiO ₂ %	0.07	0.09	0.09	0.09	0.09	0.09	0.10
Al ₂ O ₃ %	1.70	2.36	2.40	2.31	2.41	2.55	2.58
MnO %	0.19	0.23	0.22	0.21	0.21	0.21	0.20
MgO %	1.41	2.51	2.62	2.51	2.52	2.67	2.87
CaO %	2.23	1.55	1.60	1.72	1.69	1.73	1.78
Na ₂ O %	0.05	0.90	0.95	1.02	1.09	1.07	0.95
K ₂ O %	0.29	0.18	0.19	0.21	0.21	0.22	0.23
P ₂ O ₅ %	0.13	0.31	0.33	0.34	0.33	0.34	0.37
Fe ₂ O ₃ t %	39.92	41.26	37.68	40.80	38.89	36.22	33.01

Accuracy
(error = 100%- value given below)

	30keV	20keV	50keV	40keV	30keV	20keV
SiO ₂ %	89.95	96.57	90.31	93.82	98.53	104.51
TiO ₂ %	130.95	130.95	133.33	128.57	130.95	140.48
Al ₂ O ₃ %	138.92	140.88	135.88	141.76	150.10	151.86
MnO %	118.42	115.79	111.40	111.40	108.77	105.26
MgO %	178.01	185.58	178.01	178.49	189.13	203.55
CaO %	69.28	71.75	77.20	75.93	77.35	79.97
Na ₂ O %	1796.67	1906.67	2030.00	2183.33	2146.67	1900.00
K ₂ O %	62.64	64.37	72.41	72.41	74.14	79.89
P ₂ O ₅ %	235.90	253.85	258.97	252.56	258.97	280.77
Fe ₂ O ₃ t %	103.36	94.38	102.20	97.42	90.73	82.69

6.4 us, high uA

Standard ID	Accepted	Measured					
	FER-4	30keV	20keV	50keV	40keV	30keV	20keV
SiO ₂ %	50.07	43.94	47.21	43.71	45.10	47.82	51.05
TiO ₂ %	0.07	0.08	0.09	0.08	0.09	0.08	0.09
Al ₂ O ₃ %	1.70	2.66	2.62	2.61	2.62	2.74	2.86
MnO %	0.19	0.22	0.22	0.20	0.20	0.20	0.20
MgO %	1.41	3.34	3.26	3.66	3.65	3.51	3.47
CaO %	2.23	1.56	1.62	1.67	1.69	1.71	1.81
Na ₂ O %	0.05	3.73	2.93	5.49	4.88	4.00	3.09
K ₂ O %	0.29	0.19	0.20	0.22	0.23	0.23	0.25
P ₂ O ₅ %	0.13	0.41	0.42	0.44	0.45	0.45	0.47
Fe ₂ O ₃ t %	39.92	38.31	35.87	36.34	35.53	33.68	31.15

Accuracy
(error = 100%- value given below)

	30keV	20keV	50keV	40keV	30keV	20keV
SiO ₂ %	87.76	94.29	87.30	90.07	95.51	101.96
TiO ₂ %	116.67	126.19	116.67	121.43	116.67	126.19
Al ₂ O ₃ %	156.18	154.22	153.43	153.92	161.37	168.04
MnO %	114.04	114.04	104.39	105.26	106.14	102.63
MgO %	236.52	231.32	259.69	258.87	248.82	246.10
CaO %	69.73	72.50	74.81	75.56	76.76	81.09
Na ₂ O %	7453.33	5856.67	10986.67	9760.00	7990.00	6186.67
K ₂ O %	66.67	68.39	74.71	78.16	78.74	84.48
P ₂ O ₅ %	312.82	323.08	341.03	346.15	347.44	361.54
Fe ₂ O ₃ t %	95.97	89.84	91.02	89.01	84.36	78.02

Appendix 3: The complete Quantitative data of Sample 18

This table displays the quantitative point data which was used to determine a general or average composition per layer. Six random points per chosen layer were analyzed, but it was made certain that no or as little as possible interference of veins and other layers would occur. Na is so high because its peak is located on the Si and Al slope.

Wt%	Na	Mg	Al	Si	P	K	Ca	Ti	Mn	Fe _(TOTAL)
black 1a	5.27	2.18	0.84	43.64	0.2	0.05	0.08	0.06	0.14	47.55
black 1a	6.07	1.58	0.84	55.20	0.21	0.04	0.06	0.05	0.11	35.85
black 1a	5.68	1.47	0.99	66.86	0.21	0.03	0.07	0.04	0.07	24.57
black 1a	4.95	1.46	1.10	59.90	0.20	0.04	0.05	0.05	0.06	32.18
black 1a	5.34	1.34	1.12	54.70	0.21	0.03	0.05	0.06	0.05	37.12
black 1a	5.14	1.39	0.91	64.37	0.20	0.02	0.04	0.05	0.04	27.84
average	5.41	1.57	0.97	57.45	0.21	0.04	0.06	0.05	0.08	34.19
pink 2	6.02	1.82	1.09	87.46	0.29	0.03	0.05	0.02	0.01	3.22
pink 2	5.79	1.85	1.10	88.90	0.30	0.05	0.06	0.02	0.01	1.93
pink 2	5.52	1.66	1.09	88.45	0.30	0.05	0.07	0.01	0.01	2.85
pink 2	6.06	2.01	1.09	87.21	0.28	0.04	0.05	0.02	0	3.25
pink 2	6.04	1.74	1.12	87.31	0.3	0.04	0.05	0.01	0	3.39
pink 2	6.28	1.80	1.08	89.37	0.29	0.05	0.06	0.01	0.00	1.04
average	5.95	1.81	1.10	88.12	0.29	0.04	0.06	0.02	0.01	2.61
pink 4	5.64	1.59	1	78.68	0.26	0.05	0.04	0.02	0.03	12.69
pink 4	5.99	1.91	1.11	89.87	0.27	0.05	0.05	0.01	0.00	0.74
pink 4	6.08	1.70	1.09	88.10	0.32	0.06	0.06	0.01	0.01	2.58
pink 4	5.84	1.86	1.1	89.6	0.34	0.04	0.06	0.01	0	1.16
pink 4	5.66	2.00	1.09	90.42	0.32	0.05	0.05	0.01	0.00	0.41
pink 4	5.75	1.69	1.08	89.09	0.32	0.05	0.05	0.01	0	1.95
average	5.83	1.79	1.08	87.63	0.31	0.05	0.05	0.01	0.01	3.26
red 2	4.66	1.54	0.90	66.28	0.23	0.05	0.05	0.04	0.11	26.14
red 2	5.53	1.32	0.88	67.90	0.26	0.04	0.04	0.03	0.11	23.88
red 2	4.73	1.39	0.85	66.58	0.25	0.03	0.04	0.03	0.12	25.97
red 2	4.85	1.47	0.89	61.88	0.25	0.03	0.04	0.04	0.18	30.37
red 2	5.59	1.37	0.85	51.41	0.24	0.04	0.05	0.04	0.22	40.21
red 2	5.24	1.44	0.89	65.69	0.32	0.03	0.04	0.03	0.17	26.14
average	5.10	1.42	0.88	63.29	0.26	0.04	0.04	0.04	0.15	28.79
red 3	5.44	1.44	0.73	44.49	0.27	0.06	0.04	0.04	0.21	47.27
red 3	5.44	1.32	0.82	54.64	0.27	0.03	0.04	0.04	0.15	37.24
red 3	5.25	1.43	0.86	53.70	0.27	0.03	0.04	0.04	0.16	38.23
red 3	5.11	1.52	0.88	60.82	0.28	0.04	0.05	0.04	0.11	31.16
red 3	5.47	1.35	0.83	61.45	0.29	0.03	0.04	0.04	0.09	30.41
red 3	5.89	1.41	0.90	55.68	0.32	0.04	0.05	0.05	0.10	35.58
average	5.43	1.41	0.84	55.13	0.28	0.04	0.04	0.04	0.14	36.65
red 4	5.04	1.27	0.73	52.83	0.21	0.03	0.04	0.05	0.08	39.72
red 4	4.54	1.21	0.93	65.1	0.22	0.05	0.04	0.04	0.05	27.82
red 4	5.25	1.45	0.84	55.42	0.27	0.06	0.05	0.05	0.05	36.55

red 4	5.56	1.41	0.82	56.19	0.26	0.03	0.05	0.04	0.09	35.56
red 4	4.83	1.49	1.01	69	0.26	0.04	0.05	0.03	0.04	23.25
red 4	4.76	1.6	0.93	62.18	0.25	0.03	0.05	0.04	0.1	30.05
average	5.00	1.41	0.88	60.12	0.25	0.04	0.05	0.04	0.07	32.16
red 5	5.87	1.6	1.08	59.44	0.22	0.04	0.07	0.04	0.06	31.58
red 5	5.67	1.64	1.06	60.09	0.21	0.06	0.07	0.05	0.05	31.11
red 5	5.53	1.67	1.04	64.49	0.23	0.05	0.07	0.04	0.05	26.84
red 5	6.46	1.75	1.36	80.53	0.28	0.07	0.07	0.03	0.01	9.43
red 5	5.61	1.68	1.11	68.32	0.29	0.03	0.05	0.03	0.03	22.85
red 5	5.31	1.54	1.03	63.66	0.28	0.05	0.06	0.04	0.04	27.98
average	5.74	1.65	1.11	66.09	0.25	0.05	0.07	0.04	0.04	24.97
white 2	6.37	1.91	1.06	87.62	0.30	0.07	0.07	0.02	0.01	2.57
white 2	6.44	1.72	1.16	88.36	0.29	0.05	0.07	0.02	0.00	1.90
white 2	5.95	1.86	1.09	87.74	0.33	0.05	0.06	0.02	0.01	2.90
white 2	6.18	2.01	1.12	88.27	0.28	0.04	0.06	0.01	0	2.03
white 2	6.03	1.76	1.07	87.46	0.32	0.04	0.06	0.01	0.01	3.24
white 2	6.15	1.98	1.19	89.11	0.35	0.04	0.07	0.01	0.01	1.09
average	6.19	1.87	1.12	88.09	0.31	0.05	0.07	0.02	0.01	2.29
white 3	5.84	1.98	1.12	90.37	0.27	0.07	0.08	0.01	0	0.25
white 3	5.97	1.85	1.91	89.48	0.31	0.08	0.09	0.01	0.00	0.30
white 3	6.29	2.14	1.99	87.05	0.36	0.08	0.07	0.02	0	2
white 3	6.34	1.81	1.19	88.61	0.3	0.05	0.06	0.01	0.01	1.63
white 3	5.99	1.82	1.29	90.07	0.33	0.05	0.07	0.01	0	0.37
white 3	6.07	1.79	1.3	89.13	0.31	0.07	0.05	0.02	0	1.26
average	6.08	1.90	1.47	89.12	0.31	0.07	0.07	0.01	0.00	0.97
white 4	6.70	2.12	1.09	89.43	0.28	0.07	0.07	0.01	0.00	0.23
white 4	6.20	2.04	1.13	89.97	0.28	0.06	0.05	0.01	0.00	0.26
white 4	6.53	2.16	1.18	89.13	0.30	0.12	0.11	0.02	0.00	0.45
white 4	6.34	1.93	1.21	89.77	0.29	0.08	0.08	0.01	0.01	0.28
white 4	6.78	1.99	1.12	89.32	0.29	0.05	0.07	0.01	0.00	0.36
white 4	5.88	1.74	1.16	90.18	0.31	0.03	0.05	0.01	0.00	0.62
average	6.41	2.00	1.15	89.63	0.29	0.07	0.07	0.01	0.00	0.37

The table below displays the quantitative data of lines perpendicular to all red layers. This data was used to determine whether the qualitative Fe-Mn relations would also be visible in the quantitative data. 10, 13, and three times 5 points respectively were analyzed for the red layers 1-5. And the starting and final points were chosen so that no interference of other layers would occur. Na is so high because its peak is located on the Si and Al slope.

Wt%	Na	Mg	Al	Si	P	K	Ca	Ti	Mn	Fe _(TOTAL)
Red 1	4.81	1.58	0.88	67.95	0.22	0.04	0.06	0.04	0.07	24.35
Red 1	5.16	1.5	0.94	66.39	0.23	0.04	0.05	0.04	0.07	25.57
Red 1	5.44	1.42	0.88	60.21	0.23	0.04	0.05	0.04	0.1	31.58
Red 1	4.79	1.34	0.85	53.17	0.23	0.03	0.04	0.04	0.14	39.37
Red 1	5.38	1.51	0.7	45.29	0.24	0.03	0.04	0.05	0.18	46.6
Red 1	5.14	1.66	0.77	41.35	0.24	0.04	0.04	0.05	0.19	50.51
Red 1	5.58	1.51	0.74	43.26	0.23	0.05	0.04	0.05	0.19	48.35
Red 1	5.15	1.58	0.76	48.34	0.22	0.05	0.04	0.05	0.18	43.64
Red 1	5.32	1.62	0.84	54.79	0.21	0.06	0.05	0.04	0.15	36.92
Red 1	5.54	1.44	0.82	61.56	0.26	0.05	0.04	0.04	0.12	30.11
Red 2	5.75	1.52	0.79	46.79	0.26	0.05	0.05	0.04	0.21	44.55
Red 2	5.65	1.49	0.82	45.62	0.25	0.05	0.04	0.04	0.2	45.84
Red 2	5.42	1.48	0.84	46.77	0.26	0.05	0.04	0.05	0.21	44.89
Red 2	5.39	1.54	0.86	49.38	0.29	0.05	0.04	0.05	0.21	42.2
Red 2	5.51	1.52	0.79	53.32	0.25	0.05	0.05	0.04	0.21	38.24
Red 2	5.53	1.43	0.79	53.87	0.26	0.06	0.05	0.05	0.21	37.76
Red 2	4.95	1.43	0.85	51.79	0.27	0.06	0.05	0.05	0.23	40.33
Red 2	5.69	1.65	0.82	48.39	0.27	0.05	0.05	0.04	0.25	42.78
Red 2	5.85	1.64	0.85	46.94	0.3	0.05	0.05	0.05	0.27	44
Red 2	5.82	1.72	0.89	48.19	0.28	0.05	0.07	0.05	0.26	42.65
Red 2	5.87	1.59	0.85	51.05	0.29	0.06	0.07	0.05	0.24	39.92
Red 2	6.06	1.51	0.92	56.12	0.32	0.06	0.08	0.04	0.2	34.69
Red 2	5.9	1.69	0.94	63.15	0.3	0.06	0.08	0.04	0.14	27.71
Red 3	5.71	1.44	0.74	45.31	0.29	0.04	0.04	0.05	0.2	46.17
Red 3	5.11	1.48	0.71	42.39	0.29	0.04	0.04	0.05	0.22	49.67
Red 3	5.7	1.38	0.69	38.33	0.28	0.04	0.04	0.05	0.23	53.25
Red 3	5.98	1.42	0.7	40.09	0.3	0.04	0.04	0.05	0.23	51.17
Red 3	5.79	1.48	0.82	51.17	0.28	0.05	0.05	0.04	0.18	40.13
Red 4	4.73	1.32	0.77	52.26	0.22	0.04	0.05	0.05	0.09	40.49
Red 4	4.79	1.22	0.79	55.92	0.21	0.05	0.05	0.05	0.08	36.84
Red 4	4.92	1.38	0.83	60.94	0.22	0.04	0.04	0.04	0.06	31.52
Red 4	4.62	1.43	0.86	65.68	0.24	0.03	0.05	0.04	0.05	27.01
Red 4	5.22	1.31	0.99	69.15	0.25	0.03	0.05	0.03	0.05	22.92
Red 5	5.27	1.66	1.04	62.52	0.22	0.05	0.07	0.05	0.05	29.08
Red 5	5.22	1.54	1.07	64.38	0.22	0.05	0.06	0.04	0.05	27.36
Red 5	5.01	1.67	1.1	67.26	0.25	0.05	0.06	0.05	0.04	24.5
Red 5	5.03	1.65	1.15	70.94	0.23	0.05	0.06	0.04	0.04	20.81
Red 5	5.11	1.66	1.17	73.89	0.22	0.06	0.06	0.04	0.03	17.76

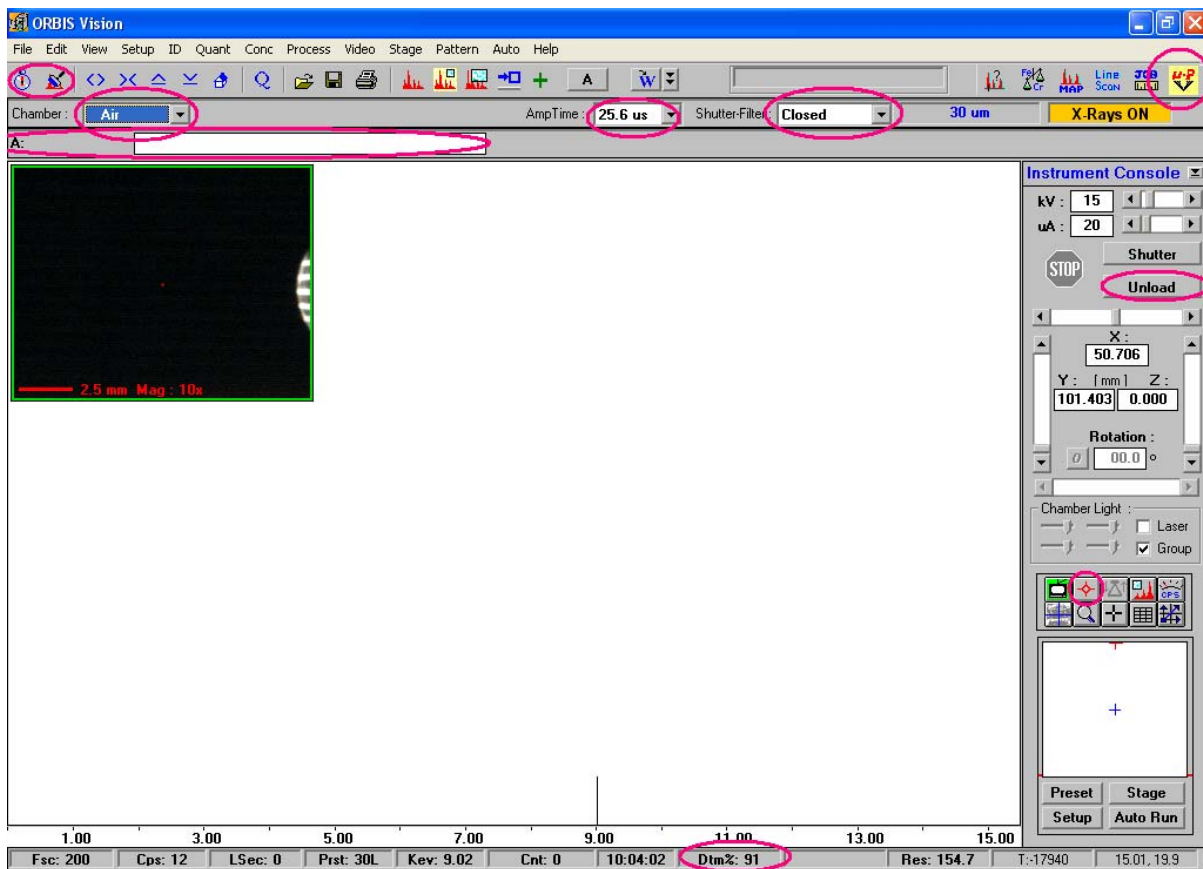
☞ Appendix 4: The Micro XRF Work routine User's Manual ☜

The Micro XRF Work routine User's Manual

By Sophie Jansen under supervision of Tilly Bouten

In general (<i>qualitative</i> analysis)	page II
Peak identification	page V
Spectrum text: add, delete or edit	page VI
Multi-color spectral overlay	page VIII
Printing of spectra or sample images	page IX
Constructing measuring-parameters	page X
Linescan construction (<i>qualitative</i>)	page XI
Via LineScan Icon	
X-ray map construction (<i>qualitative</i>)	page XIII
Help with determining the resolution	page XV
Loading and Printing of maps	page XVI
Automatic analysis of a point, line or matrix, and multiples (<i>qualitative</i>)	page XVIII
Analysis of a point, line or matrix, and multiples via Stage table	page XVIII
Point	page XIX
Line	page XIX
Matrix	page XIX
Linescan via Montage and Stage Table	page XX
Using the Montage feature	page XX
Creating the Linescan	page XX
X-ray map construction via Montage and Stage Table	page XXII
Maps with preset proportions (5:4)	page XXIII
Maps with a manually determined shape	page XXIII
Multi-Field mapping	page XXV
Auto – Setup Output	page XXVII
Re-processing of data	page XXIX
Executing a <i>quantitative</i> analysis	page XXX

In general



- Start Orbis Vision program
- Instrument Console: Unload sample
- Open chamber and insert the sample in the micro XRF while attaching it with special clay or tape in the middle of the stage, close the chamber.
- Check if the röntgen source is enabled --> **X-Rays ON** top right in Orbis Vision program or the middle light on the instrument
When off: hold the middle light on the instrument (X-Ray) pressed down until it switches on
- Choose Chamber: *Vacuum*, to start the pump --> top left in program
NB it is possible to work in Air mode, however, the X-rays of elements like Si, Al, Mg and Na are for the most part absorbed in air. Because of this, there are hardly any elements retrieved in the spectrum. This is a major problem in Earth science because these elements are often main elements.
- When the Vacuum box is light green, the vacuum in the chamber is low enough to be able to perform proper measurements.

- Choose $\mu probe$ option -->  icon top right. (A standard way to work is with the 30 μ m poly-capillary, however, 1 en 2 mm apertures are also available --> Setup – X-ray Tube...
- Put X and Y to 50, the stage is now centered under the bundle.
- Increase the height of the table by increasing the Z. for this, choose as a maximum height (in mm) : 90 mm minus sample height
 - Thus, if the sample is 3 cm thick: $90 - 30 = 60$ so $Z=60$
- Next, focus by means of smaller steps in the 10X magnification ( icon bottom right) until the sample is approximately focused by clicking on the adjustable beams
- Change the magnification to 70x ( icon bottom right) and fine-tune the focus by means of the slider and arrows). The *Laser* --> middle right, may help with finding the right height. *Autofocus* ( icon bottom right) may also be helpful when the surface has sufficient "color relief"
- Choose a position on the sample. To do this without using X or Y use the  *Get Feature* button --> bottom right, this centers the point on the sample where one has clicked
- Give the spectrum a name in the top white box with A (or B) in front of it, one can use this box to record the measuring conditions like keV, μ A, 30 μ m etc.
- Choose Voltage en Current (ex. 30kV, 100 μ A)
 - NB** the chosen voltage should depend on the elements to be measured
- Choose an Amplifier Time, this is the time that the detector is open for receiving signal --> *AmpTime* option top middle
 - NB** a good AmpTime is 6.4 μ s
- Choose *Live time*, this is the time that a point is being measured --> Setup - Preset & Memory..., here, the Live time is in seconds
 - NB** this time depends on the type of sample and the defined problem, for maps \sim 1 sec, for quantitative measurements 30-300 sec. *LSec* is the live time passed --> left of the center at the bottom
- Open Shutter-Filter --> top right
- To start measuring push *Collect Spectrum* -->  icon top right, to stop the measuring when it has not finished yet, push the same button
 - NB** the spectrum shows intensities, it is, thus, a qualitative analysis
- Check *Dtm%* = Measured Dead Time Percentage --> right of the center at the bottom.

NB Dead time is the time that the detector needs to process a certain amount of pulses and is not available for new pulses. A high Dead time results in very long waiting times, and with a low Dead time less signal is received per unit time. For a higher throughput one always has to look for an optimum between speed and amount of signal. A maximum desirable Dtm% is 35-40%

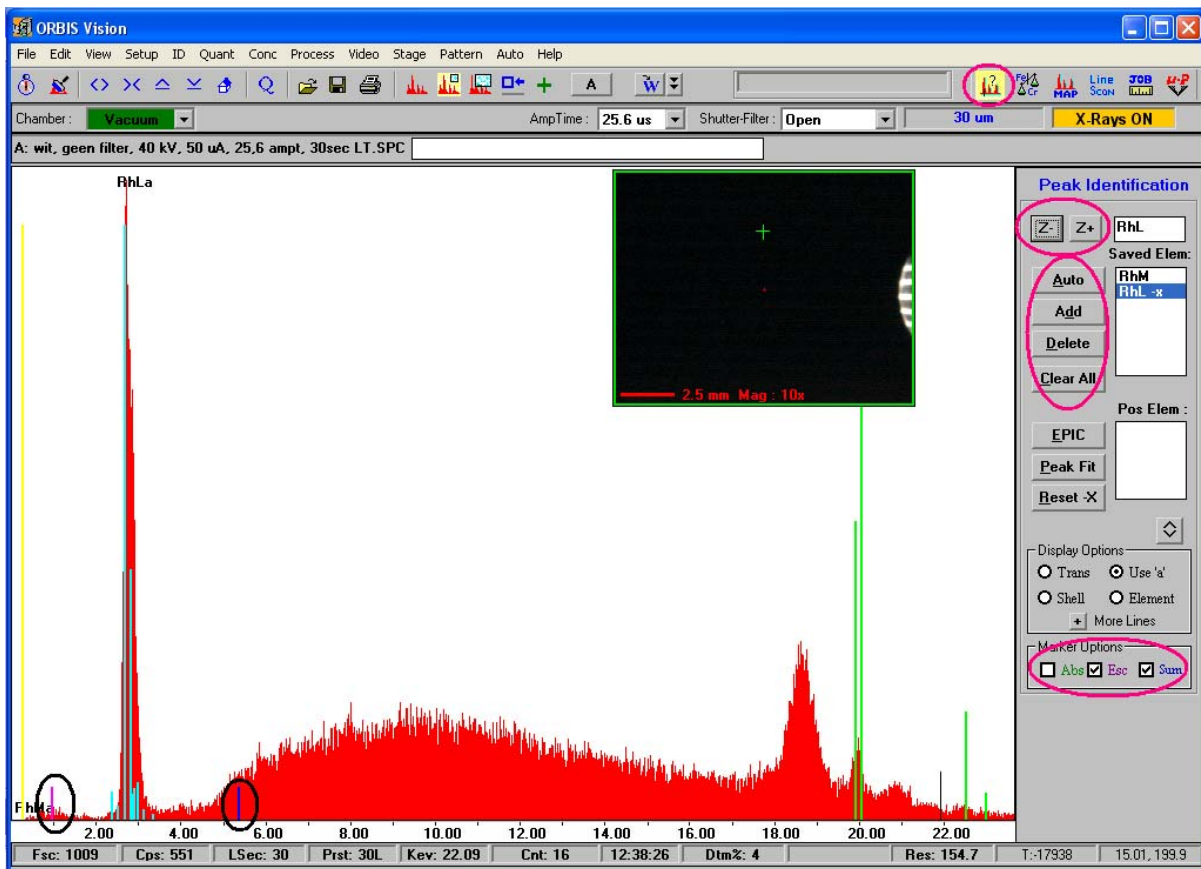
- When the Dtm% is not below 35-40% one has to adapt the AmpTime, μA or the filter until the Dtm% is below these numbers.

NB for further explanations see '**Constructing measuring-parameters**'

- To find the optimal image for the spectrum, depending on one's wishes, one can adapt the screen by holding the spectrum with the left button of the mouse and moving the mouse across the screen to adapt the vertical and horizontal axes.
- When the sample image is blocking the spectrum, one can move this image to the other side of the screen by clicking  (--> top center)

Peak identification

The program can identify elements from Sodium (Na) (Z=11) up to Berkelium (L) (Z=97).



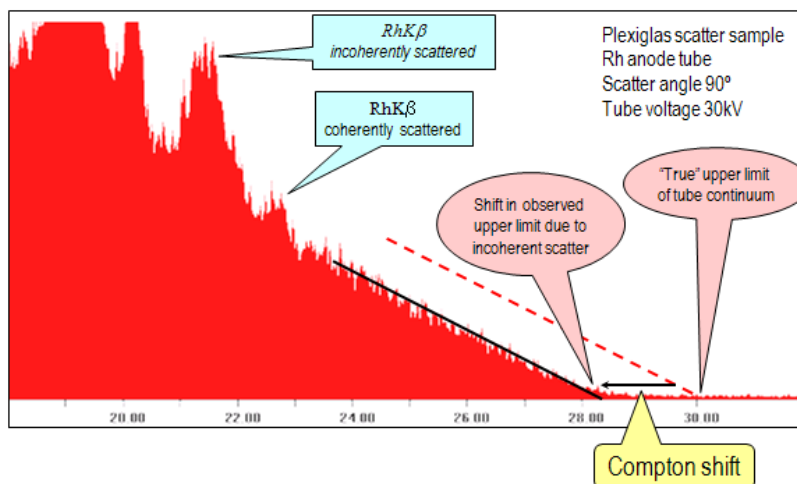
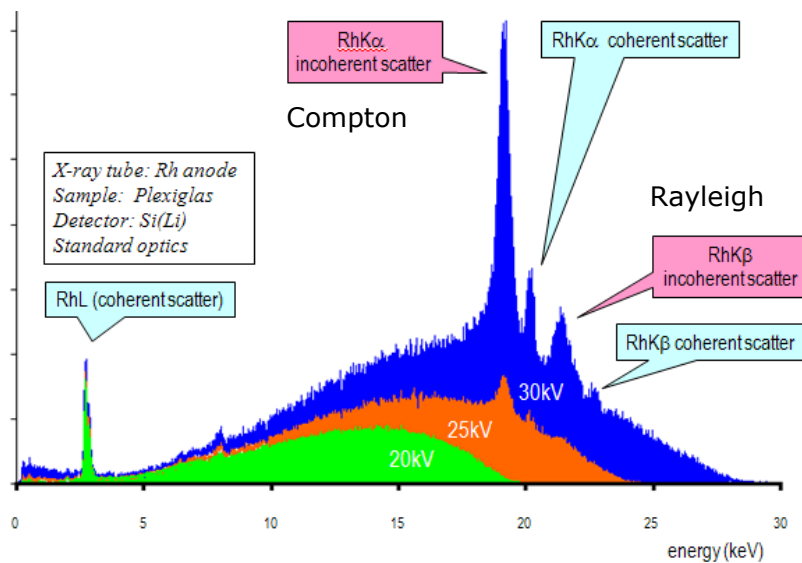
- Push  --> top right, to enter the peak identification screen
- Make sure that there is a spectrum from which one can identify the peaks. This can be a new spectrum or it can be a previously saved spectrum.
- Push Clear All --> top right
- Push Auto --> top right, to let the program identify the peaks.

NB always verify if the peak identification is indeed correct, the program can be wrong! One can ignore the peaks below 1.00 kV, this is static, because of the Beryllium filter that is located in front of the detector.

- A useful method is to start with the K-lines of the low elements. One can get to the low elements by repeatedly pushing the Z-button --> top right. By pushing the Z- and Z+ buttons, one changes the element peaks from the library that one uses to identify the peaks, typing the desired element and K, L or M is also possible. The light green lines are the K-lines, the light blue lines are the L-lines and the yellow lines are the M-lines (for additional explanations about these lines and the reaction behind them Google XRF on the internet)

- If the lines match with the peaks, push Add --> top right, to add the element to the list
- **Escape** and **Sum** peaks are artifacts of the μ -XRF method. The Escape peak is the kV of an element – 1.74 kV of Si. Sum peaks are peaks that are the result when the x-ray quant of an element entered the detector twice at precisely the same moment and was counted as one kV. These peaks are thus not element peaks and cloud the data. If one wants to name the Escape and the Sum peaks, than one has to tick these two options in the bottom right (pink and blue lines) and, if desired, add the names manually to the spectrum: see '**Spectrum text: add, delete of edit**'

NB there can also be peaks that cannot be identified these peaks can be **Compton** or **Rayleigh** scattered peaks (see below) or **diffraction** peaks due to the reflection of the sample surface. Diffraction peaks can be identified by turning the sample 90° and by comparing the 2 spectra, if the peaks differ then they are very likely to be diffraction peaks. Also see Orbis Vision User's Manual, Chapter 5, p. 40



Spectrum text: add, delete or edit

Add:

- Edit – Add Text
- Click 1 time on the location where the texts needs to start, the text beam appears
- Insert the wanted text and press Enter

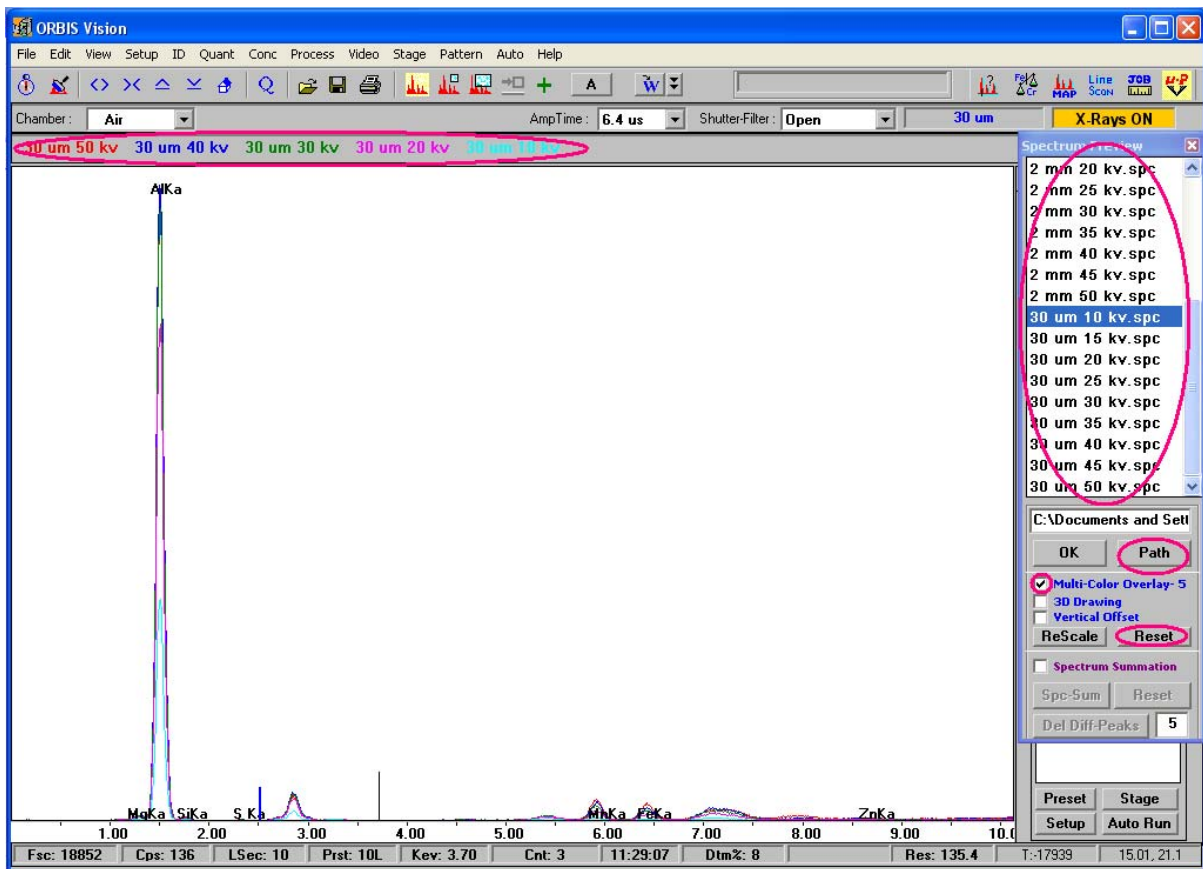
Delete:

- Edit – Clear Text
NB this deletes ALL the manually added text

Edit:

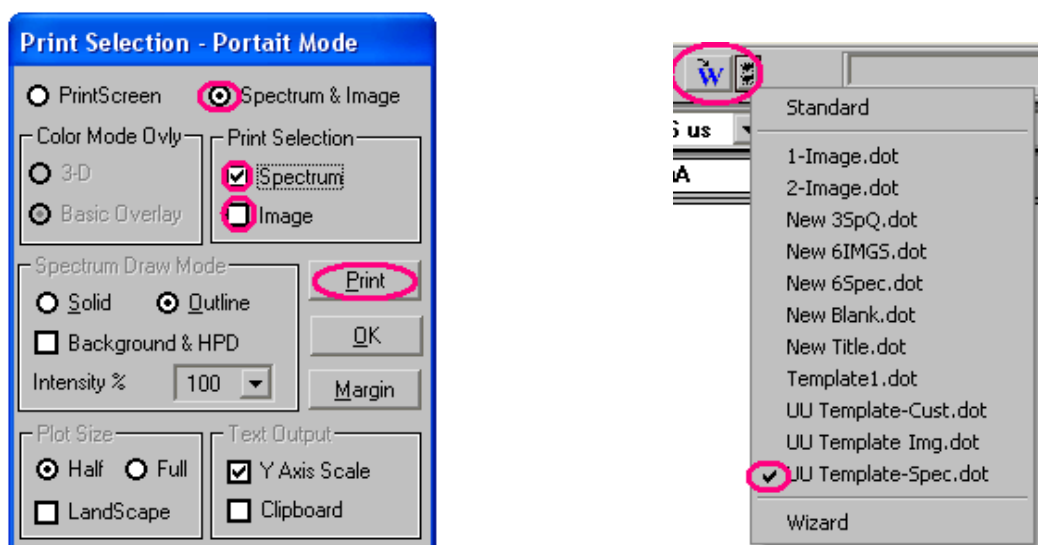
- Edit – Edit Text
- Click on the text that had to be altered
- Adapt the text or drag the text beam to the proper location
- Press enter

Multi-color spectral overlay



- File – Spc Preview...
- Push *Path* --> center right
- Select a spectrum file in the folder that one wants to upload into the program
- Push *Open*
- Tick the *Multi-Color Overlay* box --> center right
 - NB** one can also choose *3D drawing* or *Vertical Offset*
- Select a maximum of 6 spectra that one wants to overlay and click on them each individually
 - NB** if one choose the wrong spectra one can push *reset* and all the chosen spectra will be unselected
- In the top of the window the names of the selected spectra are visible in the color that the spectra have in the overlay

Printing of spectra or sample images



One can print newly measured spectra or sample images by:

- Choosing File – Print
- Clicking *Spectrum & Image*
- Ticking the *Spectrum* or *Image* box under the Print Selection option
 - NB** when the Plot Size is chosen as Half, and one want both a spectrum and an image, they are printed on one page with in the upper half the spectrum and the image below
- And pushing *Print*

One can also want to transfer spectra and/or images to a special Utrecht University word document:

- Open (first) spectrum/image that one wants to send to the UU template
- Choose the two down pointing arrows of the  icon(--> top center) to choose the UU Template-Spec.dot for transferring spectra or choose UU Template Img.dot for transferring images
- Push on the W of the  icon to start the transfer to the Word template
 - NB** the program adapts the size of the images so that everything will fit on 1 page.
- Open the next spectrum/image that needs to be transferred to the template and again push of the W of the  icon. Repeat this process until the desired amounts of spectra or images are transferred.
- Save the created Word file and, if desired, change the size of the spectra or images and print the page(s)

Constructing measuring-parameters

There are several factors that determine the measuring-parameters and the Dead time of the detector:

- The *Voltage*: This determines if an element will or will not be excited. One needs at least the specific energy of an element to excite this element. An optimal signal is produced with twice the specific energy for the heaviest to be measured element. A higher voltage will, in general, result in more signal but also in a higher Dead time.
- The *Current*: The amount of current that one uses for the emission is proportional with the amount of signal. Higher currents result in more signal and a higher Dead time.
- The *Amplifier Time*: The AmpTime can be adapted into predefined amounts and determines how much signal can be processed at the same time. The Amp. Time varies from 0.5 to 12.8 µsec. In practice, the 6.4 µsec is used most often. A lower Amp. Time results besides a higher amount of signal also in a broadening of the element peaks. This makes identifying the peaks more difficult.
- The use of a *filter*, to exclude part of the primary spectrum. At present time, the 25 µm Al-filter appears most useful to cancel the Rh-L line from the spectrum, when Cl has to be measured. This will, however, have negative effects on the detection limit and yield of the lighter elements.

Per sample type, it has to be determined what the optimum setup for the Micro-XRF is.

NB even though they do not influence the Dead time, the counting times are important while optimizing the Micro-XRF. For a higher certainty in analysis one needs a good peak shape and enough counts. With mapping, besides the high certainty of analysis, the Total time of the analysis is also important. Every analysis is a compromise between the amount of time and the accuracy of the analysis. For mapping, always calculate the total measuring time to see if the scan can be completed in the intended or available measuring time:

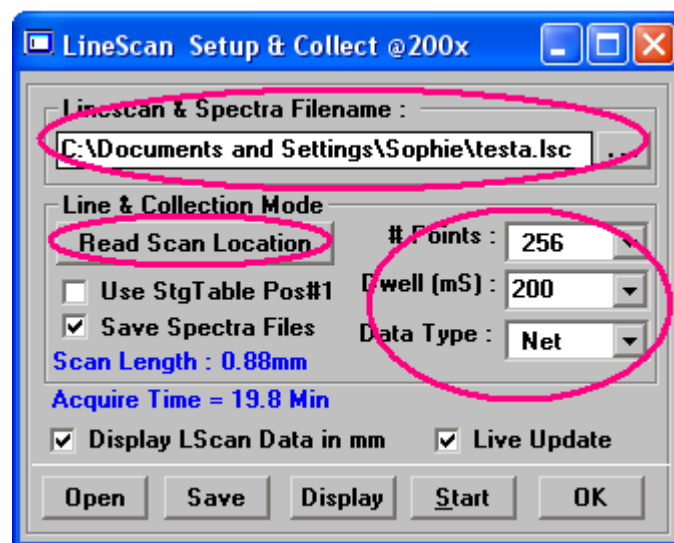
Actual running time = number of X-points x number of Y-points x measuring time x 1.4 (at 40% Dtm%) + extra time for the Autofocus and the saving of spectra and images

Adapting one or several of the above explained parameters will result in more realistic scans.

Linescan construction via LineScan icon

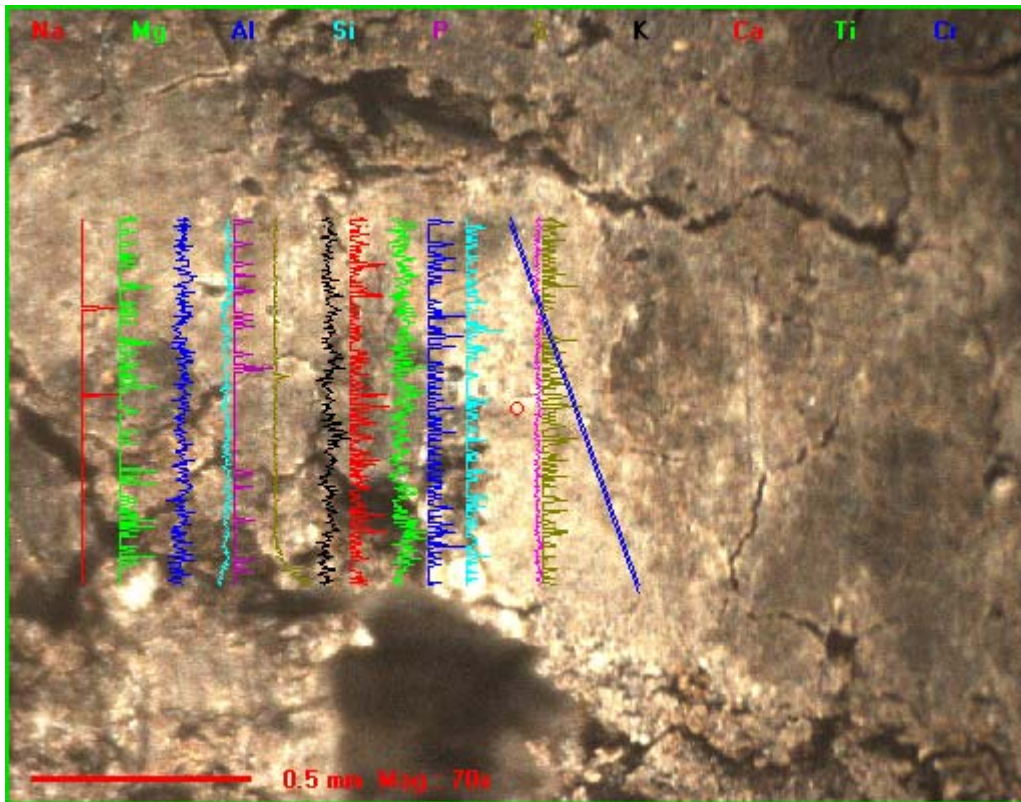
Creating a linescan via the *LineScan* option (), results in intensity graphs that one can place over the sample picture, but it also has the option to save spectra.

- Choose in μ Probe mode ( icon top right) the voltage and current (Dead time <40%) and focus the image
- Create a spectrum to determine the elements that will be measured
- Choose in *Peak ID*-mode ( icon top right) the elements that will be mapped by means of the created spectrum, consider adding extra elements that might be expected in the sample
- Tick Video – Line --> center top
 - NB** the desired line can also be chosen via Stage – Table, as described **above**, than choose *Use StgTable Pos#1*
- Draw the desired line in the live image
- Push *LineScan*  --> top right



- Give the to be run scan a name, in the proper folder
- Push *Read Scan Location*, this provides the total length of the line, with this, calculate the desired amount of scan points
- Insert # of Points
- Choose a measuring time and insert this in *Dwell (mS)*
- Change *Data Type* to Net
- Choose, if necessary, Save Spectra Files
- Push Start, the graphs are immediately visible in the bottom of the window

- When the scan is finished, one can push Display to show all the element graphs individually
- Via VideoOverlay – Horizontal / Vertical one can overlay the graphs over the drawn line (see below, the angles dark blue line is the drawn line)



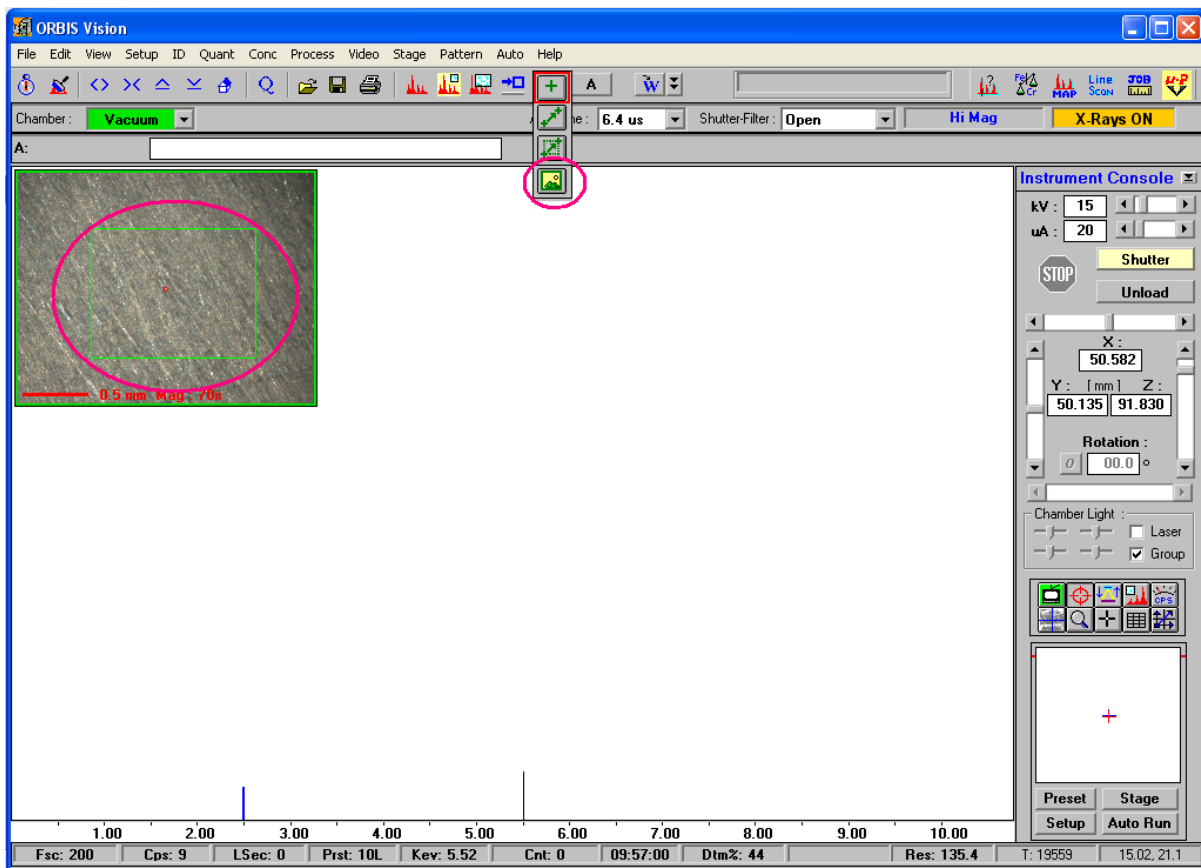
- To save the image, go to File – Save As – choose Save as *Type*: Image Bitmap.bmp
NB to see the further saving options of the program see Orbis Vision User's Manual, Chapter 5, p. 33

X-ray map construction

When creating X-ray maps take the following factors into account:

- A practical to be executed map does not contain more than 256x200 or 512x400 points.
- A longer counting time per spot provides a better spectrum, and thus a better element distribution, but also a much longer measuring time.
- For main elements, a measuring time for mapping of 1000msec is fairly long, for minor and trace elements one will require much longer counting times.
- A good balance between counting time and resolution of the sample surface is preferentially.

Creating an X-ray map:



- Choose in μ Probe mode ( icon top right) the voltage and current (Dtm% <40% when running the spectrum) and focus the image
- Create a spectrum to determine the elements that will be measured
- Choose in *Peak ID*-mode ( icon top right) the elements that will be mapped by means of the created spectrum

- Choose, on the sample, a position that represents the center of the area where one wants to perform the linescan (via the Get Feature mode )
- Choose in Video Pointer Mode the  icon --> top center
- Define the to be mapped area with the mouse pointer on the Live Video image of the sample (green box is the defined area, can be any area)
- Select in the *Collection* tab of the *Mapping*-mode ( icon top right) the Matrix of resolution

NB First run a test map with a smaller resolution, matrix 32x25, than run the actual test with a good resolution

- Tick the *Color Overlay* box --> right center
- Choose *Dwell* time, for main elements <1000 msec, for minor and trace elements ≥10000 msec
- Set the EDS-mode to Live time
- Data type always on Net Integr. (otherwise the background will be measured as well)
- Spectrum map to 16-Bit so that the spectra are also being saved and can be reprocessed at a later point of time: see '**Re-processing of data**'

NB not appropriate for quantitative processes

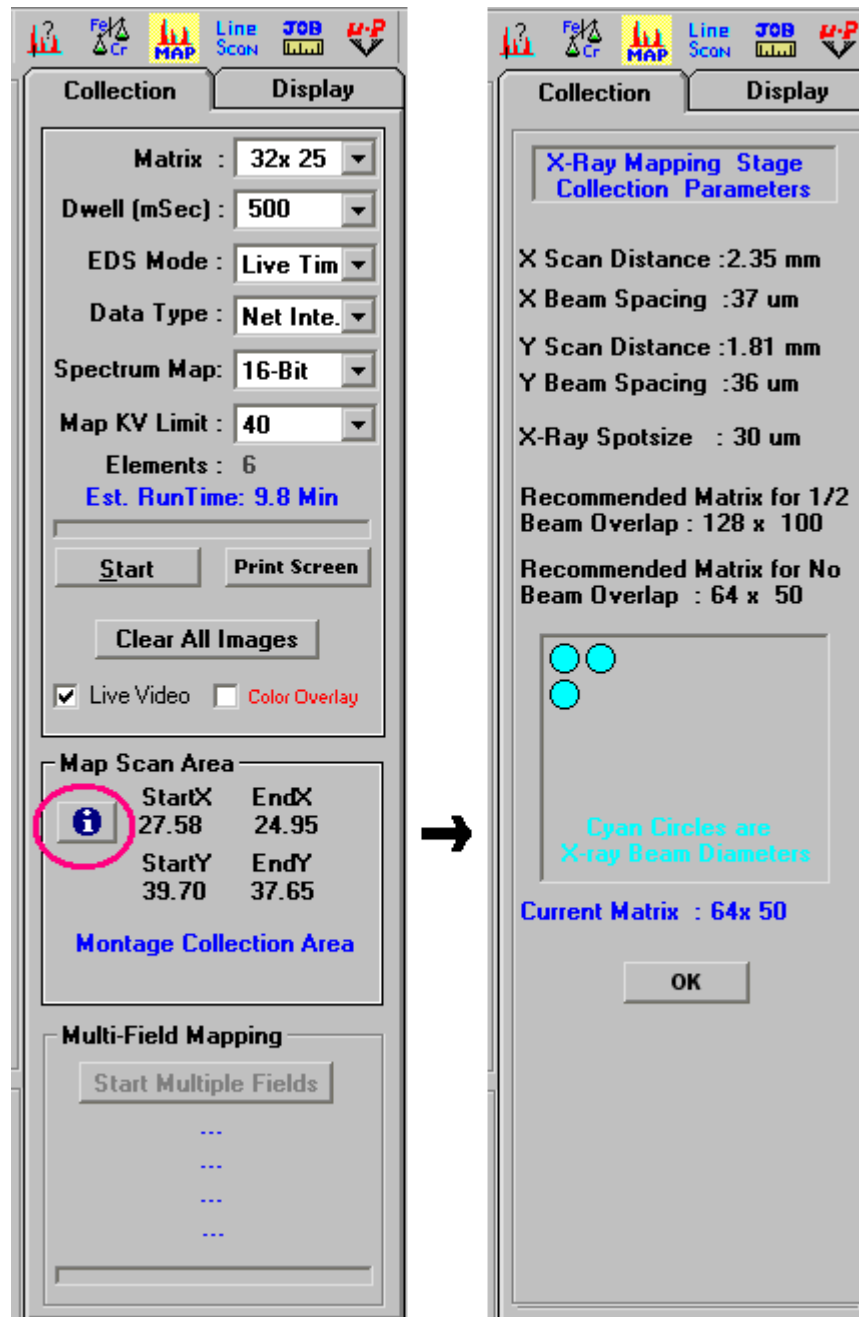
- Map kV Limit is standard on 40kV
- Check the amount of to be measured elements that were selected for mapping
- Push  --> top right, to name the maps and to choose the proper folder where they are being saved

NB the name cannot contain spaces

- Push *Start*

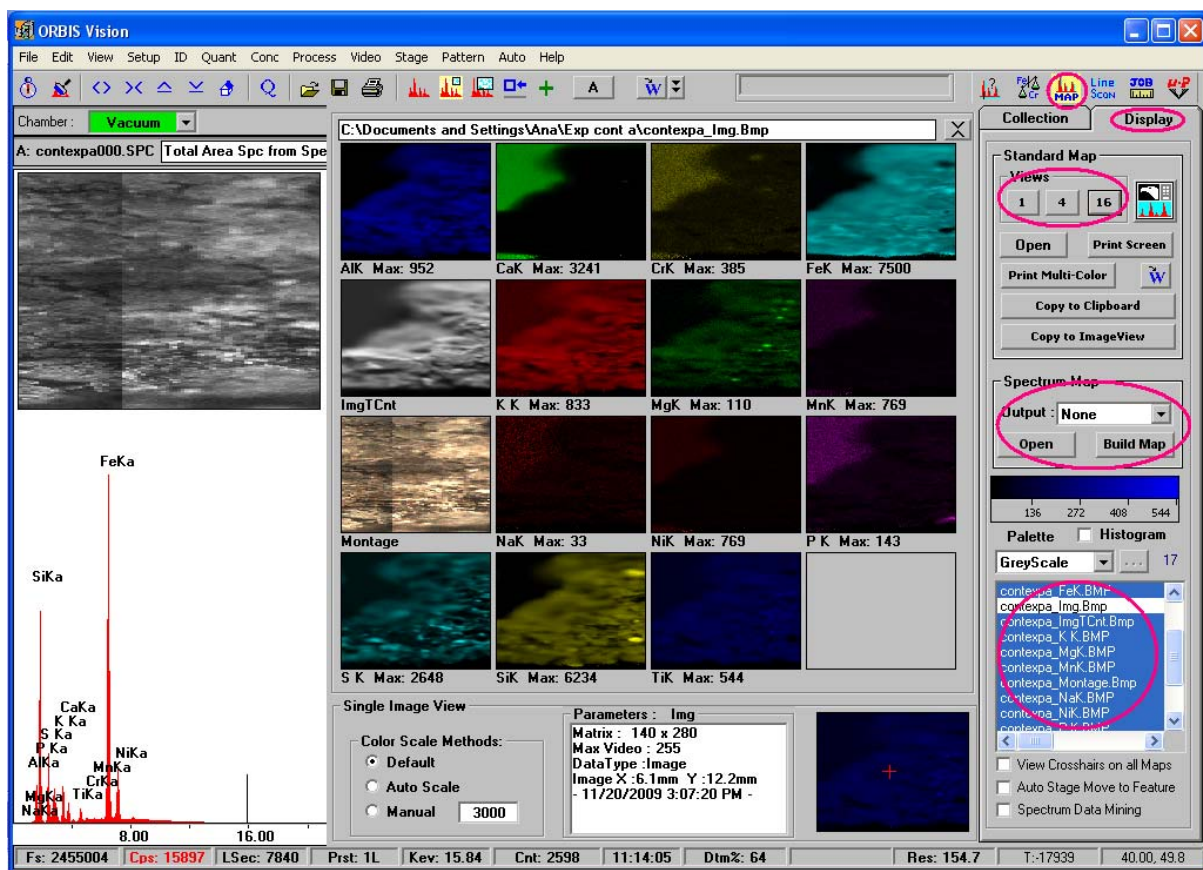
NB the Est. Run Time is usually longer than the program calculates, see '**Construction measuring-parameters**'

Help with determining the resolution

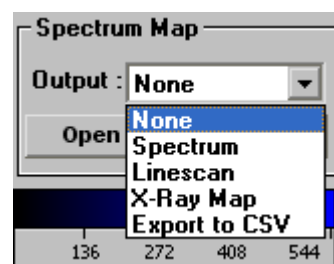


If one pushes on the information icon  in the Collection tab in the Mapping mode, a window appears containing a resolution advice. But, one can also see in how much overlap the chosen resolution results by looking at the cyan colored circles. In the top of the window the dimensions of the chosen mapping area are described.

Loading and Printing of maps

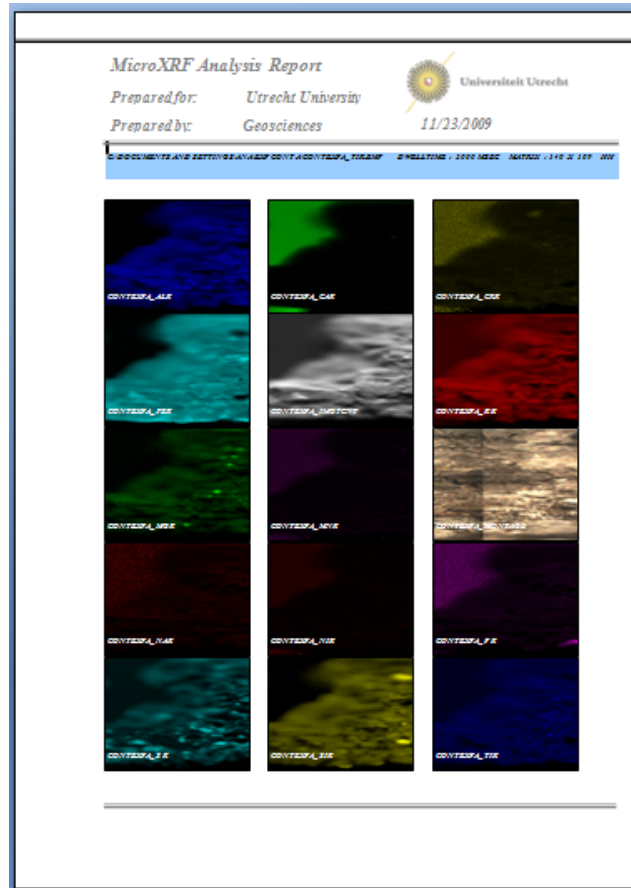


- Go to  icon --> top right
- Push *Display* tab --> top right
- Choose in the *Spectrum Map* frame --> center right, X-Ray Map



- Click *Open*
- Choose the correct **.Spd** file to upload the created maps, the maps appear right, in the lower field
- Select by means of *Ctrl* (keyboard) the desired element maps and images
 - **NB** a maximum of 15 maps or images can be send to a Word template
- Than push under *Views* --> top right, the desired amount of frames to be displayed 1, 4 of 16
- The maps appear in the window

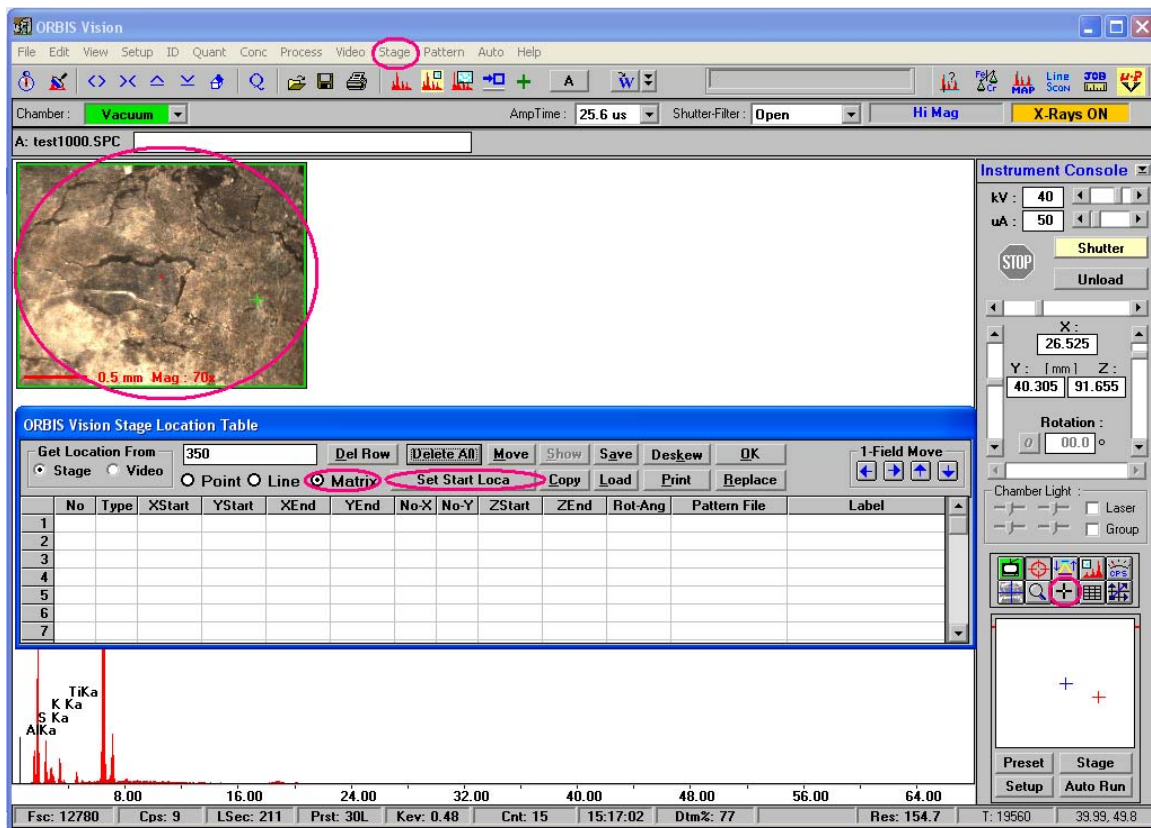
- Push the 2 down pointing arrows of the  icon (--> top center), and choose UU Template-Cust.dot
- Push on the  icon --> center right, to start the transfer to the Word template
- Save the created Word file and print the page



Automatic analysis of a point, line or matrix, and multiples

- Choose in μ Probe mode ( icon top right) the voltage and current (Dead time <40%) and focus the image
- Make sure that *Get Feature* () is enabled
- Create several spectra to determine the elements that will be measured
 - NB** only applies when making maps in the *Mapping*-mode ( icon top right)
- Choose in *Peak ID*-mode ( icon top right) the elements that will be mapped by means of the created spectrum, consider adding extra elements that might be expected
 - NB** only applies when making maps in the *Mapping*-mode ( icon top right)
- Choose, on the sample, a position that represents the center of the area where one wants to perform the analysis (via the *Get Feature* mode )

Analysis of a point, line or matrix, and multiples via Stage Table



The screenshot shows the ORBIS Vision software interface. At the top, the menu bar includes File, Edit, View, Setup, ID, Quant, Conc, Process, Video, Stage, Pattern, Auto, and Help. The 'Stage' menu is circled in red. Below the menu bar, the 'Chamber' is set to 'Vacuum', 'AmpTime' is 25.6 us, 'Shutter-Filter' is Open, and 'X-Rays' are ON. The main window displays a sample image with a red circle highlighting a region of interest. Below the image is the 'ORBIS Vision Stage Location Table' with a toolbar containing buttons like 'Get Location From', 'Del Row', 'Delete All', 'Move', 'Show', 'Save', 'Deskew', 'OK', '1-Field Move', 'Point', 'Line', 'Matrix', 'Set Start Loca', 'Copy', 'Load', 'Print', and 'Replace'. The 'Matrix' option is selected and circled in red. Below the table is an XRF spectrum showing peaks for TiKa, K Ka, S Ka, and AlKa. The 'Instrument Console' on the right shows parameters for kV (40), uA (50), X (26.525), Y (40.305), Z (91.655), and Rotation (0.0). At the bottom, the status bar displays various technical details: Fsc: 12780, Cps: 9, LSec: 211, Prst: 30L, Kev: 0.48, Cnt: 15, 15:17:02, Dtm%: 77, Res: 154.7, T: 19560, 39.99, 49.8.

- Set the *Magnification* to 70x
- Go to Stage – Table (--> center top)
- Push as required Point, Line or Matrix

Point:

- Click in the sample image on the point that needs to be measured
- Push *Save Point* --> center
- For multiple points: repeat

Line:

- Click in the sample image on the point that should be the top/left of the line
- Push *Set Start Location* --> center
- Click in the sample image on the point that should be the bottom/right of the line
- Push *Set End Location* --> center
- Calculate and adjust the amount of the be measured points in No-X en No-Y (resolution), check for what Z-values tha start and end are in focus and insert
- For multiple lines: repeat

Matrix:

- Click in the sample image on the point that should be the upper left corner of the map
 - Push *Set Start Location* --> center
 - Click in the sample image on the point that should be the lower right corner of the map
 - Push *Set End Location* --> center
 - Adjust the amount of the be measured points in No-X en No-Y (resolution) , check for what Z-values tha start and end are in focus and insert
- NB** calculate the amount of points by taking into account the 30 μm probe, the length of the to be measured area (X of Y) and the amount of overlap that one desires for the measurements



no overlap – 25% overlap – 50% overlap

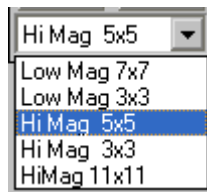
- For multiple matrices: repeat
- Save the *Stage Location Table* so that one can retrieve the values in the future
NB this only applies when the sample has not been moved (manually) in the mean time in the μXRF
- Push *OK*
- Adjust the Auto – Setup Output... settings to one's own desire, see '**Auto – Setup Output**'
- Auto – Start Auto Run

Linescan via Montage and Stage Table

Using the Montage feature

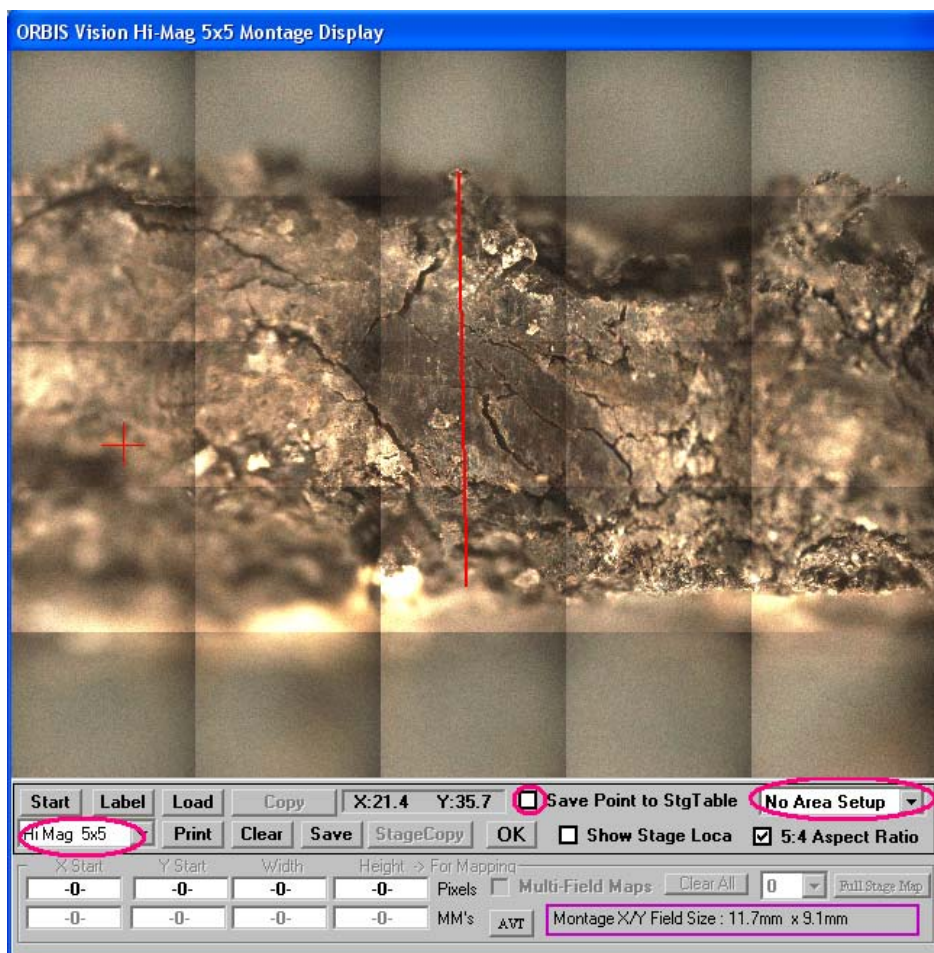
- Choose by means of Montage () in the μ Probe () option the desired points. Before this can be done, one has to take a photo of the sample. For this one can choose out of several options (see Orbis Vision User's Manual, Chapter 10, p. 229):
 - ❖ Low mag (=10x) 3x3, 7x7 images
 - ❖ High mag (=70x) 3x3, 5x5, 11x11 images

Choose by Trail & Error a good magnification to take the Photo of the sample or part of it --> bottom left



- Push *Start* to start taking the Photo
- Save the Photo

Creating the Linescan



- Tick the *Save Point to StgTable* box
- Select by means of *Set LScan Area* the to be measured line and define the line on the sample photo



- Push *OK*
- Go to Stage – Table (-->top center) and adjust the amount of to be measured points in No-X en No-Y depending on the direction of the line, check for what Z-values tha start and end are in focus and insert

NB calculate the amount of points by taking into account the 30 µm probe, the length of the to be measured area (X of Y) and the amount of overlap that one desires for the measurements



no overlap – 25% overlap – 50% overlap

ORBIS Vision Stage Location Table File : C:\Documents and Settings\Ana\Exp cont b\exp cont b.stg

Get Location From: Stage Video

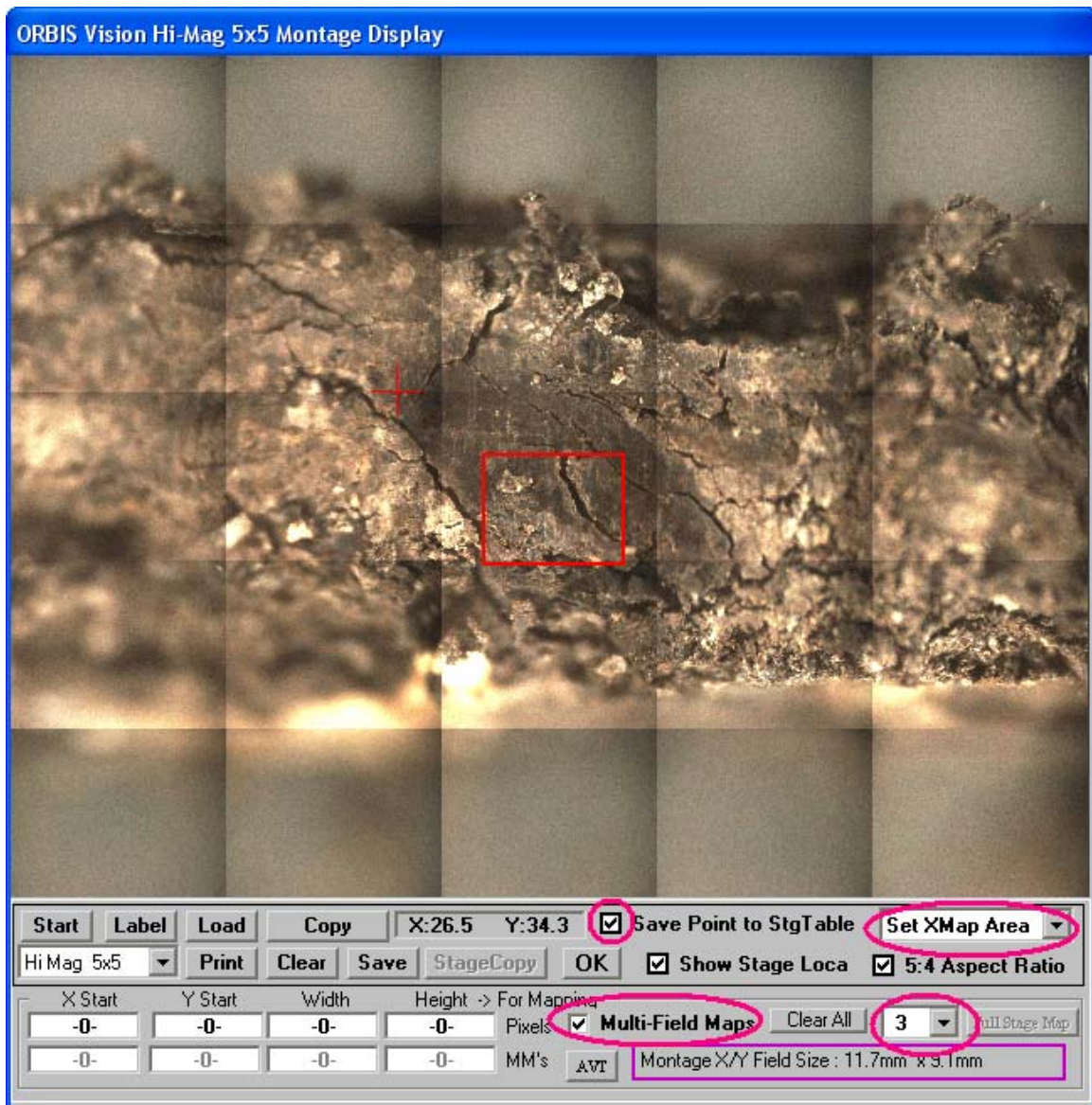
Point Line Matrix

Buttons: Del Row, Delete All, Move, Show, Save, Deskew, OK, 1-Field Move (Left, Right, Up, Down), Set Start Loca, Copy, Load, Print, Replace

No	Type	XStart	YStart	XEnd	YEnd	No-X	No-Y	ZStart	ZEnd	Rot-Ang	Pattern File	Label
1	1	L	26.490	40.300	26.450	37.320	1	250	90.800	90.800		StgMap
2												
3												
4												
5												
6												
7												

- Save the *Stage Location Table* so that one can retrieve the values in the future
NB this only applies when the sample has not been moved (manually) in the mean time in the µXRF
- Push *OK*
- Adjust the Auto – Setup Output... settings to one’s own desire, see '**Auto – Setup Output**'
- Auto – Start Auto Run

X-ray map construction via Montage and Stage Table



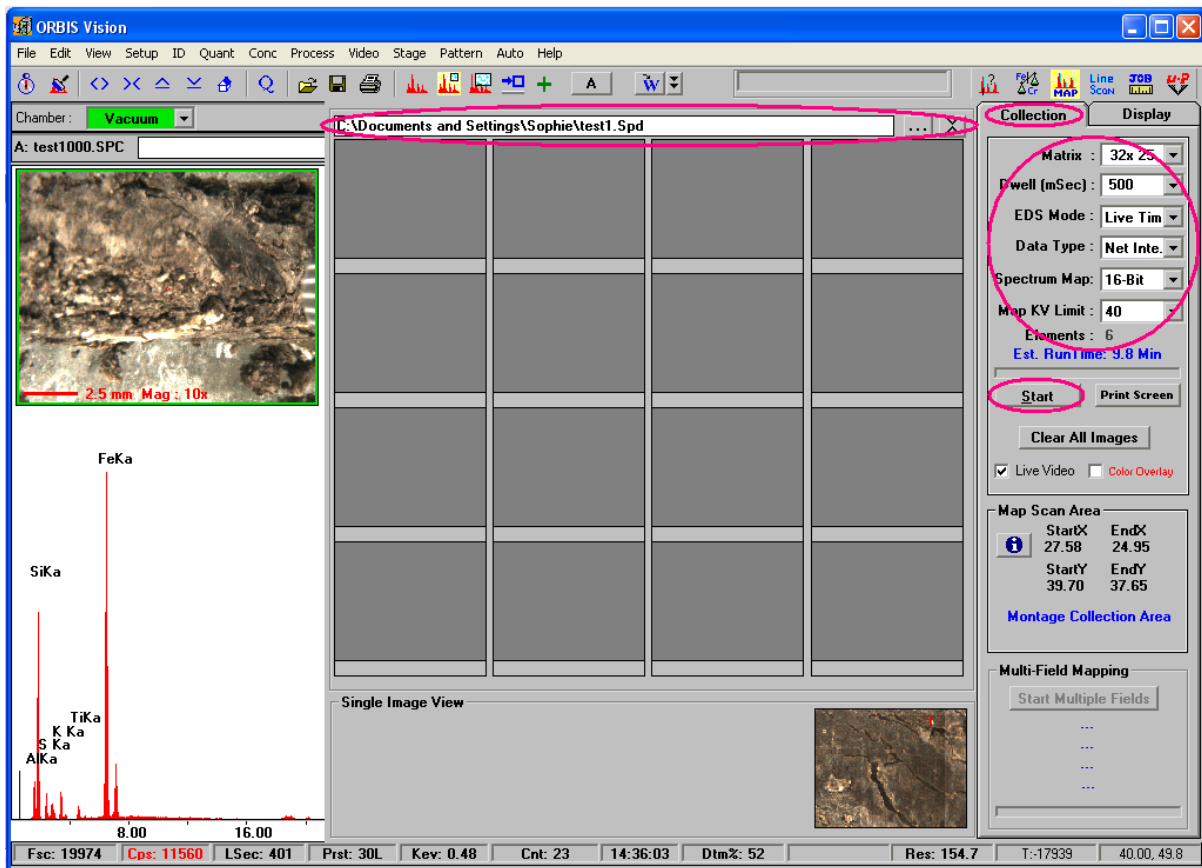
- Make a Photo of the sample in Montage, see '**Linescan via Montage and Stage Table**' and '**Using the Montage feature**'
- Tick the Save Point to StgTable box
- Now, one has 3 possibilities to create maps:
 - A) Xmap Area, this option creates maps with the preset proportions 5:4
 - B) AnyXmap Area, this option creates manually defined rectangular maps
 - C) Multi-Field Maps, with this mode, one can create several maps with the preset proportions 5:4

A) Option Xmap Area (5:4):

- Select by means of **Set Xmap Area (5:4)** the to be measured surface. The + indicates where the probe is located at present time.



- Push *OK*
- Select in the *Collection* tab of the *Mapping*-mode ( icon top right) the Matrix of resolution
NB First run a test map with a smaller resolution, matrix 32x25, to determine if high enough counts are recorded for each element, than run the actual test with a good resolution



B) Option AnyXmap Area (personal shape):

- Select by means of **AnyXmap Area (personal shape)** the to be measured surface. The + indicates where the probe is located at present time.
NB when one chooses AnyXmap Area, the *5:4 Aspect Ratio* option --> bottom right, should be ticked off



- Push *OK*
- Go to Stage – Table (-->top center) and adjust the amount of to be measured points in No-X en No-Y

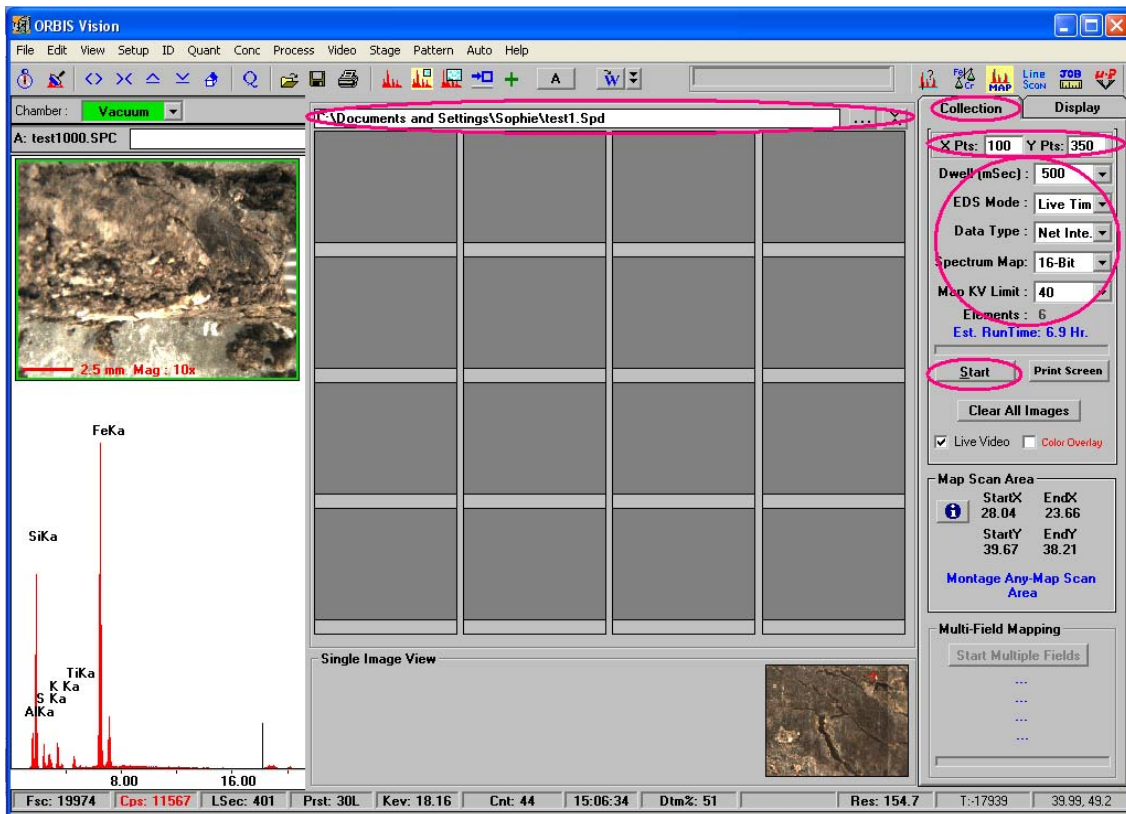
NB calculate the amount of points by taking into account the 30 µm probe, the length of the to be measured area (X of Y) and the amount of overlap that one desires for the measurements



no overlap – 25% overlap – 50% overlap

ORBIS Vision Stage Location Table															
Get Location From		Del Row		Delete All		Move		Show		Save		Deskew		UK	
<input checked="" type="radio"/> Stage <input type="radio"/> Video		<input type="radio"/> Point <input type="radio"/> Line <input checked="" type="radio"/> Matrix		Set Start Loca		Copy		Load		Print		Replace		1-Field Move	
No	Type	XStart	YStart	XEnd	YEnd	No-X	No-Y	ZStart	ZEnd	Rot-Ang	Pattern File	Label			
1	1	L	23.280	37.670	23.100	37.520	100	350	92.450	92.450		StgMap			
2															
3															
4															
5															
6															
7															

- Save the *Stage Location Table* so that one can retrieve the values in the future
NB this only applies when the sample has not been moved (manually) in the mean time in the µXRF
- Push *OK*
- Select in the *Collection* tab of the *Mapping*-mode ( icon top right) the Matrix size or resolution by inserting the same values as previously inserted in the *Stage Table* in the X Pts en Y Pts
NB First run a test map with a smaller resolution, matrix 32x25, to determine if high enough counts are recorded for each element, than run the actual test with a good resolution



C) Option Multi-Field Maps

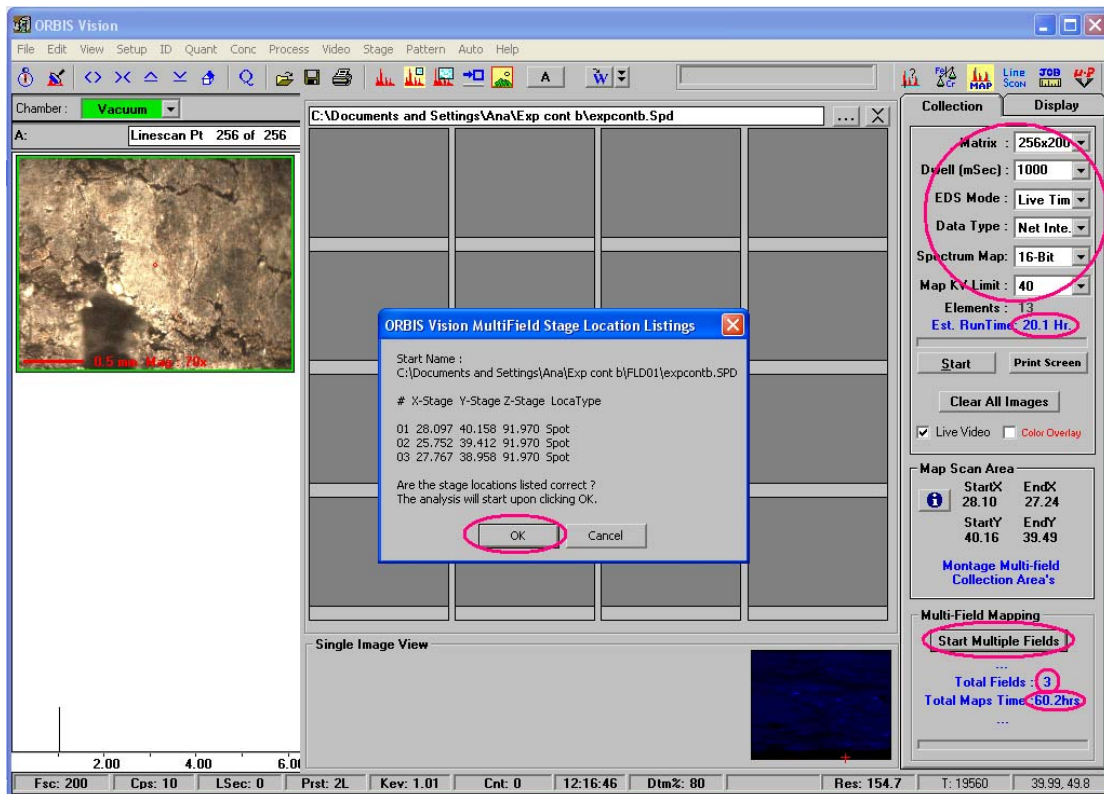
NB this is only possible with the preset 5:4 Xmap Area function

- Select **Set Xmap Area (5:4)**. The + where the probe is located at present time.



- Tick the *Multi-Field Maps* box
- Select the desired fields on the sample photo
- In the bottom left of the window, one can see the total amount of maps that were defined
- Save the photo
- Push *OK*
- Select in the *Collection* tab of the *Mapping-mode* ( icon top right) the Matrix or resolution

NB in the Mutli-Field Mapping option, one can choose only 1 resolution that will apply for all the defined maps. First run a test map with a smaller resolution, matrix 32x25, to determine if high enough counts are recorded for each element, than run the actual test with a good resolution



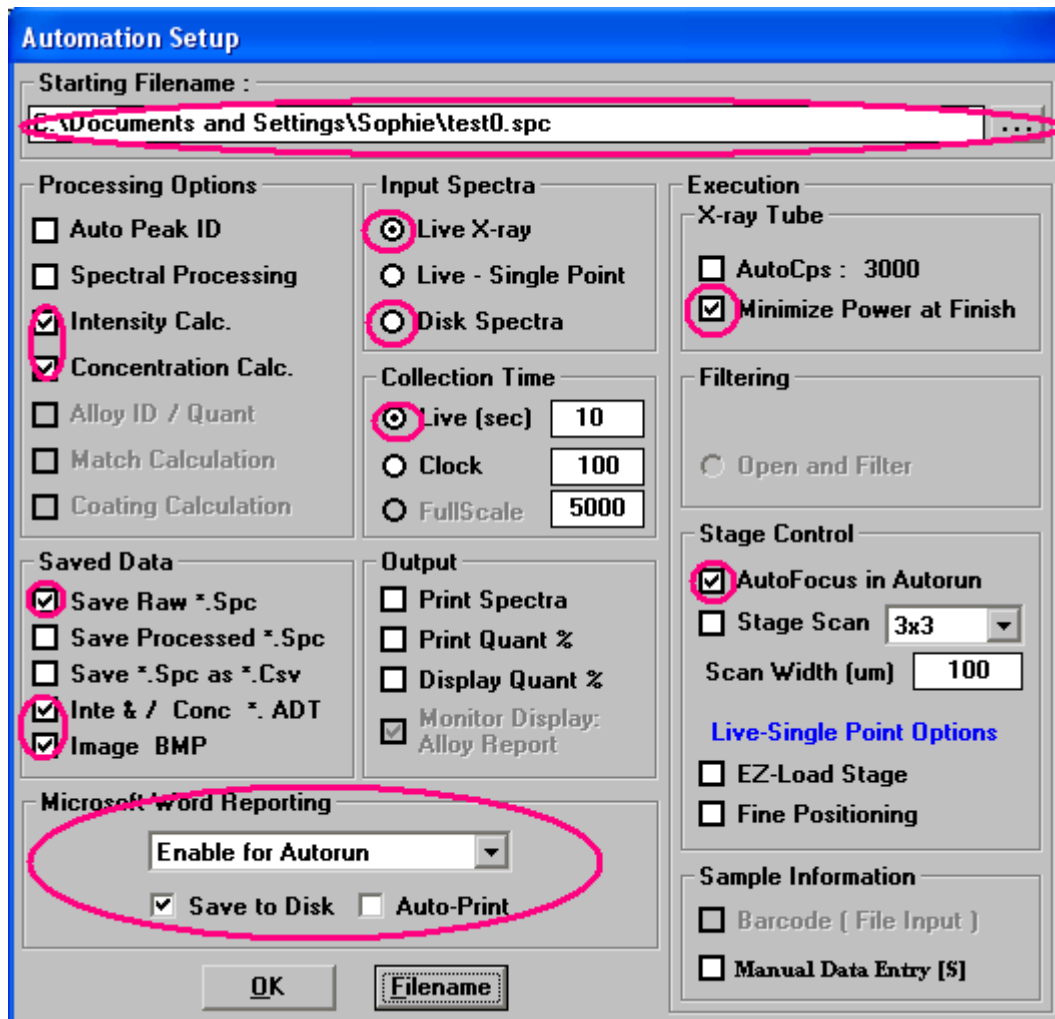
- Tick the *Color Overlay* box --> right center
- Choose *Dwell* time, for main elements <1000 msec, for minor and trace elements >10000 msec
- Set the EDS-mode to Live time
- Data type always on Net Integr. (otherwise the background will be measured as well)
- Spectrum map to 16-Bit so that the spectra are also being saved and can be reprocessed at a later point of time for elements that may have been missed or to generate point, line and matrix data within the map: see Orbis Vision User manual Ch. 8, Spectrum Map Data Output Functions, under *Help*
 - NB** not appropriate for quantitative processes
- Map kV Limit is standard on 40kV
- Check the (amount of) to be measured elements that were selected for mapping
 - Push **...** --> top right, to name the maps and to choose the proper folder where they are being saved
 - NB** the name cannot contain spaces and cannot be more than 6 characters
- Push *Start* for option A en B, push *Start Multiple Fields* for option C
 - NB** the Est. Run Time is usually longer than the program calculates, see '**Construction measuring-parameters**', and for Multi-Field Mapping the total (by the program estimated) running time is located in the bottom left
- For option C: push *OK*, the coordinates that appear are located in *Stage – Table*

Auto – Setup Output

Before one starts the Autorun, one has to choose the desired settings.

NB for further information about the Autorun settings see Orbis Vision User's manual, Chapter 5, p. 125-137

- Auto – Setup Output... --> top center



- Insert the desired *Starting Filename*, with a maximum of 32 characters
NB try to avoid numbers since the program will use the chosen number as its starting point, and will add up from it
- Tick the *Intensity Calc.* or *Concentration Calc.* box under Processing Options
NB when using the Concentration Calculations on creates a .CSV file that can be read with Excel. With this program one can make one's own linescan with a graph and then use appropriate programs, for example Paint and Word, to make or take the image of the linescan location and to overlay it

with the created graph. This is sometimes necessary because the software occasionally shows overlays that are not overlain on the exact location that was measured.

- Tick the *Save Raw *.Spc, Inte & / Conc *.ADT* and *Image BMP* box (creates a folder with all the images) under *Saved Data*
- Choose *Live X-ray* if one want to run a new scan, if one wants to re-process the result files, *.CSV or *.SMY, choose *Disk Spectra*

NB if one is going to re-process Disk Spectra, the program will ask for to enter a SPC-Reprocess waiting Time. This can be useful if one want to see the re-processing of each spectrum or if one want to print the spectra

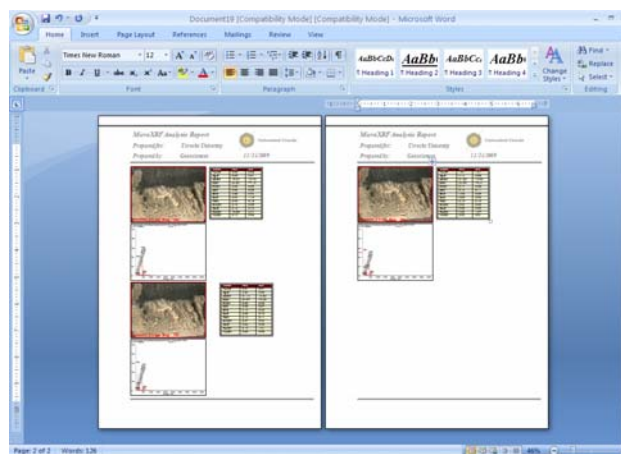
- Choose under *Collection Time* the desired *Live (sec)* time, this is the measuring time per point
- Under *Execution* one can choose for *Minimize Power at Finish* if one is running a scan over the weekend or vacation
- If one has a (very) irregular sample it is recommended to choose under *Stage Control* de *AutoFocus in Autorun*. This feature will focus each point.

NB this will cost a lot of extra time, as does the following option

- The *Enable for Autorun* under *Microsoft Word Reporting* will send **every** made spectrum to a word template. Make sure that the proper template is chosen via  before the measuring is started. If one also chooses *Save to Disk*, the document will be automatically saved when the scanning is finished.

- ❖ For spectra choose *UU Template-Spec.dot* (6 spectra per page)
- ❖ For sample images choose *UU Template Img.dot* (12 images per page)
- ❖ For images, spectra and quantitative data choose *UU Template-Cust.dot* (2 measurements per page, see image below)

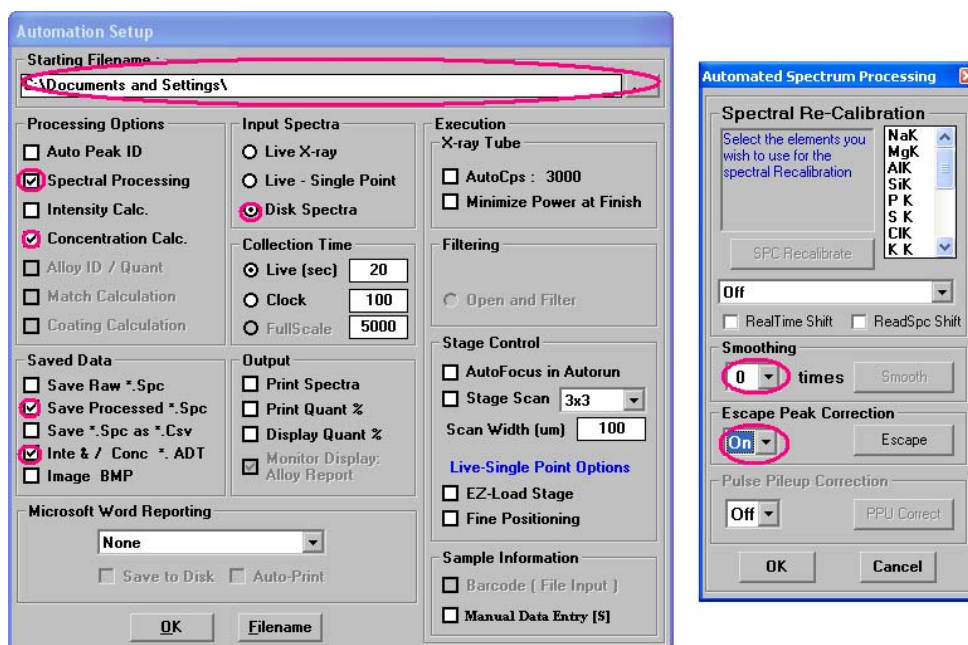
NB if one wants to change the amounts of spectra/images per page, one has to create a new Template via the Wizard under 



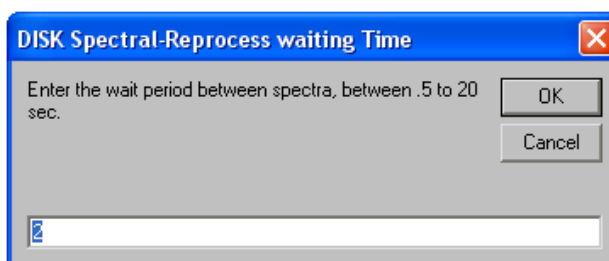
- Push *OK*

Re-processing of data

Whith spectral re-processing one can remove escape peaks and one can smooth the data (removal of statistical noise).



- *Auto – Setup output...*
- For *Starting Filename* choose the first spectrum of the to be re-processed sequence
- Tick the *Concentration Calc.* box and the *Spectral Processing* box
 - ❖ Choose *Smoothing* x-times, if desired
 - ❖ Choose *Escape Peak Correction – On*, if desired
 - ❖ Push *OK*
- Tick the *Save Processed *.Spc* box and the *Inte & / Conc *ADT* box
- Choose Input Spectra: *Disk Spectra*
- Push *OK*
- Choose under *Peak-ID* mode the desired elements
- *Auto – Start Autorun*



- Choose the wait time between spectra (in seconds), for example 1 or 2 seconds
- The spectra will now be re-processed and a .CSV file will be created with the starting time in its name

Executing a quantitative analysis

- Choose in μ Probe mode ( icon top right) the voltage and current (Dead time <40%) and focus the image
- Create a spectrum to determine the elements that will be measured
- Choose in *Peak ID*-mode ( icon top right) the elements that will be mapped by means of the created spectrum
- Quant – Options --> center top
- Define conditions:
 - Oxide or not
 - Intensity mode normal or cps/ μ A (makes no difference for quant)
 - KENO (Known Elements Not Observed): The adding of known amounts of not measured elements
 - For example 44% CO₂ in limestones of calcite
 - The totals that one want to measure in the sample
 - Analyze methods
 - ❖ Fundamental Parameters no Standards
 - ❖ With standards is not yet available
- For quantifying there are various options:
 - Quantifying a set of spectra:
 - First define the to be analyzed points, lines, or matrices in the stage table when at the 70x magnification (for accurate locations), see **'Analysis of a point, line or matrix, and multiples via Stage Table'**
 - Then adjust the Auto – Setup Output... settings to one's own desire, see **'Auto – Setup Output'**
 - Auto – Start Auto Run
 - After the analysis is finished, all the results are saved as *.CSV and *.SMY files, the last can be made visible via Auto summary
 - Or quantifying individual spectra:
 - Click on the point to be analyzed in the image window --> left top
 - Go to the Quantification window ()
 - Press *Concentrations*